UNIVERSITY OF CALIFORNIA, SAN DIEGO

Engineering of anisotropic metallic nanomaterials

A dissertation submitted in partial satisfaction of the
requirements for the degree of Doctor of Philosophy

in

Nanoengineering

by

Sohini Manna

Committee in charge:

Professor Eric E. Fullerton, Chair
Professor Oleg Shpyrko, Co-Chair
Professor Michael J. Heller
Professor Vitaliy Lomakin
Professor Shirley Meng

2016

The Dissertation of Sohini Manna is approved and is acceptable in quality and form for publication on microfilm and electronically:

Co-Chair

Chair

University of California, San Diego

2016

DEDICATION

I dedicate my dissertation to my parents, Atanu K Manna and Krishnakoli Manna, who have encouraged and supported me throughout my life and gave me the freedom to pursue all my dreams including this one.

EPIGRAPH

Do! Don't Try!

Eric Fullerton

TABLE OF CONTENTS

LIST OF FIGURES

ACKNOWLEDGEMENTS

This dissertation represents an incredible journey from both an academic and a personal perspective. It has changed my world view and made me a wiser, stronger and more perseverant person. I could not have asked for a better educational institution than University of California, San Diego not only because it provided me with very intelligent peers and mentors but also the weather and the beach next to it made every bad research day into a good reason to be here. So many emotions and thoughts are racing through my brain while writing this section as it is the most crucial part of my dissertation. I hope I do justice.

First and formost I would like to thank, from the bottom of my heart, my PhD adviser, Prof. Eric Fullerton, who took a chance on me, many times, and taught me that success comes only after a series of failures. I truly learnt to be an independant scholar under his guidance. I now finally have the courage to take the lead in any sphere of life. I would also like to thank my other mentors especially Dafine Ravelosona who gave me a chance to work on a very interesting project in Paris. Not only was that an opportunity of a lifetime (which girl does not dream of living in Paris), I learnt a lot of new techniques in a completely different enviroment. I even learnt french. I would also like to thank Prof. Henrik Ronnow, Prof. Samarendra Kumar Ray, Goran Nilsen, Liza Herrera Diez and Edwin Fohtung for all the encouragement and opportunities without which I would not have even be able to go to graduate school. I would like to thank my collegues, Jimmy, Erik Shipton, Raj, Charles and especially Nasim who had my back throught this journey.

The first part of this chapter has material verbatim from journal article [2] authored by me . The second part of this chapter is based on reference [3] which is work done in collaboration with J.W. Kim, S. H. Dietze, A. Ulvestad, R. Harder, E. Fohtung and O. G. Shpyrko. The main result of this disseration was work done in collaboration with H. Ren who helped me further my project as my mentee. Also would like to thank my other

co-authors; Y. Takahashi , M. Lubarda, J. Wingert, F. Spada, V. Lomakin.

This journey would have been a lot more difficult without my group of friends. I am not sure what I would have done without my support system, Augusta Modestino, who no matter what, always provided me with good cooked food with good wine and honesty; Valentin Robert who always lent me a listening ear; Niki Vazou, Margherita, and Elaine who not only gave me company for whining but are incredible sources of inspiration; Marcela and Dimo for being the best roomates I could hope for. Anukool, Vivek, Max and Srdjan, thank you for being there and always making me laugh; Sania for always being the person I can discuss science and PhD life with since the very beginning. I would also like to acknowledge my high school friends (Jasleen, Harleen and Vivna) for always keeping me grounded and for a lasting friendship. And friends who are not near but still dear, Gaelle and Lavinia, who always skype with me whenever I am feeling low, no matter which part of the world they are in. And last but not the least, Tom, who has made the hardest time " the writing time" fun, who brought a lot of happiness, warm hugs and smiles, who kept a check on my progress, who encouraged me throughout the time that we spent together.

I would like to specially thank my family which includes my aunt and uncle, Sumitra and Shantanu Manna and my parents Krishnakoli and Atanu K Manna, for their continuous support and words of encouragement which kept me going. This thesis and PhD is for them.

VITA

2005-2009	Bachelor of Engineering (Hons.), Birla Institute of Technology and Science (BITS), India
2010–2012	Master of Science, University of California San Diego, USA
2015–2016	Exchange PhD student, Université Paris-Sud, France
2012-2016	Doctor of Philosophy, University of California San Diego, USA

PUBLICATIONS

"Characterization of strain and its effects in ferromagnetic nickel nanocubes" S. Manna, J.W. Kim, M.V. Lubarda, J. Wingert, R. Harder, F. Spada, V. Lomakin, O.G. Shpyrko, E.E. Fullerton (in prep.)

"Magnetoresistive response of singlecrystalline Ni nanowires with superconducting contacts " S. Manna, H. Ren, E.E. Fullerton (in prep.)

"Synthesis of single-crystalline anisotropic Au nano-crystals via chemical vapor deposition" S. Manna, J.W. Kim, Y. Takahashi, O.G. Shpyrko, E.E. Fullerton *Journal of Applied Physics*, 119 (2016)

"Observation of x-ray radiation pressure effects on nanocrystals" J.W. Kim, A. Ulvestad, S. Manna, R. Harder, E. Fohtung, A. Singer, L. Boucheron, E.E. Fullerton & O. G. Shpyrko *Journal of Applied Physics*, 120 (2016)

"Curvature-induced and thermal strain in polyhedral gold nanocrystals" J.W. Kim, S. Manna, S. H. Dietze, A. Ulvestad, R. Harder, E. Fohtung, E.E. Fullerton & O. G. Shpyrko *Applied Physics Letters*, 105 (2014)

CONFERENCES

S. Manna, H. Ren, E.E. Fullerton "Magnetoresistive response of singlecrystalline Ni nanowires with superconducting contacts " *Magnetism and Magnetic Materials Conference*, New Orleans, USA (November 2016)

S. Manna, L.H Diez, E.E. Fullerton, D. Ravelosona "Light Ion Irradiation of CoFeB-MgO ultra thin films with perpendicular anisotropy" *Domain Walls and Spintronics*, Spetses, Greece (September 2016)

S. Manna, J.W. Kim, O. G. Shpyrko E.E. Fullerton Anisotropic gold nanocrystals via chemical vapor deposition Poster presented *Materials Research Society (MRS) Spring Meeting*, San Francisco, USA (April 2015)

ABSTRACT OF THE DISSERTATION

Engineering of anisotropic metallic nanomaterials

by

Sohini Manna

Doctor of Philosophy in Nanoengineering

University of California, San Diego, 2016

Professor Eric E. Fullerton, Chair
Professor Oleg Shpyrko, Co-Chair

This dissertation explores the nanofabrication and characterization of anisotropic metallic nanomaterials. Employing both bottom-up and top-down fabrication techniques, the chemistry and crystal structure of metals were exploited to create an assortment of anisotropic nanomaterials ranging from gold nanocrystals to nickel nanowires to CoFeB/MgO thin films. We investigate the role of anisotropy on the physical properties in these nanomaterials. The anisotropy arises from the combined effects of the shape, crystal structure and symmetry breaking at interfaces. The effect of anisotropy on properties such as strain, magnetic anisotropy and micromagnetic configuration were investigated.

A variety of characterization techniques ranging from imaging, simulations and magneto-transport measurements were employed. We first study the strain distribution within anisotropic nanocrystals associated with its shape. We further study the interplay between the nanocrystals and the substrate on the strain distribution. We then study the relation between the strain, magneto-crystalline anisotropy and shape on the magnetic response of Ni nanostructures, including magnetic vortex configurations in Ni nano-cube and nano-wires. This interplay leads to complex domain patterns and could enable novel bio-magnetic applications and magnetic-superconducting devices. Lastly we explore ion-irradiation as a tool to modify the interfaces of ultra thin films with which we can tailor the magnetic anisotropy.

Introduction

The term ”anisotropy” has greek origins, ”anisos” meaning unequal and ”tropia” meaning turn or change. The etymology of this word reflects its definition especially in the scientific context where anisotropy refers to direction dependence of properties. Wood is an excellent example of how human civilization have used anisotropic properties to their advantage from the very beginning. One of the hallmarks of wood's success is its anisotropy of strength and hardness in different orientations[1]. Anisotropy is present in most materials and its effects are more pronounced at nanoscale. Hence, the study of anisotropic nanomaterials becomes more essential.

Scientists are exploring and understanding the nanoscale anisotropic building blocks, mostly semiconducting materials. The bulk of this dissertation is focussed more on transition metal anisotropic nanomaterials. The work on micron sized whiskers of Iron(Fe), Cobalt (Co) and Nickel (Ni) dates back to 1950-60s but there was not much progress on their controlled growth. Especially because the tools to characterize them effectively had not yet been developed. Nanofabrication and characterization tools are more easily available in every university which gives us the edge to explore and exploit the anisotropic properties of transition metals.

There has been tremendous development involving isotropic nanoparticles; however, anisotropic nanoparticles made of metals and metal oxides, etc., are emerging because of their superior mechanical, electrical, magnetic, optical and chemical properties. Their applications have been demonstrated in electronics, photonics, biological and

chemical sensing, imaging and drug delivery, etc. Owing to their preferred orientation and ordering, anisotropic nanoparticles can be organized into a multitude of well-defined higher-order assembled structures.

> ”Nature has a great simplicity and therefore a great beauty”-Richard Feynman

The overall theme of this dissertation is simplicity. How can we synthesize single crystals of metals in its natural crystalline form in a simple way ? How can we exploit its natural anisotropy to our advantage?

The first chapter details the bottom up fabrication approach of creating anisotropic metallic nanomaterials using chemical vapor deposition and dc magnetron sputtering and the second chapter expounds on the characterization techniques employed to investigate the properties of these materials.

The third chapter presents an in-depth analysis of zero dimentional anisotropic gold and nickel nanomaterials. The first part of this chapter has material verbatim from journal article [2] authored by me. The second part of this chapter is based on reference [3] which is work done in collaboration with with J.W. Kim, S. H. Dietze, A. Ulvestad, R. Harder, E. Fohtung and O. G. Shpyrko. This chapter has material which is work done by me along with my other co-authors; Y. Takahashi , M. Lubarda, J. Wingert, F. Spada, V. Lomakin.

The fourth chapter investigates the effect of passing current through superconducting electrodes in one-dimentional single crystal magnetic nickel nanowire. The main result of this disseration is presented in this chapter which was work done in collaboration with H. Ren who helped me further my project as my mentee.

The fifth chapter discusses the role of light-ion irradiation in tailoring the magnetic anisotropy of CoFeB/Mgo ultra thin films.

Overall we notice anisotropy manifests in a variety of ways and impacts the properties of nanomaterials.

Chapter 1

Fabrication and synthesis techniques

Most of the anisotropic nanomaterials ranging from nanocrystals to nanowires described in this dissertation were synthesized employing Chemical vapor deposition (CVD). Since, it was the primary technique used, various aspects of CVD will be detailed. The thin films and the electrodes for nanowires (for electric characterization purposes) were deposited using magnetron sputtering system. Other fabrication techniques such as lithography will be briefly discussed.

1.1 Chemical Vapor Deposition (CVD)

The traces of chemical vapor deposition (CVD) can be traced back to pre-historic times when cavemen lit a lamp, and the soot was deposited on walls of a cave. CVD, nowadays, is fundamental tool for manufacturing just about anything from advanced electronics to potato chip bags. Probably the earliest patent describing a CVD process was by John Howarth for the production of carbon black, which due to lax safety standards led to the burning down of a wooden plant. The earliest patent describing CVD process for deposition of metals was reported around 1855 where Wohler used WCl_6 with hydrogen carrier gas to deposit Tungsten metal. The major impetus to the technology has been provided by the rapid development of Silicon Valley since the mid-1970s. The microelectronics revolution called for very thin high purity films with precise control of

uniformity, composition and doping.

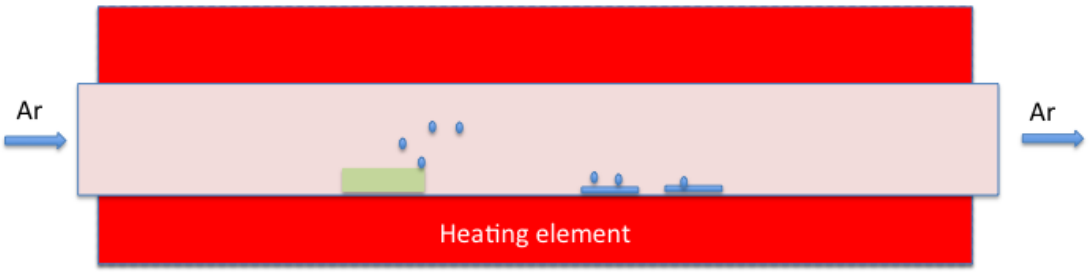

Figure 1.1. Schematic of chemical vapor deposition (CVD)

A typical CVD process involves aspects of thermodynamics, fluid dynamics, chemistry and kinetics. It involves a series of gas-phase and surface reactions. Hence, it is diverse in both the parameters that affect growth and the products that can be achieved. The key steps in most CVD process involve the following

- Evaporation and transport of precursors in the gas fow region into the reactor
- Gas phase reactions of precursors in the reaction zone to produce reactive intermediates and gaseous by-products
- Mass transport of reactants to the substrate surface
- Adsorption of the reactants on the substrate surface
- Surface difusion to growth sites, nucleation and surface chemical reactions leading to product formation
- Desorption and mass transport of remaining fragments of the decomposition away from the reaction zone

1.1.1 Thermodynamics

The basis for the of occurrence any chemical reaction, even the ones in a CVD process, depends on if the energy involved is minimized or not. The second law of thermodynamics states that the entropy of any isolated system always increases. What it entails is that, for starting reactants with free energy of formation $\triangle G_{reactant}$ and resulting products with free energy of formation $\triangle G_{product}$, the net change in energy for the reaction ($\triangle\ G_{reaction}$) needs to be negative.

$$\triangle G_{reaction} = \sum \triangle G_{product} - \sum \triangle G_{reactant} < 0 \tag{1.1}$$

The free energy of formation is dependent on particular atoms/molecules involved and the bonds formed and broken as well as the temperature and pressure of the reaction enviroment.

1.1.2 Mass Transport

An important step in CVD is the transportation of the precursor from the source to the reaction chamber. In most cases, the precursor is volatile and hence is easily converted to its gaseous form, which then is transported either by a carrier gas, such as argon or hydrogen, or diffuses due to the gradient in pressure. As the gaseous mixture flows across a surface there is a boundary layer directly over the surface through which the reactants diffuses. Following diffusion through the boundary layer, adsorption onto the surface takes place and reactions occur on this surface. Next, any reaction by-products and other escaping atoms/molecules will desorb from the surface and diffuse back through the boundary layer where it will then be carried off with the main stream of flow outside the boundary layer. The surface mentioned here can be any surface over which the reactants flow, including the reaction chamber walls and intentionally positioned growth substrates.

The type of deposition in CVD can be classified into two main categories

- Mass transport limited : The influx of ractants in the reactor is limited and sets the rate of growth.
- Surface reaction limited : Enough reactants are available but the reaction on the surface is limited by the temperature or the available catalytic particles.

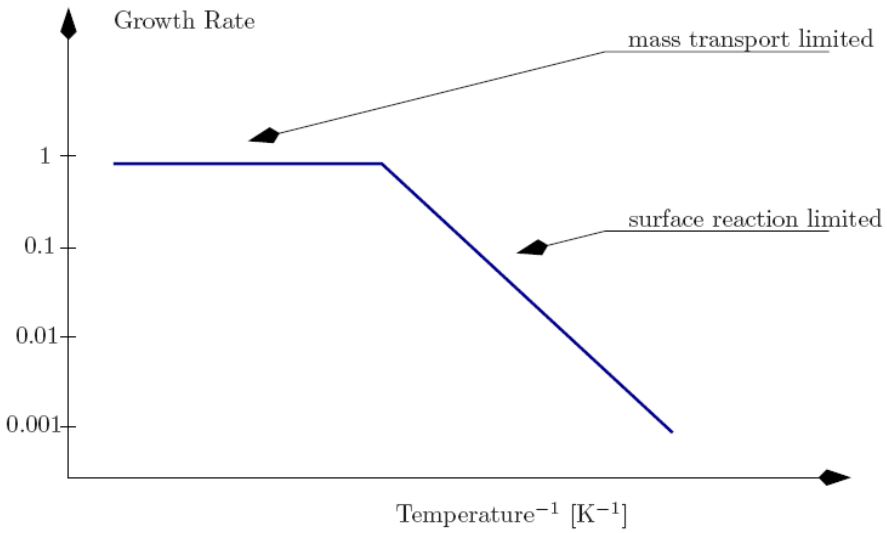

Figure 1.2. Deposition rate as a function of temperature

1.1.3 Chemistry

The end-products of a CVD process is highly dependant on the starting reactants, also known as precursors. Whichever form of CVD process is employed, the precursor requirements are similar. The characteristics of an ideal precursor are

- Adequate volatility to transform in a gaseous form
- Stability so that decomposition does not occur during evaporation

- Sufficient temperature window between evaporation and decomposition for deposition
- High chemical purity
- Non-hazardous
- Long shelf life and readily manufactured

Thermal decomposition reactions are among the most fundamental process in the CVD of materials and involve the splitting of molecules into their constituent atoms or more elementary molecules by supplying an adequate amount of heat to overcome bonding. A second route to breaking down a starting molecule is through reduction, the gain of electrons leading to a lower oxidation state.

In traditional thermal CVD, which is the method that was employed in the synthesis of nanomaterials presented in this dissertation, the growth is determined by several parameters, the primary ones being the temperature of the substrate, the operating pressure of the reactor and the composition and chemistry of the gas-phase.

1.2 Sputtering

Sputtering is a physical vapor deposition (PVD) technique carried out in vacuum for depositing very thing films onto substrates. Sputtering occurs when an ionized gas molecule is used to displace atoms of a specific target material. These atoms then bond at the atomic level to a substrate and create a thin film. Several types of sputtering processes exist, including: ion beam, diode, and magnetron sputtering.

The history of PVD is closely associated with the development of vacumm technology. In 1852, W.R Grove was the first to study the effect of sputtering when he deposited highly polished silver surface which was the anode with tip of a wire as

coating source which was the cathode at a pressure of about 0.5 Torr. However, Thomas Edison holds patent for commercial use of sputtering. In the mid-1930s Berkhardt and Reineke patented a means of increasing the ionization of atoms thermally evaporated into a plasma at low pressure. They used a magnetic field parallel to the electric field between the source (anode or ground) and the substrate (cathode).

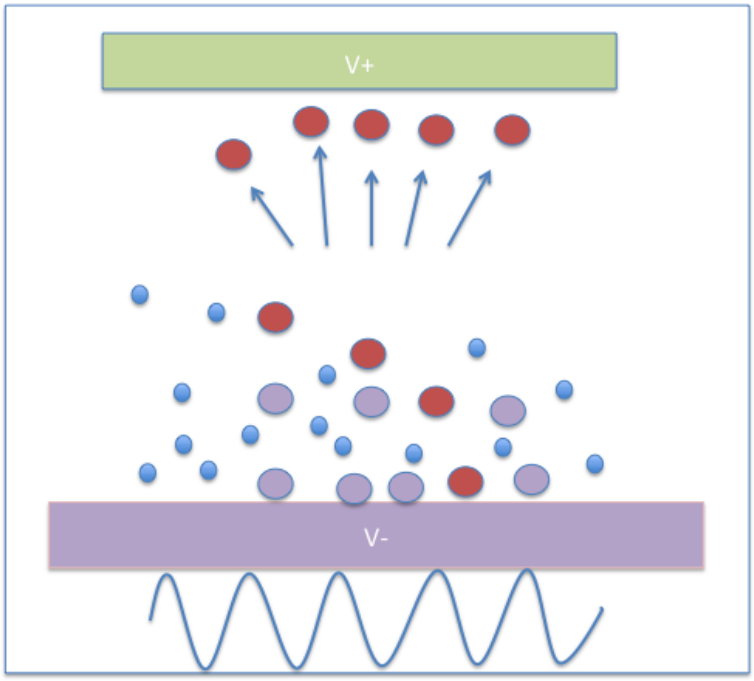

Figure 1.3. Schematic of magnetron sputtering

In this dissertation, most of the thin films and the electrical contacts were deposited using magnetron sputtering system. GE coined the term ”magnetron” in 1920s for devices that used magnetic fields to control the motion of electrons and ions. In a magnetron sputtering system, a magnet is placed behind the cathode which traps free electrons and make their paths more circuitous which leads to an increased probability of electrons ionizing neutral gas molecules by several orders of magnitude. This increase

in available ions significantly increases the rate at which target material is eroded and subsequently deposited onto the substrate.

1.3 Photolithography

The word lithography which is derived from greek words ”lithos” meaning stone and ”graphein ” meaning to write refers to the process invented by Aloys Senefelder in 1796. He used a bavarian limestone which he inked and then treated with chemicals and could tranfer a carved image onto paper. Following the chemical treatment of the stone, image and non-image area became oil receptive and oil repellent, respectively, attracting ink onto the image area and attracting water on non-image areas. Using photons to treat the chemicals in this process is what is known as photolithography which is used widely in fabricating integrated circuits.

Performance of a photolithographic process is determined by its resolution i.e the minimum feature size that can be transferred. The basic photolithography and pattern transfer steps involve resist coating, exposure, development, etching and resist stripping.

Chapter 2

Characterization techniques

Considerable progress in the field of nanotechnology has been possible due to a myriad of sophisticated characterization techniques available to study various properties of nanomaterials. Characterization of nanomaterials includes the determination not only of size and shape but also the chemical structure and other important properties. The techniques include various electron microscopy in addition to standard techniques such as X-rays and advanced techniques such as coherent X-ray diffraction imaging.

Characterization of nanomaterials is performed at different levels. Some of the methods are used to study the structural aspects such as size, shape and morphology, whereas other methods are used to study the internal crystal structure, magnetic and optical properties. The characterization techniques used to study the various aniostropic nanomaterials presented in this dissertation are described briefly as follows.

2.1 Scanning electron microscope (SEM)

Scanning electron microscope uses a probe made up of electrons with energies typically upto 40 keV which scans the surface of the sample in raster pattern to generate an image. The electrons interact with the sample surface and generate various signals which are collected and analysed to give us information about the sample. The signals are mainly comprised of secondary electrons, with energies of a few tens of eV, high-energy

electrons backscattered from the primary beam and characteristic X-rays.

The development of electron miscroscopy began with the realization that electron wavelengths calculated by de Broglie around 1925 were almost five orders of magnitude smaller than the wavelength of light used in optical microscopy. Knoll built a first scanning microscope in 1935, however, the resolution limit was around 100 mm because of the diameter of the focused beam on the specimen. The first true SEM was described and developed in 1942 by Zworykin, who showed that secondary electrons provided topographic contrast. The first commercial SEM, the Cambridge Scientific Instruments Mark I Stereoscan was developed in 1965. The SEM we are using today are not very different from this first instrument.

The major components which make up a SEM

- Electron source
- Column with electromagnetic lenses which guide the electrons
- Electron detector
- Sample chamber
- Computer and display to view images

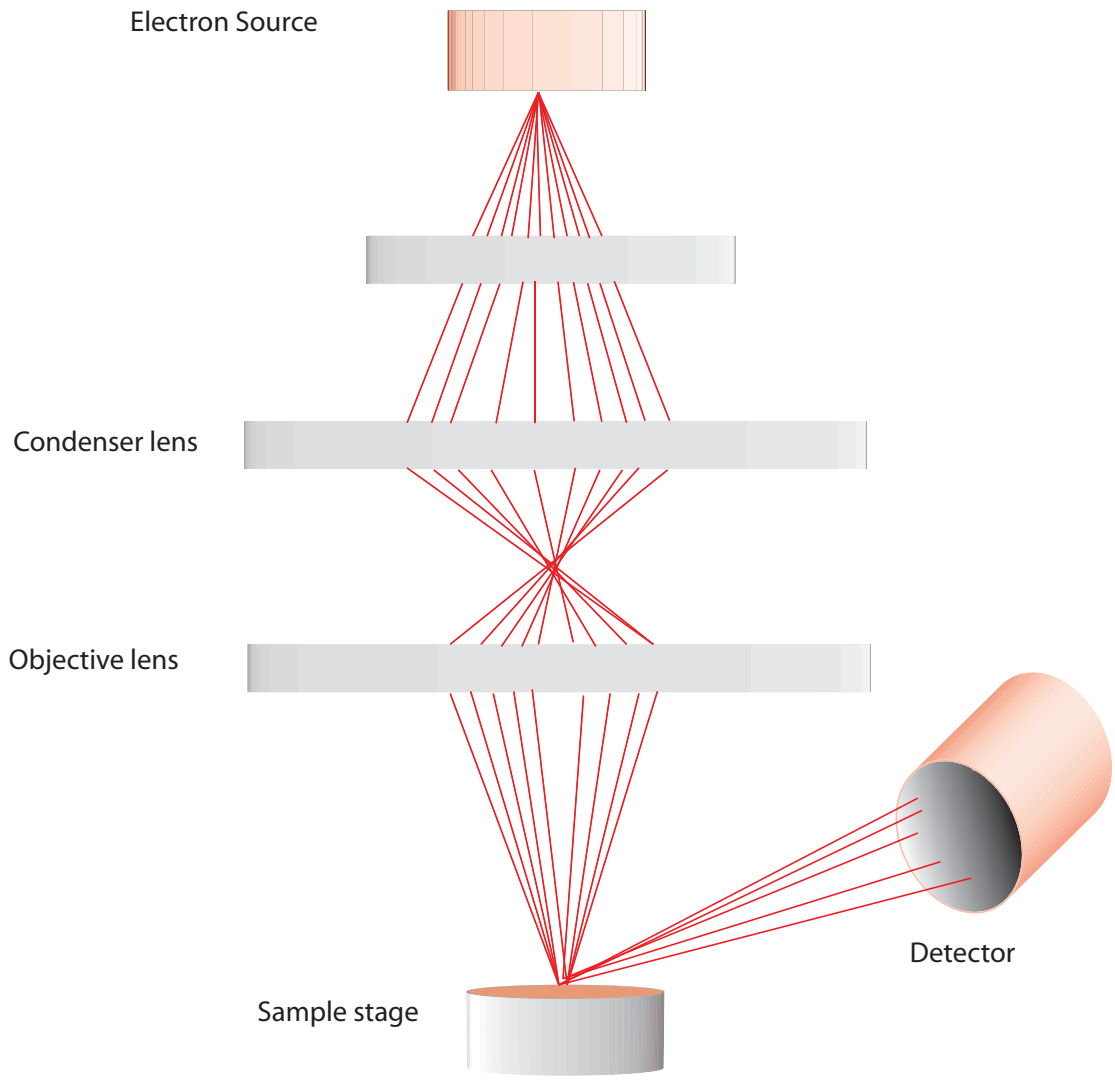

Figure 2.1. Schematic of Scanning electron micoscope (SEM)

Electrons are produced at the top of the column, accelerated down and passed through a combination of electromagnetic lenses and apertures to produce a focussed beam of electrons which hits and interact with the surface of the sample. The electron beam moves in a raster pattern, collecting information generated at each point due to the electron-sample interaction. The signals generated are then collected by the detector.

The FEI XL30 SEM in the nano3 cleanroom was used for most of the characetriza-

tion of both magnetic and non magnetic nanomaterials presented in this thesis. FEI XL30 SFEG features the FEI Sirion column which enables high resolution secondary electron imaging at low KV. Using UHR (Ultra High Resolution) mode and the through Lens Detector, resolution of 1nm is possible at 10KV or higher and 1.7nm at 1KV.

2.2 Atomic force microscopy (AFM)

The atomic force microscope (AFM) is a high resolution scanning probe microscope (SPM) with very high resolution and provides three dimentional information. AFM measures local properties, such as height, force or magnetic field with a probe [4]. The probe scans in a raster pattern measuring the local properties simultaneously generating a 3-D image. Not only direct contact forces under the tip-sample affect the catilever but also far-ranging forces such as Van der Waals and magnetic forces. Magnetic samples can be imaged for domains structure by using magnetic tips. This is also known as Magnetic force microscopy (MFM)[5].

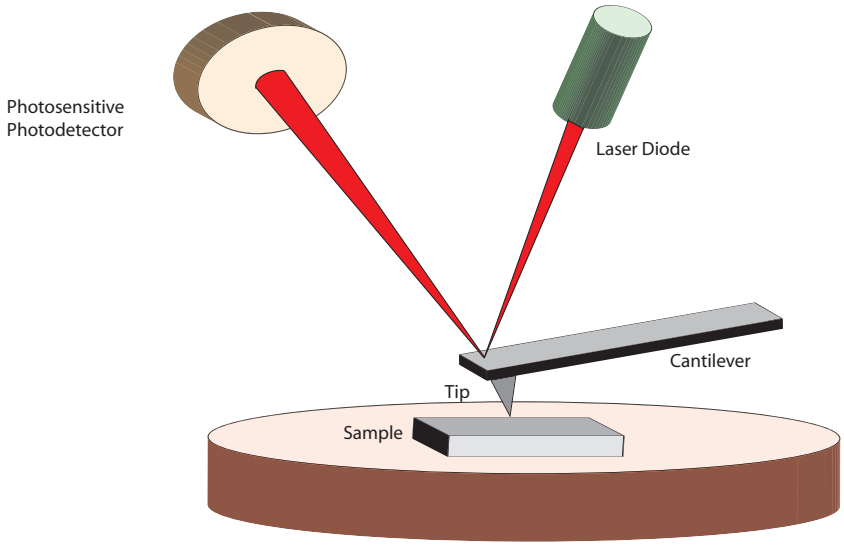

Figure 2.2. Schematic of Atomic force micoscope (AFM)

The AFM came into being after Binnig realized the shortcoming of scanning

tunnelling microscope (STM) with which one could only study conductive samples. Binnig along with Quate and Gerber later proposed to combine principles of STM and stylus profilometer and innovated the current AFM. The principle behind AFM is the interaction of a sharp tip with sample generates sufficient force which can be measured.

An atomic force microscope includes a tip mounted on a micromachined cantilever. As the tip scans a surface to be investigated, interatomic forces between the tip and the sample surface induce displacement of the tip and corresponding bending of the cantilever. A laser beam is transmitted to and reflected from the cantilever for measuring the cantilever orientation.

2.3 Coherent X-ray diffractive imaging (CXDI)

X-ray diffraction methods lie at the base of material science and crystallography. X-rays, traditionally, have been used to finger-print elements, probe the chemical structure, grain size and size of nanomaterials. Coherent diffractive imaging (CDI) is a lensless method for 3D reconstruction of nanoscale structures such as gold nanocrystals and nickel nanocubes as presented in this dissertation. Typically, a highly coherent beam of x-rays or electrons is diffracted off of the nanostructure to be imaged. In this dissertation, most nanostructures were imaged by employing x-rays at Sector 34-ID-C of the Advanced Photon Source (APS) synchrotron facility.

The underlying principle of CXDI is collection of several diffraction patterns of nanocrystals by hitting them with coherent beam of x-rays. The samples can be rotated about an axis perpendicular to the beam to extract 3D information. A simple fourier transform of the diffracted pattern only retrieves the intensity information. The phase information, which is also vital for complete reconstruction, is lost, and can be obtained by employing a Hybrid input output (HIO) algorithm for phase retrieval using adequately sampled intensity data with feedback[6].

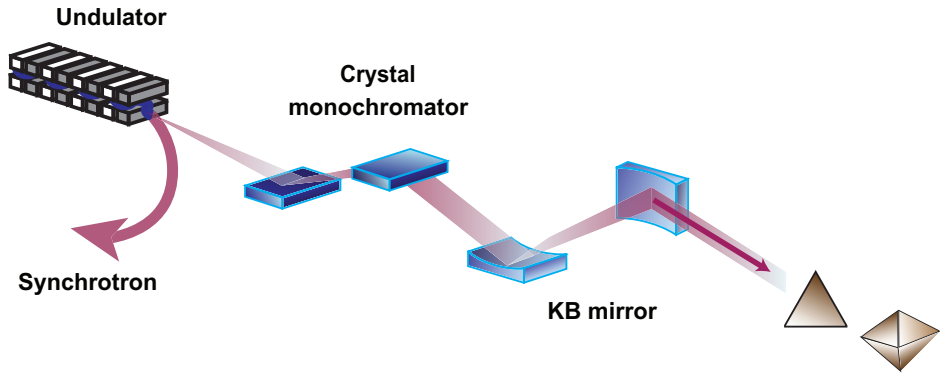

Figure 2.3. Schematic of Coherent X-ray diffractive imaging (CXDI

The CXDI is not only applied to create 3D images but is also used to map internal strain at nanoscale[7]. This technique not only probes the overall shape of crystal but also the displacement of individual atoms from an ideal periodic lattice. We employed CXDI to map the internal strain of individual gold nanocrystal and nickel nanocubes.

2.4 Micromagnetics Simulations

Micromagnetics is a method which deals with predicting the behaviour of ferromagnetic materials at sub-micrometer length scales. Ferromagnetism is a very quantum mechanical effect, however, in this theory, a ferromagnet is considered a n-body problem. These length scales are considered large enough for the materials to be considered with the continuum approximation and not as discrete atomic structures, yet small enough to resolve magnetic structures like domain walls and vortices. Micromagnetics can be used to describe the equilibrium state of magnetic system by minimizing the energies which comprise the total magnetic energy of the system. It can also predict dynamics in

magnetic system by solving time dependent Landau-Lifshitz-Gilbert equation.

Micromagnetics simulations provide us with a way to characterize and understand properties of individual ferromagnetic particles or a sub part of a larger magnetic system, which sometimes is not possible by other means of characterization techniques.

2.4.1 Energetics of a Ferromagnet

The total energy of a ferromagnet with respect to magnetization depends on a variety of effects, some of which are classical in nature and others are more quantum mechanical effects. Stable magnetization configurations are obtained by finding the local minima of the magnetic energy function. The total energy plays a role in the dynamics of the system.

The magnetic energy comprises of the following energy terms

- Exchange Energy : The characterstic feature of ferromagnetism is the existence of spontaneous magnetization. It is due to the exhange energy between the neighbouring spins of ferromagnetic atoms which causes them to align parallelly which leads to macroscopic uniform magnetization configurations.

- Demagnetization Energy : Also known as the stray-field energy, it is the energy of the magnetization in the magnetic field created by itself. What it entails is that this energy contribution accounts for the dipole-dipole interaction of the elementary magnetic atoms.

- Anisotropy Energy : This energy term accounts for the various anistropy energies such as magnetocrystalline or magnetoelastic. Magnetocrystalline anisotropy is dependent on the crystal structure of the ferromagnetic material. Magnetization is energetically favoured in certain axes also known as the easy axes. Depending on the lattice structure, some materials may have more than one easy axes. The

simplest case is that the material has a single easy axis, in such cases it is known as uniaxial anisotropy and occurs in materials with a hexagonal or tetragonal crystal structure for e.g. in cobalt. Cubic anisotropy occurs in materials such as iron which has a body-centered cubic structure or nickel which has a face-centered cubic structure. Magnetoelastic anisotropy is the energy due to elastic lattice distortions. Magnetization can be induced in preferred directions due to local distortion of the crystalline solid. Most of the time, this effect is ignored.

- Zeeman Energy : The Zeeman energy of a ferromagnetic body is the energy of the magnetization in an external field.

2.4.2 Magnetization Dynamics

The Landau-Lifshitz-Gilbert equation describes the motion of the magnetization in an effective field.

$$\frac{d\mathbf{M}}{dt} = -\frac{\gamma}{1+\alpha^2}[\mathbf{M}\times\mathbf{H}_{eff} + \alpha\frac{\mathbf{M}}{\mathbf{M_s}}\times(\mathbf{M}\times\mathbf{H_{eff}})] \tag{2.1}$$

This motion can be described as the sum of a precessional term and a damping term. The Landau-Lifshitz-Gilbert equation with effective field contributions as introduced in the preceding sections is a non-linear partial differential equation in space and time which cannot be solved analytically.

FastMag[8], developed by Prof. Lomakin's group, is a finite element method computational solver for simulating magnetization/spin dynamics in ultra-complex magnetic systems. FastMag can handle large complex structures meshed over tetrahedral elements. It allows modelling of a variety of magnetic systems, such as magnetic recording heads, media, and of magnetic nanoparticles.

2.5 Physical Property Measurement System (PPMS)

The Physical Property Measurement System (PPMS) by Quantum Design is an unique instrument which can perform a variety of automated measurements. It consists of a variable temperature - field system and can be connected to SQUID magnetometer to perform magnetic as well as electrical characterizations. The sample environment ranges from 1.9K - 400K and applied field ranges upto 9T. The majority of magnetoresistance measurements presented in this dissertation were obtained using PPMS.

Chapter 3

Zero Dimension:Anisotropic Nanocrystals

3.1 The ecstacy of gold

Au nanostructures have been a subject of intensive research due to their fascinating properties which give rise to a myriad of applications such as catalysis [9–12] , biosensing [13–17], plasmonics [18–20] and nanoelectronics [21] to name a few. The physical properties of such nanostructures are not only just size dependent but also influenced by the specific shape of the nanocrystal, their surface facets as well as the internal crystalline structure and strain. Hence much effort has been made to synthesize a variety of different shapes and sizes of Au nanostructures such as prisms[22, 23], decahedra [24, 25], nanorods [26–28], octahedral [29, 30], and icosahedra [31–33]. Many of these methods employ the use of surfactants [34–36] or polymers [37–39] that are attached to the final product and require filtration. As a result, in most cases, the surfactants or the capping layer used are still adhered on the Au nanocrystals after filtration processes, which are then difficult to remove. The biggest disadvantage of colloidal and the wet synthesis methods is aggregation of Au nanoparticles. In most of the wet-synthesis methods indicated in literature, CTAB (hexadecylcetyltrimethylammonium bromide) is used to stabilize the nanostructures by selectively forming a tight packed bilayer, which

reduces aggregation. The CTAB covered Au nanostructures are highly toxic[40–43] rendering them useless for applications such as drug delivery and bio sensors. While Au nanostructures are inherently not toxic, toxicity arising due to CTAB and other cationic ligands[44, 45]. Furthermore, many of these methods require the use of Au seeds [35, 46, 47], which adds an extra step in the synthesis process. The advantages of the methodology we present is the formation of high quality crystals without the need of external surfactant, capping layer or stabilizer. Au nanostructures on supported substrates[48] are used as catalysts for selective hydrogenation of acetylene[49] or hydrogenation of aromatic nitro compounds[50] and on certain metal oxides supports, Au nanostructures act as catalyst for low temperature CO oxidation[51–53]. For effective catalytic activity of Au nanostructures, their surface needs to be free from capping ligands and encapsulation, which is extremely difficult with the current wet-synthesis process. Our methodology prevents that and proves to be an efficient way to prepare supported Au nano-catalysts.

We investigate the growth of single-crystal anisotropic Au nanocrystals on Si substrates using a single-step catalyst-free chemical vapor deposition (CVD) method [54, 55]. This approach yields a range of nanostructures as highlighted in figure below.

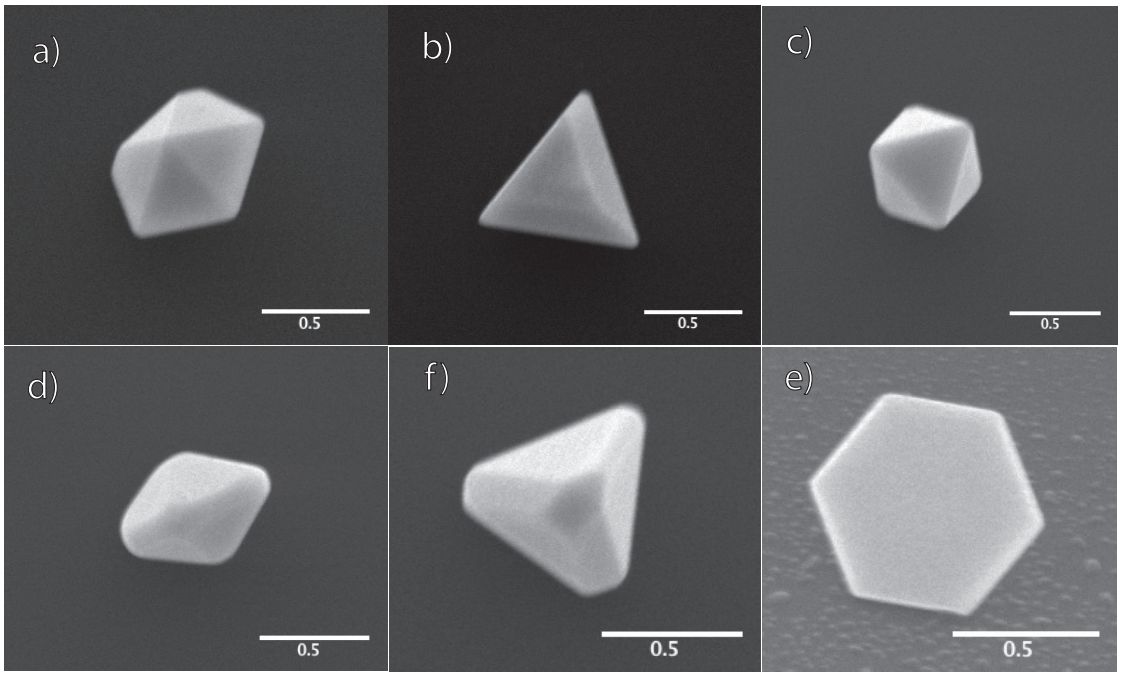

Figure 3.1. SEM images of different morphological Au nanocrystals that are formed in the CVD process including (a) decahedron, (b) triangular plate, (c) icosahedron, (d) bipyramid, (e) triangular prism and (f) hexagonal plate. The scale bar is given in microns.

3.1.1 Synthesis of gold nanocrystals

The Au nanostructures are made via one-step catalyst-free thermal CVD method (shown schematically in Fig. 3.2(a)) using gold halide as the precursor. The approach is similar to approaches recently used to synthesize Ni nanowires and nanocrystals on SiOx substrates [54, 55]. Roughly 1g of powdered $AuCl_3$ is loaded in a boat and is placed upstream of five Si (100) substrates placed in-line at distances of 3 - 15 cm in a quartz tube. The quartz tube is then introduced into a Blue Lindberg furnace at 475°C. An Ar carrier gas is flowed through the quartz tubing using a mass flow controller (the Ar gas flow is set at 10 sccm) while the downstream end of the CVD set up is separated from the outside atmosphere using a water bubbler. The system is maintained at 475°C for about an hour after which it is cooled down to room temperature while still maintaining Ar flow. Gold halide is hygroscopic and decomposes above 160°C. Above 420°C, it is

further reduced to pure Au. Powdered gold halide at high temperatures vaporizes and the argon gas flow carries the vapors over the Si(100) substrates and is deposited on the substrate and forms into crystals.

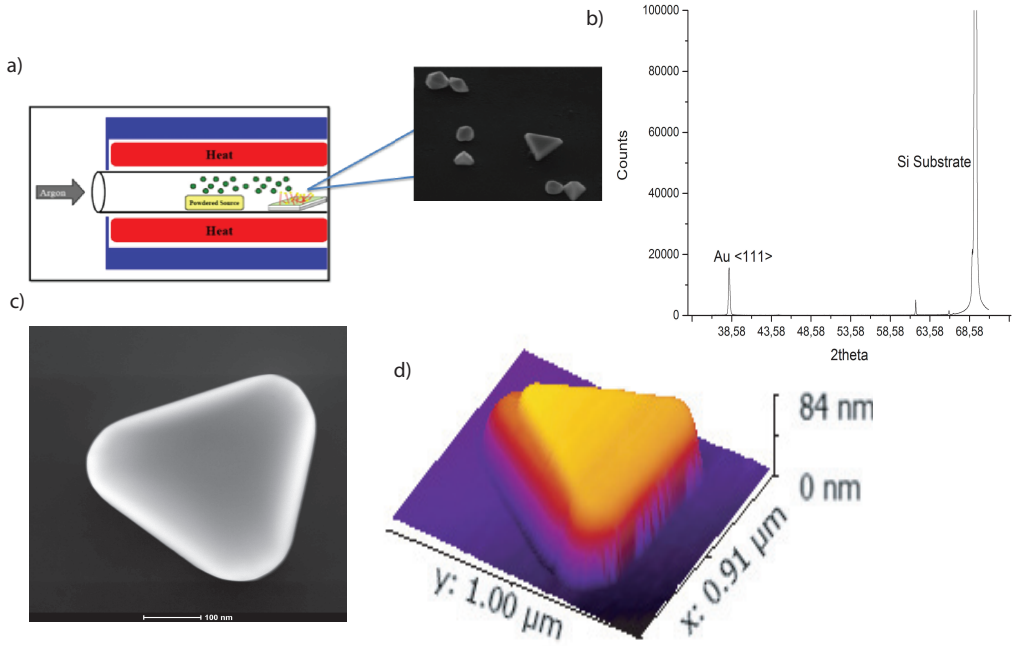

Figure 3.2. Characterization of Au nanocrystals (a) Schematic of CVD setup (b) X-ray diffraction patter of as-grown Au Nanocrystals on Si(100) substrate (c) HAADF image of a triagular plate (d) AFM image of a triagular plate.

3.1.2 Growth mechanism of gold nanocrystals

The CVD growth procedure described above produces many Au nanocrystals deposited on the substrate. We observe a bimodal growth of crystals where the initial stage is formation of various twinned Au nuclei and the second stage involves the merging of smaller crystals into larger mostly untwinned Au nanocrystals. The nanocyrstals thus formed are distinct 3-dimentional structures as opposed to 2-dimentional island clusters. This indicate a Vollmer-Weber fashion growth mode [56] instead of a van der Merwe

mode. Fig 3.1 (a)-(f) shows SEM images of Au nanocrystals of different morphologies including pyramids, bipyramids, decahedron, icosahedron, triangular and hexagonal plates.

To characterize the average structure and chemical composition of the nanocrystals, we performed XRD, AFM and EDX on selected samples. Fig 3.2(b) shows the XRD scan performed on as-grown Au nanocrystals on a Si(100) substrate. The XRD pattern shows only Bragg diffraction peaks from the Si substrate and those expected from randomly oriented fcc Au with the lattice spacing is 0.408 nm. There are no diffraction peaks due to any impurities or additional phases. AFM performed on a triangular plate shows crystalline structure with sharp edges.

To further probe the internal structure of individual nanostructure we employed coherence x-ray diffraction (CXDI). These spectra were obtained at beamline Sector 34-ID-C of the Advanced Photon Source (APS) synchrotron facility. These coherent diffraction patterns from individual crystals were recorded for the rocking curves of the (111) Bragg reflections by rotating the sample through the Bragg peak in increments of 0.005°. 121 frames were collected in this manner for each nanocrystal, covering a total angular range of 0.6°. Shown in Figs. 3.3(a) and (b) are example scans from the (111) Bragg peak from two distinct individual nanostructures. The observed fringes result from a finite crystal size and confirm that the Au nanostructures are single crystals with well-defined, sharply terminated facets [3]. The fringes are due to interference of x-rays scattered from flat facets of the nanocrystals. Using a phase retrieval algorithm as described in Ref [3] both the shape crystal and the internal strain profile in the nanocrystal can be determined. Shown in Figs. 3.3(c) and (d) are the retrieved shapes of the crystal, which are similar to SEM images of Au nanostructures formed in this process. These results confirm these particulars are single-crystal. If there were multiple grains or twins in the crystal then only part of particle would appear in the reconstruction(i.e. the part that met the Bragg

condition).

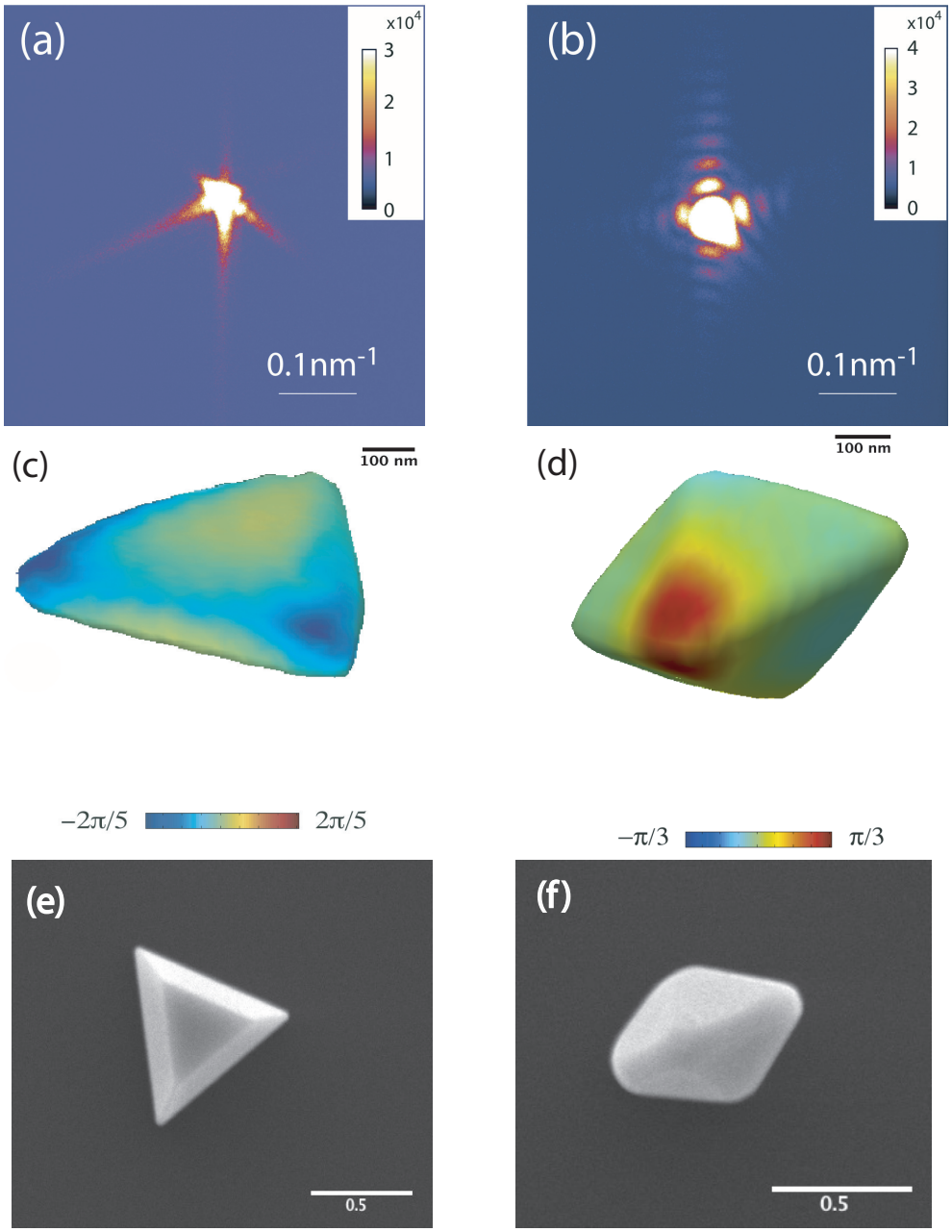

Figure 3.3. 3D images reconstructed using CXDI (a) Coherent X-ray diffraction pattern of Au triangular plate (b) Coherent X- ray diffraction pattern on Au octahedral crystal (c) Phase reconstruction of triangular plate (d) octahedral plate (e) SEM image of Au triangular plate (f) SEM image of Au octahedral crystal.

In the previous study of CVD Ni nanowire growth on SiOx substrates, Si was

observed to mediate the growth [54, 55]. Elemental EDX was performed on the nanocrystals to check for the presence of Si in the nanocrystals. Au nanocrystals were grown directly on Silicon Dioxide support TEM films as shown in Fig. 3.4(a). EDX images (shown in Fig. 3.4 (c) & (d)) shows only presence of Au on SiOx membranes. Within the resolution of the experiment no Si signal was observed. Both XRD and EDX are consistent with the formation of pure fcc Au nanocrystals. Since the growth of the crystals is initiated at the temperature above Au-Si eutectic temperature (363°C), it is likely that growth is not mediated by the formation of silicides. To further affirm that, we grew Au nanocrystals in other substrates like Quartz, Ni metal and SiN substrates where we observed similar growth of Au crystals which confirms that the crystal growth is not likely due to the formation of silicides. Furthermore we grew anisotropic Ag crystals on Si at 475°C which is much lower than the Ag-Si eutectic temperature (835°C). Also the ease with which we can transfer the Au nanostructures onto other substrates using contact transfer process further supports that these structures sit on the substrate and are not bonded onto it.

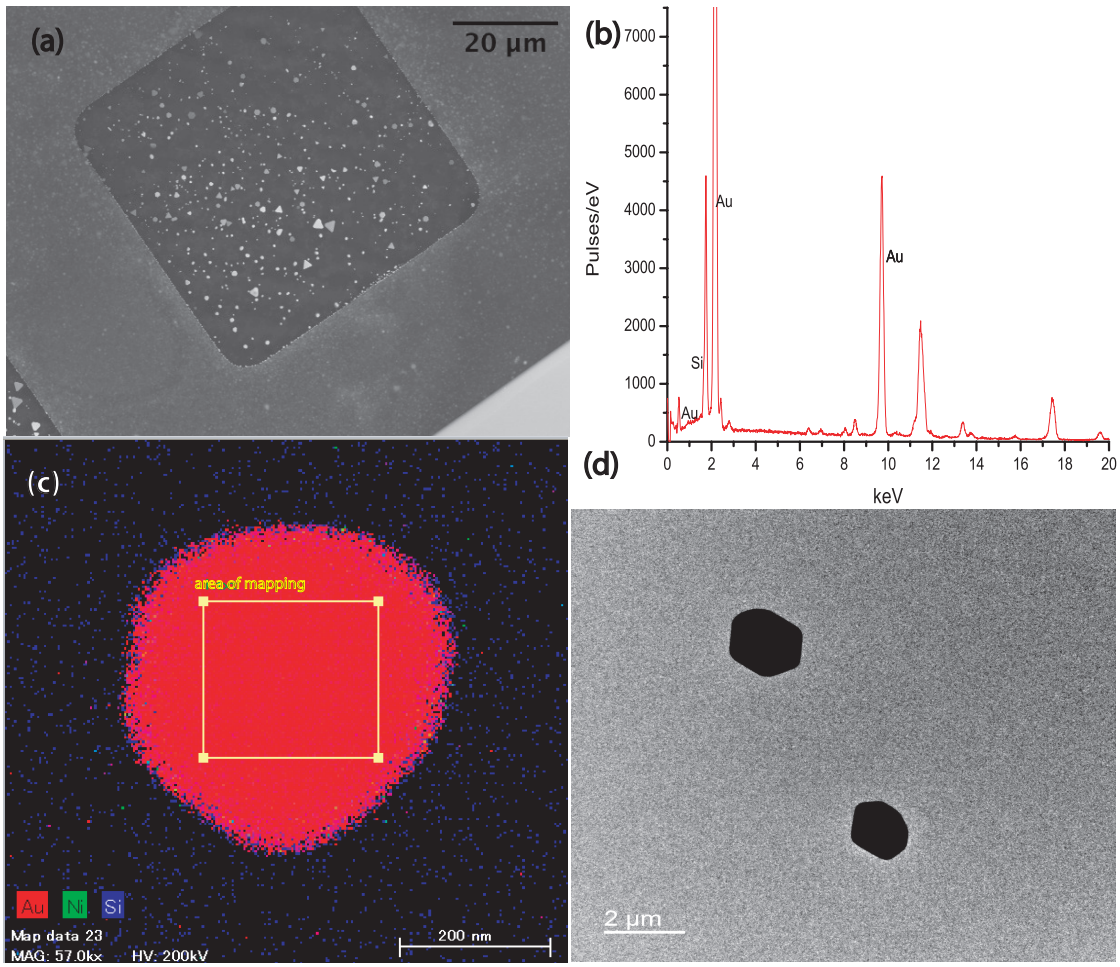

Figure 3.4. TEM of Au nanocrystals (a) As grown Au nanocrystals on SiO2 support film TEM grids (b) TEM image of Au nanocrystals (c)& (d) Elemental mapping (EDX) of Au nanocrystals indicating that there are no impurities in Au nanocrystals

To explore the formation mechanism for Au nanocrystals we performed ex-situ SEM measurements of nanocrystal size distribution by terminating the crystal growth at different times well below the final growth time of one hour described above. The typical results of SEM images and the histograms of the resulting nanocrysal size distributions are shown in Fig. 3.5. We observe a bimodal growth of Au nanocrystals i.e. (i) formation of nuclei and (ii) further growth of nuclei into 3-dimentional crystals. SEM performed after a short initial growth time (5 minutes) show the formation of a large number of nuclei, with a significant number whose shape are consistent with multiple-twinned

structures like icosahedrons and decahedrons. At longer growth time (10 minutes) the density of particles decrease, while the size of the particles increase. This indicates the coalescence of smaller nuclei into bigger particles indicating Oswald ripening effect [57](growth of larger clusters at the expense of smaller clusters). This coalescence stage results in primarily non-twinned, single crystalline structures like prisms and bi-pyramids.

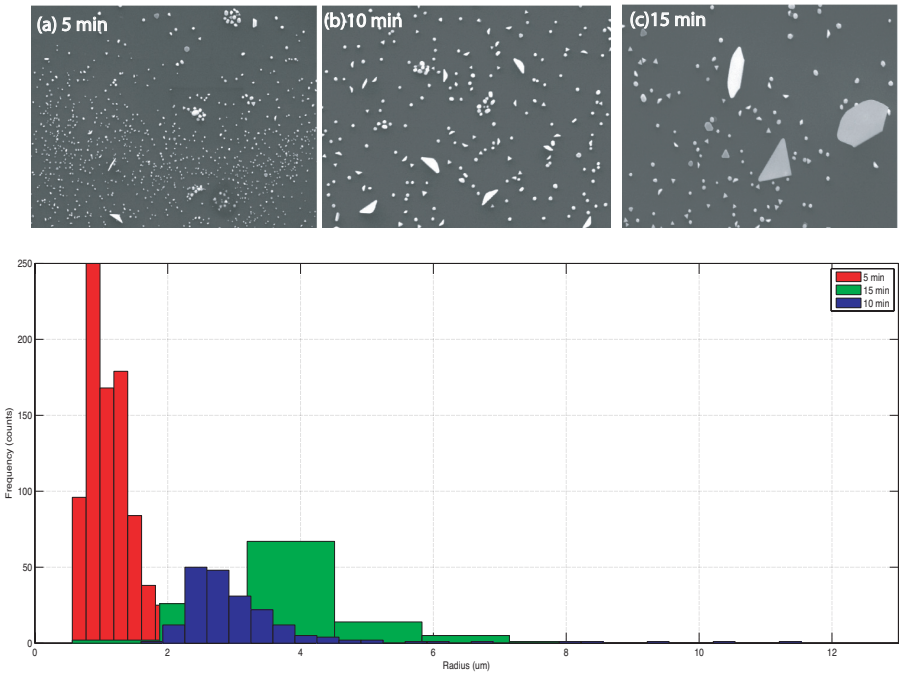

Figure 3.5. Evolution of Au nanocrystals over time, (a) At t=5 mins, the number of Au nuclei are much larger most of which are twinned (icosahedrons or decahedrons). With t=10mins (b), some of the nuclei have grown into larger non-twinned prisms. At t=15 mins (c), the average particle size has increased indicating Oswald ripening effect.

Simple and multiple twinning are prevalent among f.c.c metals. In most cases, the larger particles have simple twinning or no twinning and the multi faceted twinning is present in the smaller nanostructures. It appears therefore that the twins forms in the nuclei during early stages and the larger particles are formed from the coalescing of these smaller twinned structures, but interdiffusion leads to the formation of non-twinned particles [58]. At temperatures above 420°C, the halide reduces to pure Au, which is

deposited onto the Si substrates with the native oxide layer. The oxide layer provides a source of line defects, which provides kinks for Au nucleation [59]. These acts as nucleation points that attracts more Au atoms that are formed from thermal reduction. The Au nanocrystals are thus formed via Vollmer-Weber growth [60] since no external catalyst was used, nor any impurities were detected [61]. The initial formation of twinned nanocrystal is driven by reduction of free surface energy,which is favored by extensive faceting, and small twin boundary energies. Icosahedral particles are most stable for very small particles and decahedral particles are stable in a very narrow size range [62]. For a twinned nanocrystal to transform into a single crystal extensive atomic rearrangements are required which is kinetically difficult. Once a twinned nanocrystal is formed, it can grow to large sizes (micrometer range). The presence of impurities and defects also plays a critical role in the growth of twinned structures [62]. Many theories have tried to explain the formation of thermodynamically unfavorable structures such as the triangular prisms or the decahedrons over just isotropic spheres [58, 62, 63]. Most common methods to form Au nanocrystals is via solution based routes that involve the reduction of Au salt using organic molecules or surfactants. Therefore the proposed mechanisms use the presence of organic molecules to curb or accelerate the addition of ad atoms on certain crystalline planes, or the presence of external surfactants which behave as templates for crystal growth that lead to the shape confined growth. Since we have prepared Au nanocrystals via CVD without using organic molecules or surfactants or shape defining templates, our results are not consistent with the above-proposed mechanisms. Strictly thermodynamic explanations are not sufficient and we have to also include kinetics of the nuclei growth, size and structure. The presence of diverse shapes and sizes of nanostructures in each batch with uniform external conditions imply that the kinetics of individual nuclei play a very important part in the growth of these structures. Since the conditions under which the growth takes place are far from equilibrium, kinetics rather

than thermodynamics determine the final morphology[64].

Au nanocrystals have been formed by dewetting monolayer of adsorbed Au atoms on oxide surfaces like TiO_2 [65] and $SrTiO_3$[66] in ultra high vacuum conditions. In those cases, the substrate surface energy is greater than the interface energy plus surface energy of Au so that the substrate wets easily. We observe in Fig. 3.6(a) a similar layer plus island growth (StranskiKrastanov growth) on Ni substrates where the surface energy of substrate $\sim 1977 mJ/m^2$ which is greater than the surface energy of Au

$$\gamma_{substrate} > \gamma_{Au} + \gamma_{interface}$$

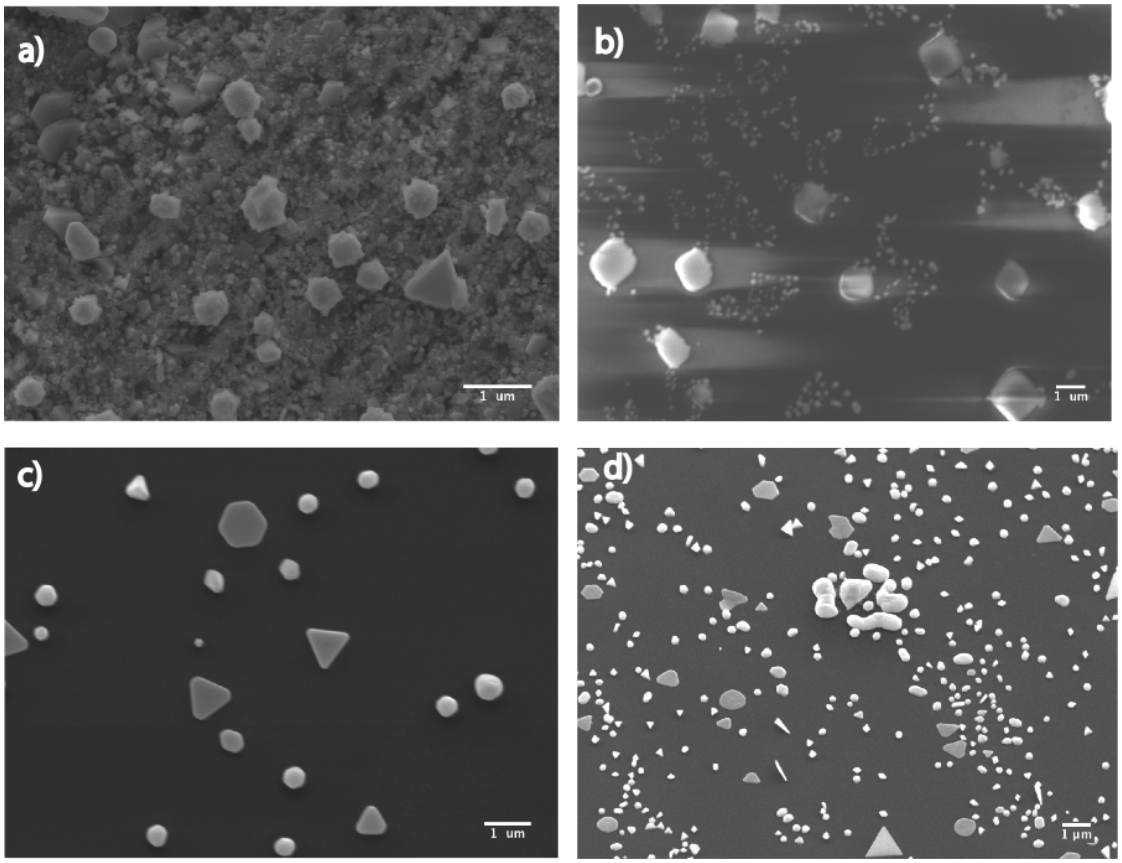

Figure 3.6. Au nanocrystals on different substrates. SEM images of CVD of Au on (a) Ni substrate, (b) SiO_2 on Si, (c) SiN, and (d) Si (100) with native oxide. The scale bar is given in microns.

But in our system, the surface energy of the Si wafer substrate (native oxide) is $\sim$ 53 $mJ/m^2 \ll$ surface energy of Au which 1500 mJ/m^2. Au is known not to have a good adhesion on Silicon substrate, the native oxide layer further reducing adhesion by acting as a diffusion layer. Hence, wetting of Si substrate by Au is not possible. Furthermore, atoms tend to like having as many nearest neighbors as possible promoting growth of three dimensional nanoclusters rather than a thin film. Also the reduction of total surface energy as the number of low energy $<111>$ facets increase in number [62, 67].

3.1.3 Strain mapping of gold nanocrystals

We use CXDI to map the local distribution of strain in individual gold nanocrystals. These measurements were performed at Sector 34-ID-C of the Advanced Photon Source (APS) synchrotron facility at Argonne National lab with our collaborators at Oleg Shyprko's lab at UCSD Physics department.

The concept of strain is used to describe the structural shift of the crystal from ideal configuration state. The origin of strain can be attributed to various forces such as chemical, electrical or magnetic in nature which can cause internal stress. Due to the enhanced role of surfaces and interfaces, stress and in turn strain plays a more important role in nano-crystals as compares to their bulk counterparts. Mathematically, strain is expressed as the spatial derivative of the displacement of atoms from an ideal lattice which is tensorial in nature.

$$\varepsilon_{xx} = \frac{\partial u_z(r)}{\partial x} \tag{3.1}$$

where ε_{xx} is the normal strain along x direction.

Coherent beam of x-rays with E = 9.0 keV obtained by using a monochromator were focused onto individual gold nanocrystals using Kirkpatrick-Baez mirrors that restricted the beam size to a 2μm $\times$ 2μm region. The resulting diffraction patterns were measured using a charge-coupled device (CCD) with 22.5 μm pixels located along the

detector arm at a distance of 0.9m beyond the sample.

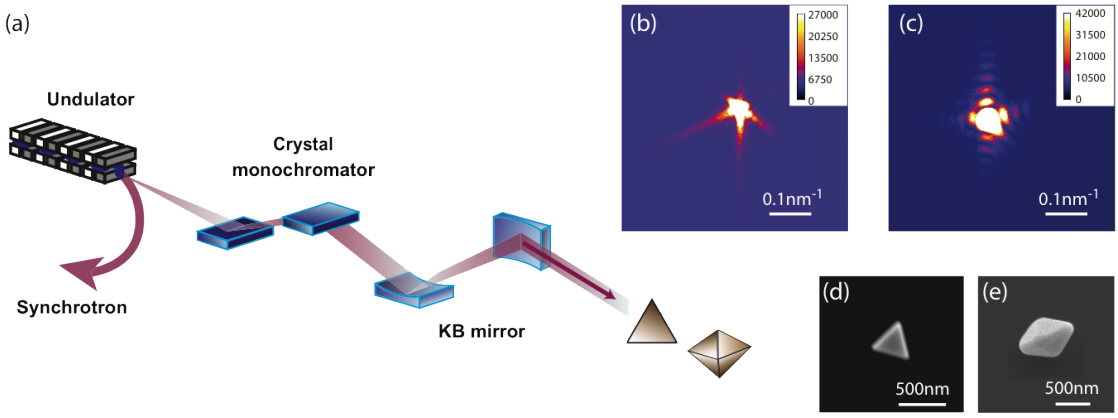

Figure 3.7. Set up for CXDI of gold nanocrystals (a) A monochromatic x-ray beam focused with Kirkpatrick-Baez mirrors illuminates a sample. The diffraction pattern is captured in the far field on a CCD area detector, (b) and (c) scanning-electron microscopy (SEM) images, (d) and (e) measured 2D coherent x-ray diffraction patterns from (111) Bragg reflections for a triangular nanoplate and an octahedral gold nanoparticle, respectively, (f) and (g) 3D diffraction patterns for each particle obtained by rocking scans with a total 121 frames.

The 2D diffracted patterns of a triangular nanoplate and an octahedral nanocrystal were recorded for the rocking curves of the (111) bragg reflections by rotating the sample in increments of 0.005°, covering a total angle of 0.6°. 121 frames were collected for each nanocrystal and by stacking them, 3D isosurfaces were obtained. The fringes, seen as spatial modulations in the signal, originate from the interference between waves diffracted from pairs of sharply terminated crystalline facets. Accordingly, the four pairs of fringe modulations in the diffraction pattern imply the presence of eight facets (i.e., an octahedron). The lack of symmetry in the diffraction pattern reflects strained nanocrystal[68]. The displacement field projected along the 111 Bragg plane direction was plotted to quantify the internal nanoscale strain field within the nanocrystals.

Figure 3.8 (a) show the geometry of gold nanocrystals on a silicon substrate with momentum transfer wave vector $\vec{Q}$ of (111) Bragg reflection, which is normal to the substrate for both crystals. Figure 3.8 (b) and (c) represent the reconstructed crystals, the

octahedron nanocrystal with an edge length of 220nm and the triangular nanoplate 60 nm thick and 600 nm as its edge length. The phase (shown on the color scale) in Figure 3.8 (d) and (e) indicate the projection of the deformation onto the reciprocal lattice vector $\vec{Q}$.

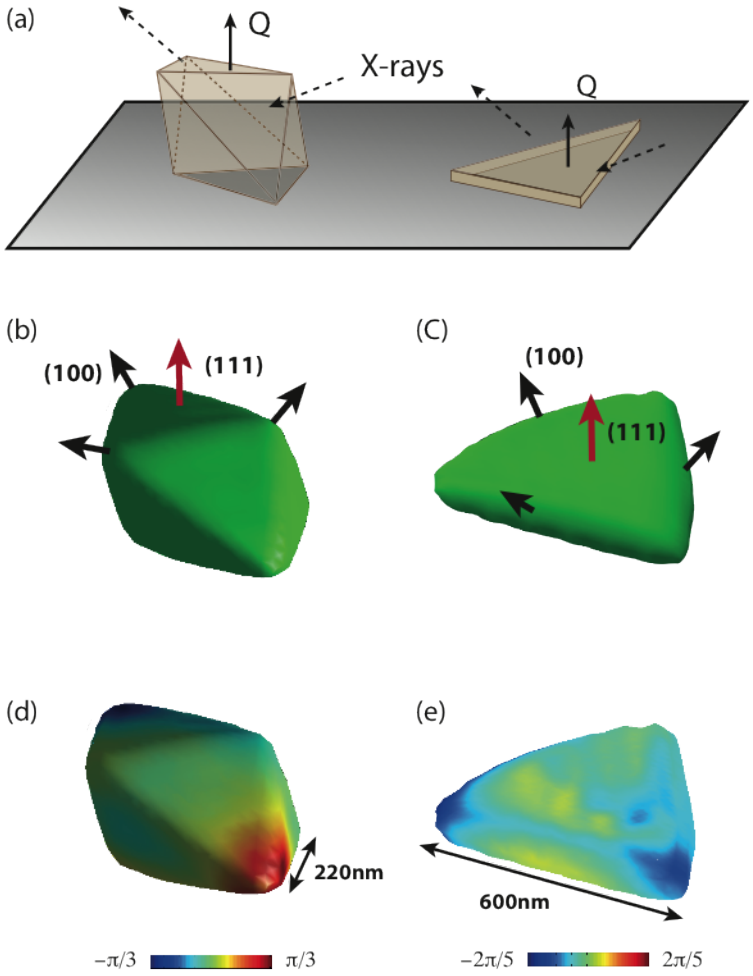

Figure 3.8. Reconstructed gold nanocrystals (a) The geometry of gold nanocrystals on a silicon substrate. The momentum transfer wave vector $\vec{Q}$ for the (111) Bragg reflection is oriented normal to the substrate. (b) and (c) Isosurfaces of the reconstructed shape for an octahedral nanoparticle and triangular plate. The normal directions of two sets of crystalline planes (111) and (100) are marked by red and black arrows, respectively. (d) and (e) The color represents the local value of the phase at the surface, indicating the presence of strain.

The phases were projected on planes containing 111 $\vec{Q}$. From those 2D phases, 3D strain distribution of the crystal along the 111 $\vec{Q}$ was calculated by taking the derivative of

the displacement field obtained form algorithmic phase reconstruction. This method lets us map the differential strain within each nanocrystal. It is sensitive to the displacement of a small fraction of the unit cell but will not be able to detect the full unit cell. However, this technique gives us a clearer view of strain in individual nanocrystal and the information presented is not the average of a number of crystals and is more accurate.

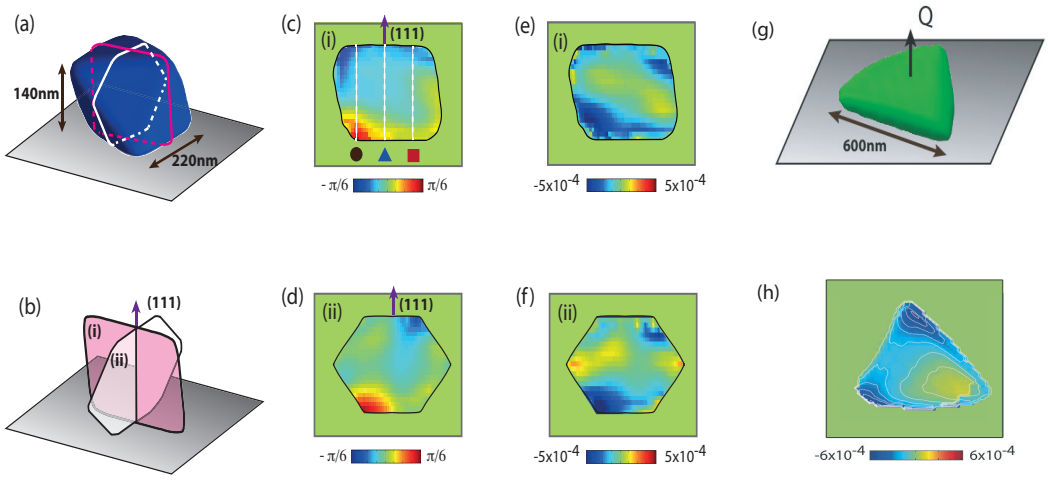

Figure 3.9. Strain within nanocrystals (a) The geometry of the nanocrystal and outlines of two cross-sections, (b) which are perpendicular to the bottom surface, and contain the 111 Q vec- tor. 2D phases on the cross-sections, depicted in (b), are shown in (c) and (d). Strain fields, calculated by the gradient of the displacement on plane (i) and (ii), are shown (e) and (f), respectively.(g) geometry and (h) strain along the normal to the basal plane of the triangular nanoplate, averaged over the depth.

As is evident from figure 3.9, the nanocrystals are strained much more at the corners and edges. These results are in good agreement with previous studies of strain distribution in metallic nanocrystals where locally rounded surface were under more compressive strain and the flat surface were relatively less strained [69]. Surface stress which lead to internal stress depends on the chemical composition of the crystal and forces acting at the interfaces due to neighbouring substrates, solvents and surfactants. In our growth enviroment, the difference in surface energies at Au/Air and Au/Si interfaces induces dissimilarity and hence strain. Furthermore, during the cooling period of the

growth, strain is induced by the different rates of thermal coefficients between the Au and the Si substrate.

The first part of this chapter has material verbatim from journal article [2] authored by me. The second part of this chapter is based on reference [3] which is work done in collaboration with J.W. Kim, S. H. Dietze, A. Ulvestad, R. Harder, E. Fohtung and O. G. Shpyrko.

3.2 Nickel and dime

Nickel nanomaterials attracts a lot of attention due to their unique ferromagnetic and catalytic properties. Research in ferromagnetic nanomagnets is driven by large potential application in memory and data storage [70–77]. Scientists are exploring memory applications and logic using magnetic vortices[78–80]. Significant research has focused on understanding the magnetic properties and control of a magnetic vortices which are generated in circular disks of ferromagnetic materials, which are typically fabricated using expensive lithography process. One of the first micromagnetic simulations were carried out on ferromagnetic cubes with uniaxial anisotropy which predicted vortices. Nanomagnets possess distinct properties compared to their bulk counterparts owing to their size and shape which are linked to their magnetic properties.[81–83] Understanding the influence of shape on magnetic properties can lead us to design nanomagnets tailored for specific applications. Towards this end we use a cost-effective single-step route for the synthesis of nanostructured Ni nanocubes using a thermal CVD method. By tuning the CVD growth parameters we can synthesize morphologically dissimilar Ni products including single-crystal cubes and horizontally and vertically-oriented nanowire arrays which form atop untreated amorphous SiO2 substrates[54, 55]. An understanding of the new properties that emerge in these nananostructured materials and their relationship to functionality will lead to for a broad range of magnetostrictive devices as well as other

catalysis [84], fuel cell [85], sensor [86, 87], and battery[88, 89] applications based on high surface-area transition-metal nanostructures.

3.2.1 Synthesis of Nickel nanocubes

We have synthesized single crystal Ni(001) nanocubes fabricated using in-house atmospheric-thermal CVD comprising of a lindberg blue furnace with a quartz tube installed. An Ar carrier gas is flowed through the quartz tubing using an MKS thermal mass flow controller while the downstream end of the CVD setup is closed off to outside atmosphere with a bubbler. Powdered $NiCl_2.6H_2O$ in a Ni boat is placed alongside SiO_2 Si substrate within a quartz tube which inserted inside the CVD furnace at 200°C for 10 mins. After that the temperature is increased to 650°C for another 10 mins. Then, the system is cooled to room temperature.

3.2.2 Characterization of Nickel nanocubes

The Ni nanocubes thus formed show well faceted single crystalline morphology as seen in the SEM and the AFM image in Fig 3.10 (a) and (b). AFM allows us to get a closer look at individual nanocube whose edge length is around 300 nm as shown in the line profile in Fig 3.10 (d). The coherent x-ray diffraction image shown in Fig 3.11 (a) with well defined periodic bragg peaks confirm the cubes being single crystal. We notice that these cubes are bounded by 100 planes. Ni has fcc crystal. According to Wulff's theorem, for an fcc crystal the surface energetic sequence is $\gamma_{111} < \gamma_{100} < \gamma_{110}$. This sequence implies that a single-crystal should take an octahedral or tetrahedral shape in order to maximize the expression of 111 facets and minimize the total surface energy. Wulff's theorem is applicable to free floating crystals devoid of external influences. However in our case, the crystals assemble on a substrate which plays a role in the kinetics of

crystal growth and favour the slightly more energtic 100 planes. The low temperature regime prefers the growth of cubes over octahedrons or nanowires by reducing the rate of ad-atoms arrival [54].

We use coherent x ray diffraction imaging technique to obtain three dimensional image of individual nanocube. The measurement was performed at 34-ID-C in Advanced Photon Source in Argonne National Laboratory. Using this technique we are also able to map the strain within each magnetic cube and calculate the internal strain. Coherent x-ray diffractive imaging (CXDI) is a technique that provides the overall shape of a nanostructure and the lattice distortion based on the combination of highly brilliant and coherent x-ray sources and phase retrieval algorithm [3, 7, 90–92]. The coherent x-ray diffraction pattern, which is measured at synchrotron source, is inverted to a complex function in real space. The amplitude of this function corresponds to the electron density in a crystal, and the phase can be interpreted as the deformation of the lattice onto the momentum transfer vector, which is determined by the direction of incident and scattered x-ray, of the Bragg peak[93].

3.2.3 Simulations

Magnetic characterization techniques like VSM and MOKE gives the average magnetic response that only indirectly reflects the underlying micromagnetic configurations. Micromagnetic simulations prove to be instrumental to understand the magnetic properties of individual nanostructures. Micromagnetic simulations are based on Landau-Lifshitz-Gilbert equation where the magnetization **M** under a local effective field **H** is

$$\frac{d\mathbf{M}}{dt} = -\frac{\gamma}{1+\alpha^2}[\mathbf{M}\times\mathbf{H}_{eff} + \alpha\frac{\mathbf{M}}{\mathbf{M_s}}\times(\mathbf{M}\times\mathbf{H_{eff}})] \tag{3.2}$$

where M is the magnetization vector, M_s is saturation magnetization, γ is the gyromagnetic ratio, and α is the damping constant. The effective magnetic field $\mathbf{H}_{eff}$ is comprised

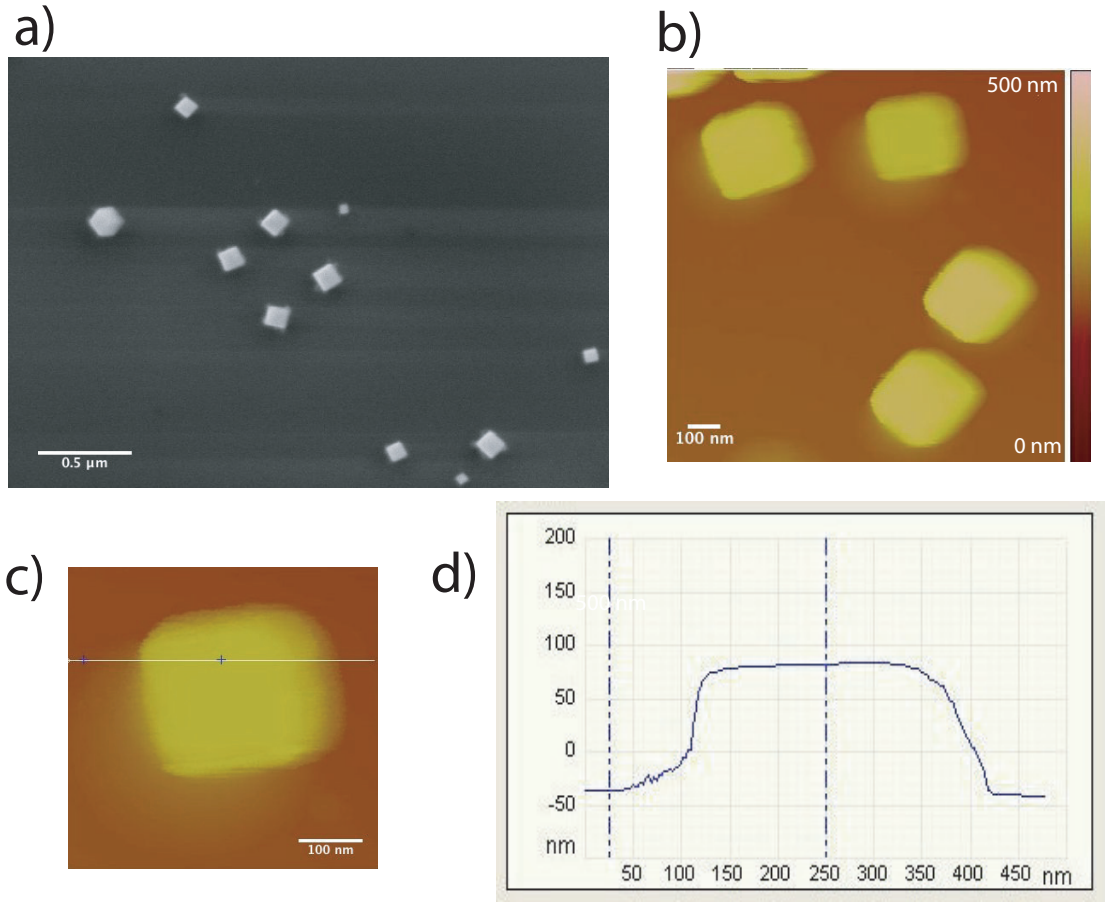

Figure 3.10. Structural characterization of Ni nanocubes (a) SEM images of Ni nanocubes as grown on $Si - SiO_2$ substrates (b) & (c) AFM images of Ni nanocubes as grown on $Si - SiO_2$ substrates which exhibit 100 facets. Ni has fcc crystal structure which enables Ni nanostructures to grow into cubes with higher surface to volume ratio which can lead to exciting applications like catalysis and topological vortices. In our cvd method, we generate only cubes. (d) Side profile of the height of individual Ni nanocube

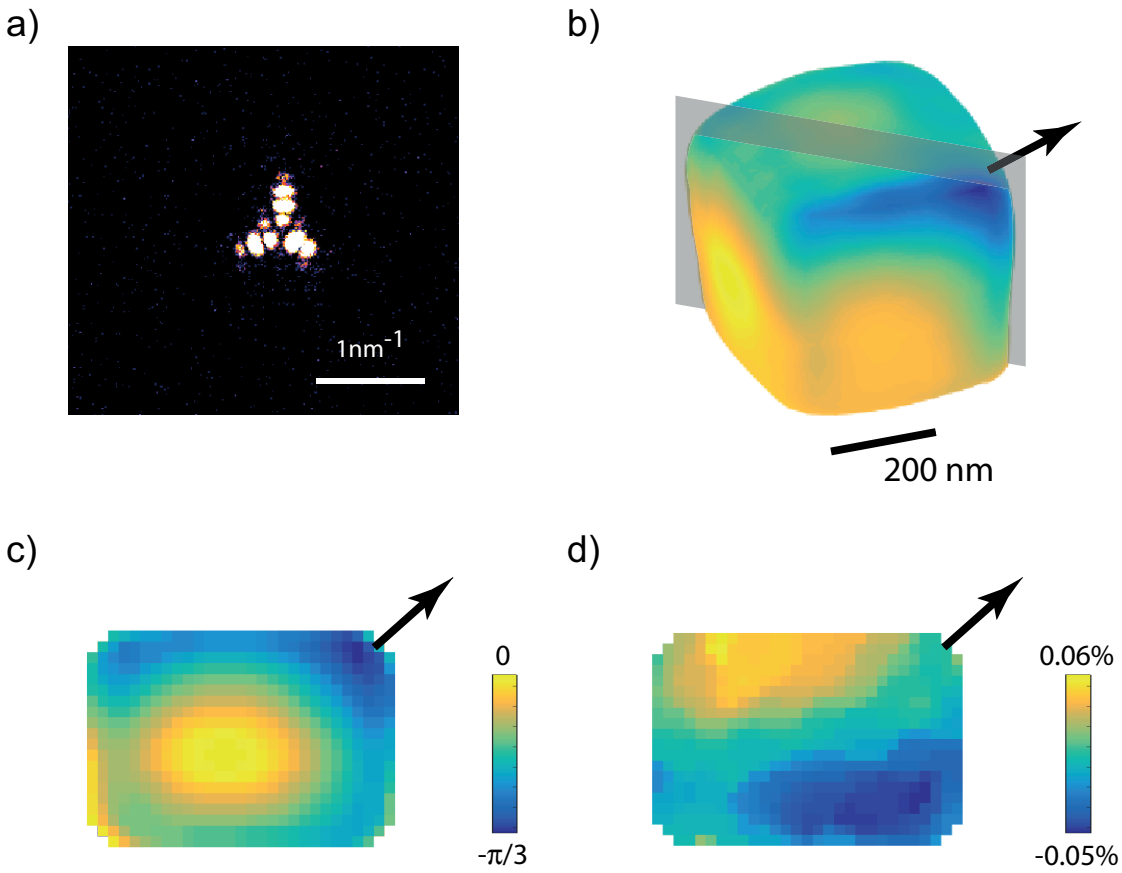

Figure 3.11. CXDI of Ni nanocubes (a) Coherent x-ray diffractive image on a detector (b) reconstructed shape of Ni nanocube, (c) and (d) the color represents the local value of the phase and strain at the surface, respectively. The black arrows are indicative of momentum transfer vector 111.

of the external field $\mathbf{H}_{Zee}$, anisotropy field $\mathbf{H}_{anis}$, exchange field $\mathbf{H}_{exc}$ and demagnetization field $\mathbf{H}_{demag}$.

$$\mathbf{H}_{eff} = \mathbf{H}_{Zee} + \mathbf{H}_{ani} + \mathbf{H}_{exch} + \mathbf{H}_{demag} \tag{3.3}$$

Anisotropy field in Eq. 2 is comprised of magnetocrystalline anisotropy and magnetoelastic anisotropy which arises due to the strain.

$$\mathbf{H}_{ani} = \mathbf{H}_{mc} + \mathbf{H}_{me} \tag{3.4}$$

Parameters used in our simulations are typical for nickel Ms = 484 emu/cm3 ; Aex = 1.05×10^{-6}erg/cm and cubic anisotropy with K_1 = -5$\times$ 10^4 erg/cm^3 and K_2 = -2$\times10^4$ erg/cm^3.The discretization elements were chosen to be tetrahedrons with 5 nm average edge length, which is lower than the exchange length which is 7.72 nm for nickel. The easy axis for nickel is along 111.

The magnetoelastic field component corresponding to stress state σ_{ij} and magnetostrictive constants λ_{100} and λ_{111} in cubic crystal can be expressed as

$$\mathbf{H}_l^{Me} = \lambda_{ijkl}^{M} \sigma_{ij} \mathbf{M}_k \tag{3.5}$$

$$\lambda_{ijkl}^{M} = \begin{cases} \frac{3}{2}\frac{1}{\mathbf{M}^2}\lambda_{100}(\mathbf{I}_{ijkl} - \frac{1}{3}\delta_{ij}\delta_{kl}), i = j \\ \frac{3}{2}\frac{1}{\mathbf{M}^2}\lambda_{111}\mathbf{I}_{ijkl}, i \neq j \end{cases} \tag{3.6}$$

where δ_{ij} is kronecker delta function and $\mathbf{I}_{ijkl}$ is the fourth order symmetric identity tensor.

Magnetostrictive constants for Ni are λ_{111}= -24$\times10^{-6}$ and λ_{100} = -46$\times10^{-6}$. σ= εE , where ε is strain and E_{Ni} is young's modulus of nickel (E_{Ni}=200GPa at room temperature). In our simulation, we assume uniform biaxial strain ε = -0.05% as the base

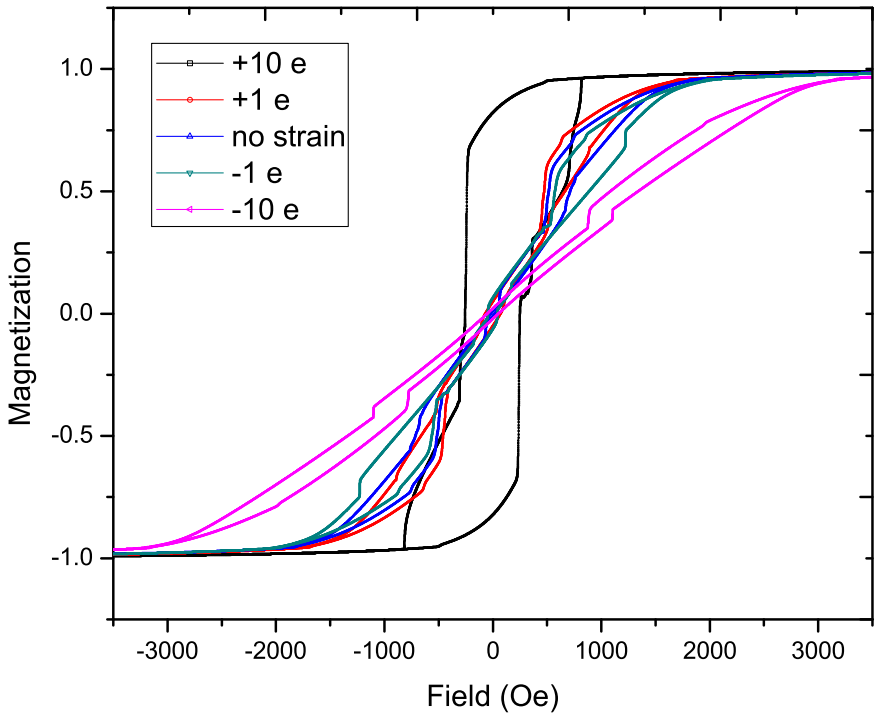

Figure 3.12. Simulations of hysteresis of nanocubes with strain. Comparison of hysteresis loops of cubes with varying magnitude of strain. The difference in the hysteresis curves is hardly noticeable for practical strains.

value using the compressive strain as calculated from CXDI (negative sign representing compression).

As shown in Fig 3.12, we observe no noticeable difference between the hysteresis loops in cubes with no strain and $+\varepsilon$ and $-\varepsilon$, but with $+10\varepsilon$ and -10ε, the change is considerable. Magnetostriction of nickel is negative, which entails that a compressive strain will create an easy axis in the direction of applied strain and tensile strain will create an easy axis perpendicular to applied strain. This explains the square coercive loop for $+10\varepsilon$ and thin loop for -10ε strain. The strain of the order of magnitude ε is what we expect in nanocrystals grown on substrate. 10ε is above the yield stress and hence

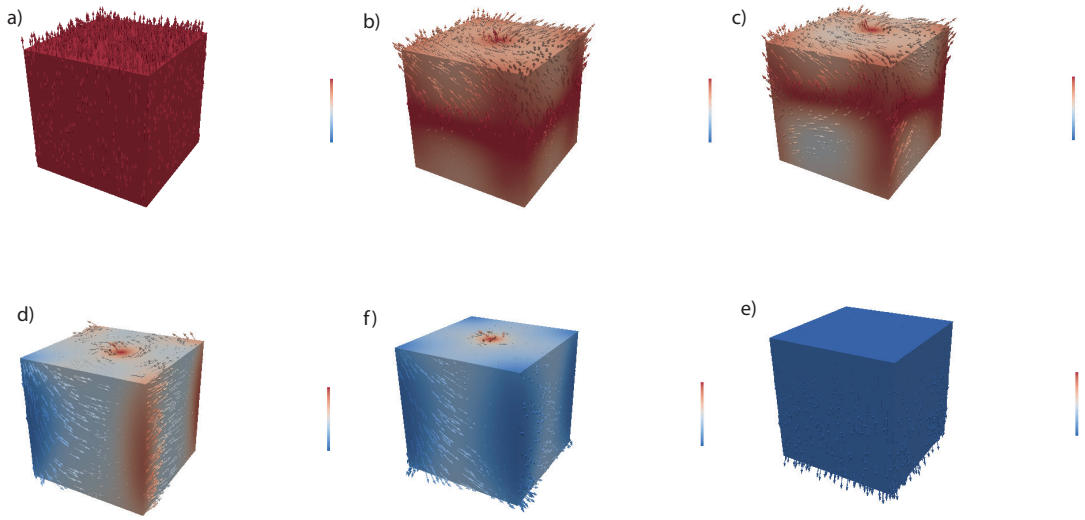

Figure 3.13. Evolution of vortices in a cube with edge length 200 nm at various fields during a hysteresis loop (a) 10,000 Oe (b) 1000 Oe (c) 600 Oe (d) -0 Oe (e) -600 Oe (f) -10,000 Oe. The cube has biaxial strain ε= -0.05%

unrealistic values of strain for nanocrystals. For all practical purposes, the strain does not affect the hystersis loops or the coercivity.

The modelling also predicts vortex at remnant state. The evolution of the vortices is shown in Fig 3.13. We notice that as the field reduces to zero (Fig 3.13(c) & (d)), vortices develop on the surface of the cube. And with the increase in field in the opposite direction, there is a change in chirality of the vortex core (Fig 3.13(e)). The presence of vortices at remanence can lead to interesting memory applications[94]. The remnant magnetic states differ with strain as shown in Fig 3.14. We notice the presence of vortices or antivortices on each side of the cube when there is no strain (Fig 3.14(a)). But with the application of compressive strain, the vortices and antivortices on the sides are suppressed (Fig 3.14(b)). With an even higher compressive strain (Fig 3.14(c)), we notice the magnetization wanting to be more inplane.

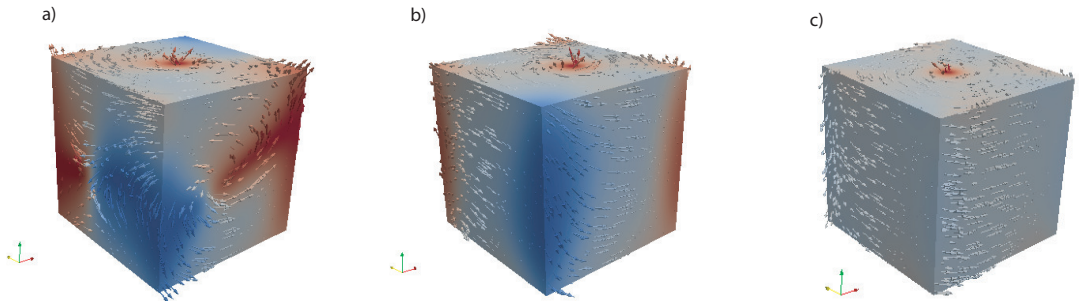

Figure 3.14. Remnant state magnetic configurations. Magnetic configuration of nanocubes at remnant state with (a) no strain (b) ε= -0.05% (c) ε= -0.5% . We notice the gradual dissapearance of vortices on the sides.

Chapter 4

One Dimension:Nanowires

Nanowires are nanomaterials where two out of the three dimensions belong to nanoscale. One - dimensional nanowires (sometimes also known as nanotubes or ribbons) generally have diameters in the nanometer range whereas the length ranges from microns to millimeters. The interest in nanowires is based upon the fact that one-dimensional systems should exhibit exotic phenomena due to the confinement of electrons in such a way, which leads to discrete energy states extending over large distances due to its length. The inherent anisotropy due to the shapy and a large surface to volume ratio make them enticing for a vareity of applications such as (i) spintronics, (ii) novel probe microscopy tips, (iii) nanoelectronics, (iv) nanophotonics, (v) quantum devices, (vi) energy storage, (vii) energy conversion, (viii) chemical and biological sensing, and (ix) nano-bio interfaces.

Semiconductor nanowires are the most versatile and hence the most researched one-dimensional nanomaterials. Compared to Carbon nanotubes (CNT's) and metallic nanowires, semiconductor nanowires have been predictibly synthesized in single crystalline forms with key parameters such as chemical composition, dimensions and electronic properties, in good control. Due to the precision in their fabrication, semicondcutor nanowires have been sucessfully integrated into various funcional electronic devices including crossed NW p-n diodes, crossed NW-FETs, nanoscale logic gates and

computation circuits, as well as optoelectronic devices such as nanoscale light-emitting diodes (LEDs) and lasers. Carbon nanotubes, invented by Iijima[95] nearly two decades ago attracted a lot of attention due to their inherent structure and strength. They were touted to be the next generation materials with which one could build space elevators. While they do indeed possess strengths 10-100 times higher than steel at fraction of the weight, the dream for space travel might be a little far-fetched due to the inherent defects. However, CNT are being used for various other applications such as drug delivery, catalysis and sensing applications.

Metallic nanowires have not been explored much since the early work on micron sized Fe, Co and Ni whiskers back in the '60s. Recent quest to develop nanoscale spintronic devices have revived an intrest in ferromagnetic nanowires which can be developed in spin valves[87, 96–98]. Stuart Parkin's brainchild racetrack memory[99] is based on the movement of domain walls in ferromagnetic nanowire. Most metallic nanowires which are grown now via electrodeposition or other template assisted techniques are polycrystalline and prove not much advantageous in terms of applications in the nanoelectronic applications where the polycrystallinity introduces defects in the wires. Our lab at CMRR succeeded in developing single crystal nanowires which grew vertically as well as horizontally atop SiO_2 with sharp (100) facets.

4.1 Estabalished Nanowire Growth Mechanisms

4.1.1 Vapor-Liquid-Solid (VLS)

The most cited paper regarding one dimensional growth of nanowires was written by Wagner and Ellis in the 1960s where they introduce the concept of Vapor-Liquid-Solid (VLS) growth mechanism[100]. They noticed that these 'whiskers' needed (a) an impurity or catalyst which lead to the formation of a (b) liquid-alloy droplet of low

freezing temperature. This liquid droplet became a preferred site for the deposition from the vapor, which after supersaturation grew out of the droplet. The advantage of this method is the ability to grow dislocation free crystals.

The primary feature of the VLS mechanism is the trasformation of the material from vapor to liquid to solid in that order. The presence of catalyst or impurities is another requirement so that the material to be grown and catalyst can form a solution with a eutectic temperature within suitable temperature range. Prior to the introduction of the precursor vapor, the catalysts/impurities should melt into small droplets onto the substrates where the deposition of the material can take place. Upon contacting the liquid, reactant species will be adsorbed and diffuse quickly untill supersaturation is reached, after which they will precipitate out of the droplet and grow vertically. Researchers at Hitachi around 1992 applied VLS mechanism with gold catalysts to grow III-V nanowires [101] which lead to nanowire based LED revolution.

The kinetics of silicon 'whisker growth' by VLS mechanism was carried out in detail by Givargizov et. al[102] and determined the dependence of axial growth rate on whisker diameter. He claimed that supersaturation, which is a measure of the driving force due to Gibbs-Thomson effect an be expressed as chemical potential difference as follows.

$$\triangle\mu = \triangle\mu_0 - (4\alpha\Omega/d) \tag{4.1}$$

The chemical potential difference ($\Delta\mu$) is that between the Si in vapor and in solid phase (in the whisker), the initial potential difference prior to precipitation is indicated by $\Delta\mu_0$, Ω is the atomic volume of Si and α is surface energy of the whisker. As the diameter decreases the supersaturation decreases and hence the growth rate decreases. Therefore, a nanowire with large diametere grows more rapidly than a nanowire with a smaller diameter.

Referring back to the driving force- vapor saturation relationship, the dependence of the growth rate V on supersaturation $\Delta\mu/kT$ is unknown a priori and must be determined from experimental data.

$$V = b(\Delta\mu/kT)^n \tag{4.2}$$

where b is coefficient independent of supersaturation and n(~ 2) is the empirical fitting factor.

The critical diameter for a nucleus to be stable and grow into a nanowire is given by

$$d_c = 4\Omega\alpha/\Delta\mu_0 \tag{4.3}$$

However the presence of catalysts/impurities in the initial droplet accounts for the differences in surface energies and hence, diameters lower than the critical diameters are possible. The VLS mechanism is a general phenomenon in vapor crystal growth widely occuring in nature even on the Moon [103]. Even platelets can grow via VLS mechanisms.

4.1.2 Vapor-Solid (VS) mechanism

One dimensional growth of nanocrystal growth is possible in the absence of an external catalyst/impurity described in the VLS mechanism. Many instances of nanowire growth via direct sublimation of vapor phase reactants have been reported in literature[104–106]. In many cases this unidirectional growth is due to the intrinsic anisotropy of the crystal like with materials having a hexagonal crystal structure grow along the c-axis direction. Another instance of one-dimensional non-VLS growth involves the restriction of specific surface facets due to crystallographic orientation. A surfactant or capping layer in the growth enviroment may attach to one of these crystallographic

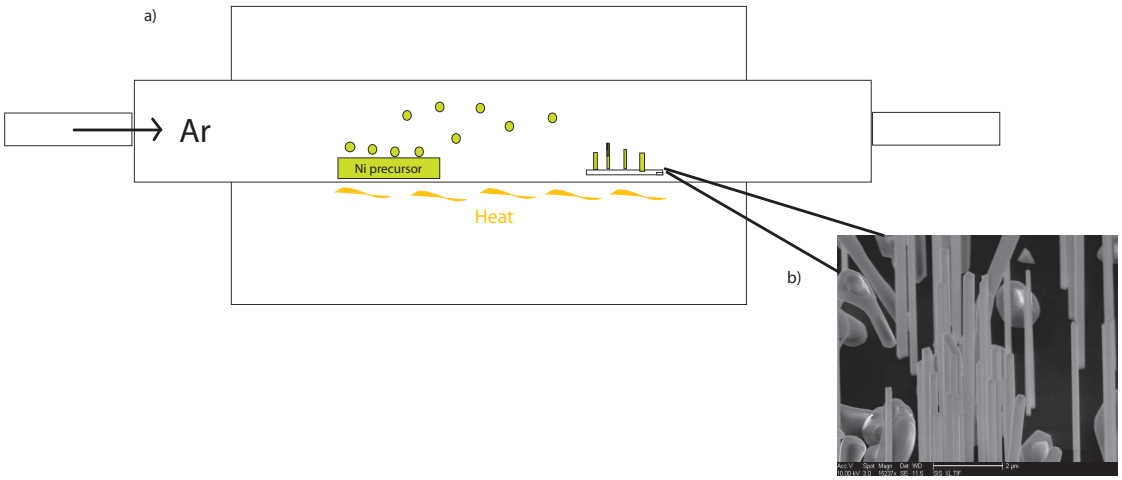

Figure 4.1. Schematic of growth of Ni nanowires via CVD

facets causing one-dimensional growth.

4.2 Synthesis of single crystal Nickel Nanowires

Nickel 'whiskers' were synthesized empirically back in the 1960s and the overall mechanism was explained by Cech[107]. He used nickel halide with moisture as starting precursor which could be quickly heated to a temperature where the halide is volatile and in an atmosphere with H_2.

$$\mathrm{NiX_2 \cdot 6\,H_2O(s)} \longrightarrow NiX_2\mathrm{(g) + 6\,H_2O(g)}$$

where X = Cl, I, F, Br

$$\mathrm{NiX_2(g) + H_2O(g)} \longrightarrow \mathrm{NiO(s) + 2\,HX(g)}$$

As heating continues and with continuous pumping of inert argon gas, most of the water is driven away and makes the enviroment more reducing in nature. The hydrogen produced from the side reactions proceed to reduce the NiO to pure Ni.

$$\mathrm{H_2(g) + NiO(s)} \longrightarrow \mathrm{Ni(s) + H_2O(g)}$$

We use this general method in our in-house CVD chamber using $NiCl_2.6H_2O$ as the halide precursor and Argon as the carrier gas. By first adding a baking step where the

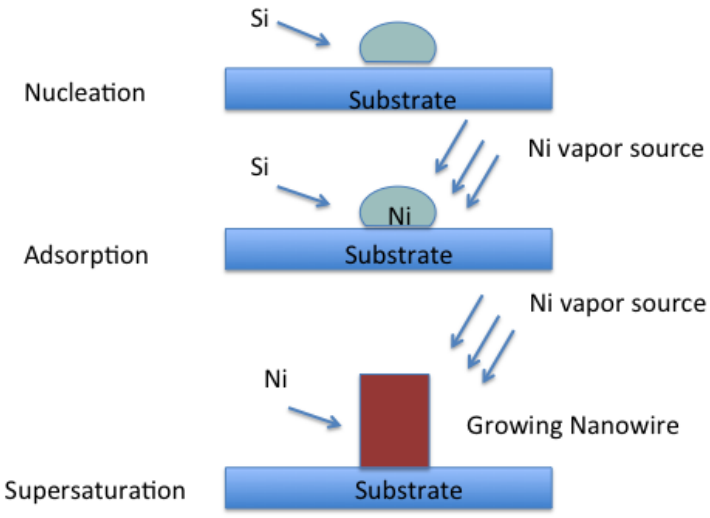

Figure 4.2. VLS growth mechanism of Ni nanowire

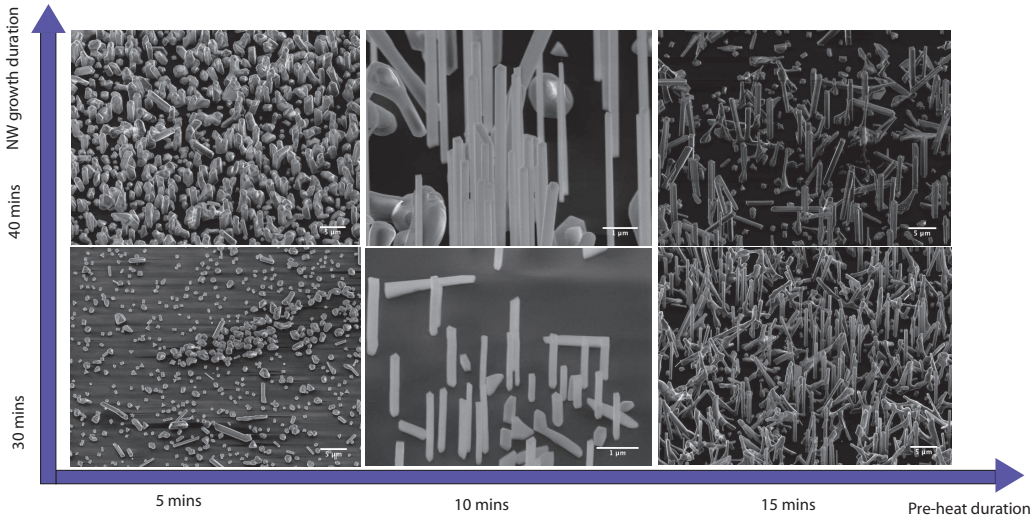

Figure 4.3. Optimizing nickel nanowire growth by changing the pre-heat baking time and growth time

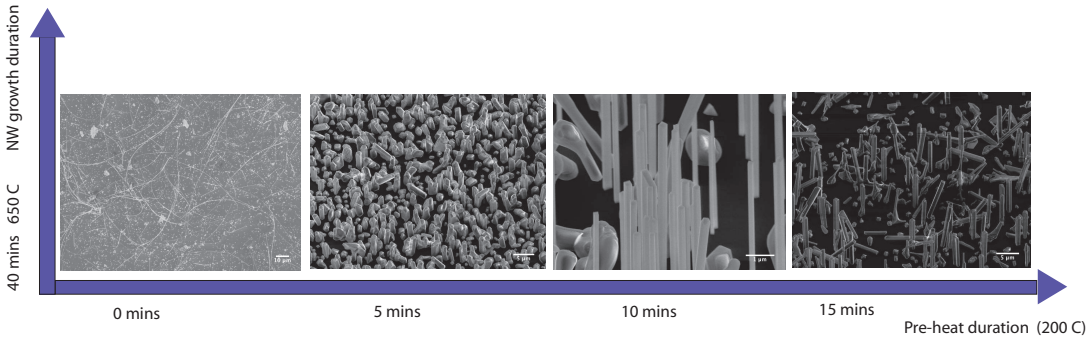

Figure 4.4. Effect of reducing moisture in the precursor by increasing pre-heat duration

precursor is heated at 200°C, we can play with the amount of moisture in the reaction enviroment. Then the temperature is ramped up to 650°C and the growth is allowed to occur for 30-40 mins, after which the system is allowed to cool down to room temperature while still flowing argon gas through it. Argon is flowed through the CVD system at a typical rate of 10 sccm during Nanowire growth. The other end of the quartz tube is connected to the exhaust through a water bubbler. The role of the water bubbler is two-folds, one acting as a visual means to check on the argon flow due to the creation of bubbles, the other being to provide some vapor pressure in the system needed to create a reducing enviroment. The parameters which we changed were the duration of pre-heating to control the moisture in the precursor, the total growth time and the substrates on which the material were deposited. The nickel nanomaterials were grown on thermal oxide SiO_2-Si substrates. The optimal conditions for the vertical nanowires to grow were heating the precursor at 200°C for 10 mins then ramping the temperature at 650°C and let the growth occur until 40 mins as shown in Figure 4.1. Without any pre-heating step, we get horizontal nanowires. This indicates the role of the moisture in the precursor as a key feature in the formation of vertical nanowires.

4.3 Interplay of superconductivity and ferromagnetism

Heike Kamerlingh Onnes[108] won the race to make liquid Helium which led to the discovery of superconductivity in mercury in 1911. However the first phenomenological theory to be widely accepted was postulated by Fritz and Heinz London[109]. Only in 1957, a microscopic theory explaining superconductivity was devised by Bardeen, Cooper and Schrieffer more commonly known as the B.C.S theory[110]. Superconductivity is the phenomenon of exactly zero resistance and expulsion of magnetic flux in certain materials below critical temperature. According to the B.C.S theory, electrons in superconductors with anti-parallel spins and opposite momenta pair up to form Cooper pairs, which are held to each other via the exhange of lattice vibrations also known as phonons. The characteristic decay length of the Cooper pair is known as its coherence length ξ. Just like any other phenomena, when the dimensions are reduced, interesting effects with novel applications arise. For instance, what happens when one or more dimensions of the material are smaller than the coherence length of the Cooper pairs? According to Hohenberg-Mermin-Wagner theorem, fluctuations should destroy superconducting order even at low temperatures in reduced dimensionality. What happens if a superconductor is placed next to a metal nanowire? Or a ferromagnetic wire? These questions have been raised and explored just out of curiosity as well as for futuristic applications such as quantum computing.

Cooper pairs leak when a superconductor is in good electrical contact with a normal metal, thereby making the normal metal also superconducting to a certain extent. This phenomenon is known as superconducting proximity effect and the distance to which the Cooper pairs survive is known as the range of the proximity effect. This range in normal metals can be as long as $\sim 1\mu$m. Even in one-dimensional nanowires of normal metal, like gold, the range can be very long as was demonstrated by Wang

et al. where gold nanowire of length 1.2 μm becomes superconducting when current is passed through W leads[111]. However if the material next to superconductor is ferromganetic, this range is not supposed to last more than few nanometers. This is because the spins of electrons in a ferromagnet are alligned parallel to each other. The exchange order in a ferromagnet prevents the antiparallel pairing up of Cooper pairs. This expectation has been confirmed in macroscopic (Fe, Ni)-In junctions [112] and submicrometre Ni-Al structures [113] where the spatial range of the proximity effect is limited to few nanometers. However, in reduced dimensional mesoscopic ferromagnetic-supercondtor structures, long ranged-proximity effect have been found[114–118]. For instance, supercurrent has been detected in half-metallic ferromagnetic CrO_2 thin film sandwitched between two superconducting leads separated by 1μm[119].

Recently long range proximity effect was demonstrated in a 600 nm long Cobalt nanowire when current was passed through superconducting tungsten leads[120]. Longer wires($> 1\mu$m) in the same experiment do not become fully superconducting. The nanowires were made via electrodeposition in templates which could lead to the production of polycrystalline nanowires. The electrodes were made by focused ion beam. They also measured nickel nanowires made by the same process but the resistance did not become exactly zero in those wires. The long range proximity in such systems have been theorized to be attributed to the spin triplet rather than the spin singlet state. The formation of spin triplet requires the presence of a region with inhomogenous magnetization.

In a similar quest to observe long range proximity effects, we patterned the single crystal nickel nanowires that we made using CVD. These single crystal nanowires show chiral domain structures when probed with photoemission electron microscopy (PEEM) (shown in Fig 4.5 (a)) which imply the presence of inhomogenous magnetization. Simulations were performed in Fastmag to understand the periodic patterns (Fig 4.5 (b)). It turns out that periodic pattern was in fact a periodic array of alternating chirality

vortices. In simulations, the pattern is dependent on the field history as shown if Fig 4.6. For the periodic pattern to form in simulations, the nanowires need first to be saturated under a field, then the field needs to be reduced to some value before being abruptly turned off. Thus it seems that in experiment the periodic pattern is the ground state, but in the simulations it is a metastable state. In fact, the ground state in simulations is a single vortex domain across the entire nanire Fig 4.6 (a). It is unclear what the origin of the discrepancy between simulations and experiment is. Including other anisotropy terms including magnetoelastic effects seem to help stabilize vortices at room temperature (Fig 4.6(c). In principle that should allow for long range proximity to exist.

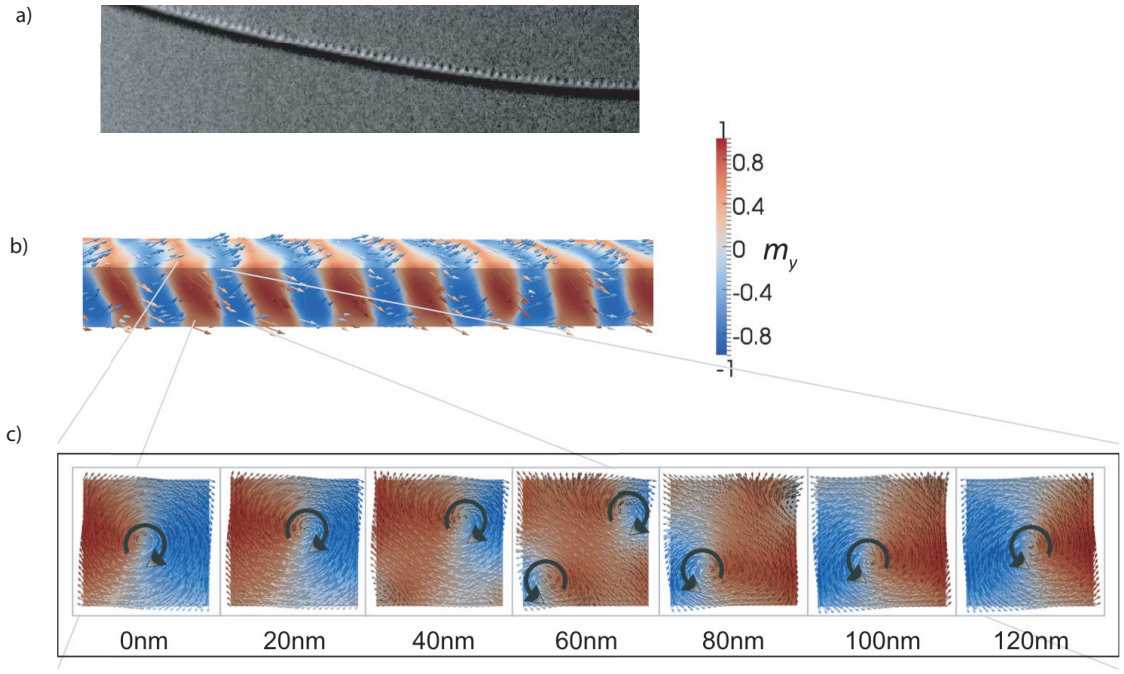

Figure 4.5. Inhomogenious magnetization in Ni nanowires (a) PEEM image of Ni nanowire showing periodic domain pattern (b) Simulations reproduce this periodic pattern (c) closer look at the simulations show that periodic pattern is periodic array of alternating chirality vortices

Figure 4.6. Inhomogenious magnetization in Ni nanowires. Depending on field history three magnetization configurations are possible (a) Uniform vortex is obtained by gradually reducing the applied field in the transverse direction to zero. This is ground state (b) Periodic array of alternating chirality vortices is obtained by cutting the transverse field off at 1 kOe. This is a higher energy state due to DWs. (c) Non-periodic array of alternating chirality vortices is obtained by relaxing the system from saturated state in the absence of field. This is intermediate energy state due to some DWs. In all three situations, there is inhomogeneity in magnetization

4.4 Fabrication of superconducting contacts

To make the superconducting contacts we pattern the nanowires with Niobium (Nb) metal using photolithography and magnetron sputtering. Few of the nickel nanowires grown on substrates were transferred mechanically on top of insulating substrates like sapphire and more commonly used and cheaper SiO_2/Si substrates. Just like any lithographic process, a photoresist is coated using a spinner. Depending on the mask which is used we need to pick either a positive or negative resist. In our case, we chose a negative photoresist. A lot depends on the type of resist used, the speed and time at which the

substrates with the resist is spun as it determines the thickness of the resist. The thickness of the resist affects the resolution of the features of the pattern. Various mechanisms are used in UV exposure, but in the case of negative photoresist such as the NR9 or NR7, exposure to UV light causes breaks in the polymer chains and changes the chemistry of the photoresist. Although the photoresist is not physically broken down by the exposure, it allows for chemical differentiation between exposed and nonexposed areas by either promoting or inhibiting solubility in a developer solution.

After exposure, a postexposure bake step using a hot plate or oven heating is used to complete the chemical transformations initiated by the UV exposure. In this step, broken polymer chains can cross-link and form chains that are insoluble to a specific developing solution. The samples can then be immersed in the developer solution that removes the soluble resist while maintaining the insoluble areas prescribed by the pattern mask.

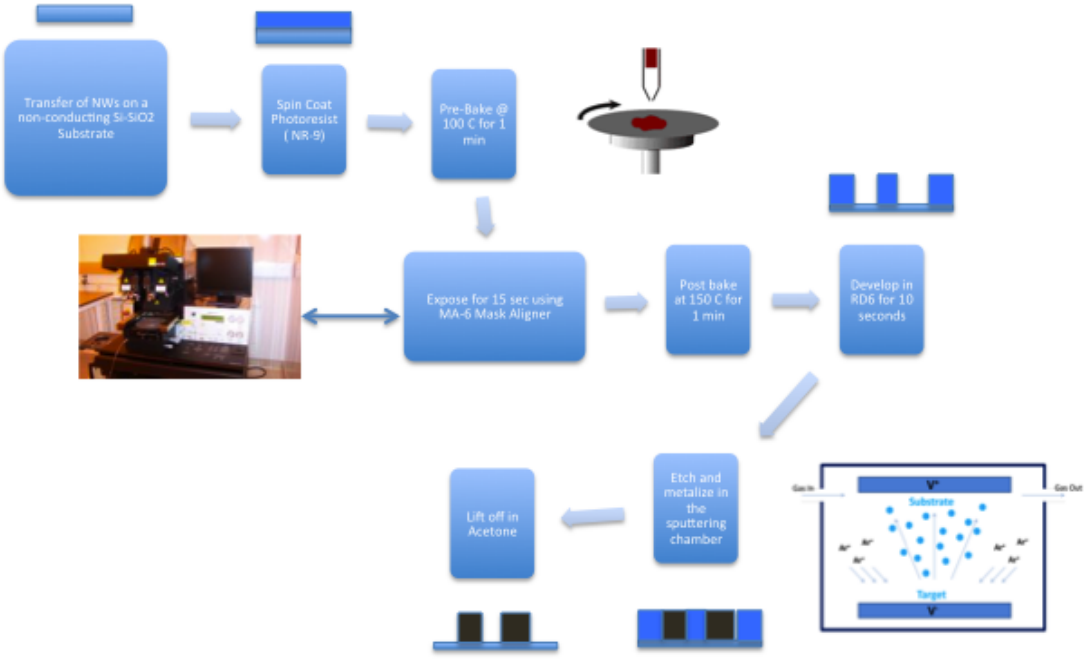

Figure 4.7. Schematic of patterning process

At first, we patterned the nanowire with only two contacts, one at each end of the nanowire. We used the NR9-3000PY resist. Negative Resist NR9-3000PY is a negative tone photoresist designed for 365 nm wavelength exposure. The resist was coated on substrates using a spinner at 4500 rpm for 40 seconds. The resist-covered substrates are then pre-baked on hot plates at 150°C for 1 minute. Then the nanowires were aligned under the mask using Karl Suss MA6 Mask Aligner. The substrates were in hard contact with the mask so there would be little mis-alignment. The substrates with nanowires and resist were then exposed for 20 seconds. After the exposure, hard bake at 100°C for 1 minute was carried out. These substrates were then developed in RD6 solution for 10 seconds subsequently. The pattern with huge contact pads at each end of the wire is easier to obtain since the pads are far apart from each other.

To pattern the nanowires with four contacts is however trickier and needed a bit of process engineering. The pattern available to us in the mask, the separation of inner contacts is around $\sim 1\mu$m which is hard to resolve using optical lithography. To achieve this, we used a thinner resist so that the shadow effect can be reduced. We used NR7-1500Y and spin-coated at 6000 rpm for 40 seconds. After a soft bake for 150°C for 1 minute, the substrates were aligned with the MA6 mask aligner under hard contact with the mask and exposed for 20 seconds. Then the substrates underwent hard bake for 100°C for 1 minute. The patterns were subsequently developed in RD6 solution for 10 seconds.

After the development process, the samples were rinsed with DI water and then dried. The samples underwent plasma clean inside the sputtering chamber before the deposition. The RF argon sputter clean ensures the removal of the leftover resist and also the few nanometer thick oxide layer on top of nanowire. The cleaning was done with RF power of 25W for about 1 minute. After that Nb was deposited for 10 minutes with 300W power. The average thickness of the Niobium deposited was around 80 nm.

The lift-off process was carried out using acetone in plastic vials. Each sample was kept in separate vial to prevent destruction of the nanowires during the shaking process. After each step of this process, the samples were observed under optical microscope to see if the nanowires were not displaced.

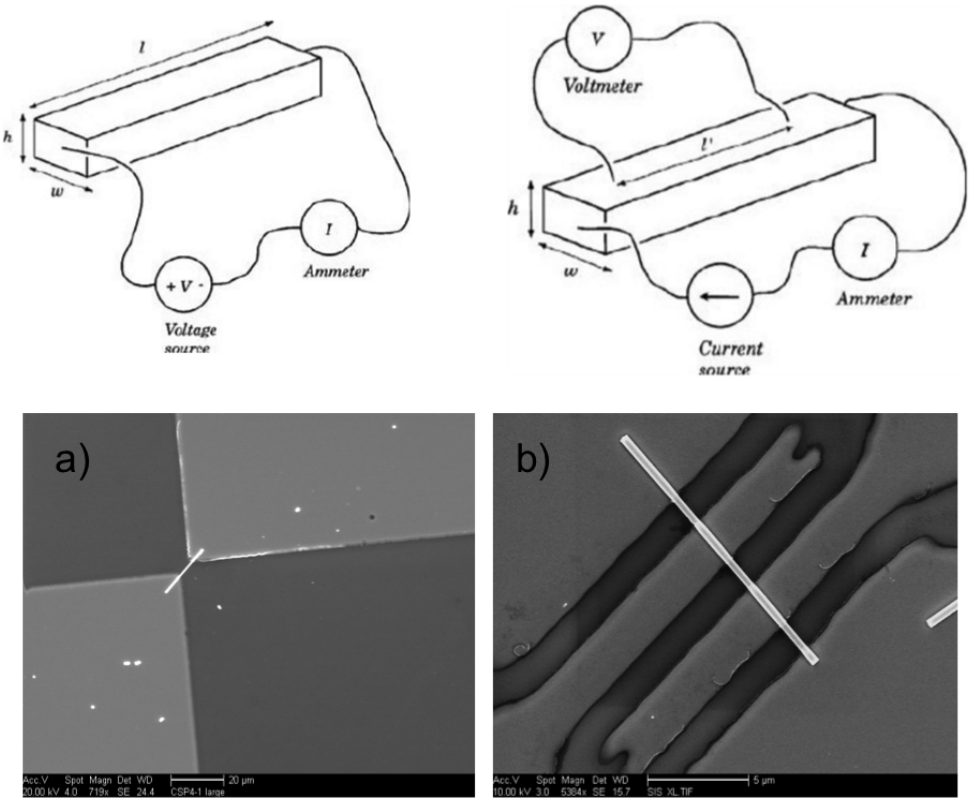

Figure 4.8. (a) Two-wire measurement (Separation between leads $\sim 7\mu$m) (b) Four-wire measurement (Separation between leads $\sim 1.6\mu$m)

The main difference between two-wire vs. four wire resistance measurements also known as kelvin probe measurements is the accuracy. The main measurement issue with the two-wire method is that total contact resistance is added to the measurement. The main current causes a small but significant voltage drop across the nanowire and the Nb contact pads. So any minor changes in magneto-transport measurements will be too obscure to observe.

To eliminate substantial contact resistance, we employ four wire measurements

which is more accurate than the former method. Here the outer two contacts are the current leads and the inner two contacts are voltage lead. In this configuration when the current is passed through the nanowire and inner leads, the voltage drop is measured only across the nanowire with the inner two leads, hence, eliminating most of the contact resistance.

4.5 Magnetoresistance

Magnetoresistance is the phenomenon where the resistivity of a material changes with the application of an external field. Depending on the type of material magnetoresistance can be categorized into ordinary or lorentz magnetoresistance and anisotropic magnetoresistance.

4.5.1 Ordinary Magnetoresistance

Ordinary or Lorentz Magnetoresistance is experienced by all metals. This effect is quite low at low fields but increases with increase in fields ($\sim B^2$). This effect is due to the curving of the electron trajectory by the lorentz force. It is very small in most metals except at low temperatures.

4.5.2 Anisotropic Magnetoresistance

Ferromagnetic materials experience anisotropic magnetoresistance. The inherent magnetization of the ferromagnets couples with the electron flow to produce an enhanced effect. This effect is much larger than OMR and can be as large as 4-6 % in certain materials. The origin of AMR lies in spin-orbit coupling. The electron cloud about each nucleus deforms slightly as the direction of the magnetization rotates, and this deformation changes the amount of scattering undergone by the conduction electrons when traversing the lattice. If the field and magnetization are oriented transverse to the

current, then the electronic orbits are in the plane of the current, and there is a small cross-section for scattering, giving a low resistance state. Conversely for fields applied parallel to the current, the electronic orbits are oriented perpendicular to the current, and the cross-section for scattering is increased, giving a high resistance state.

4.6 Results

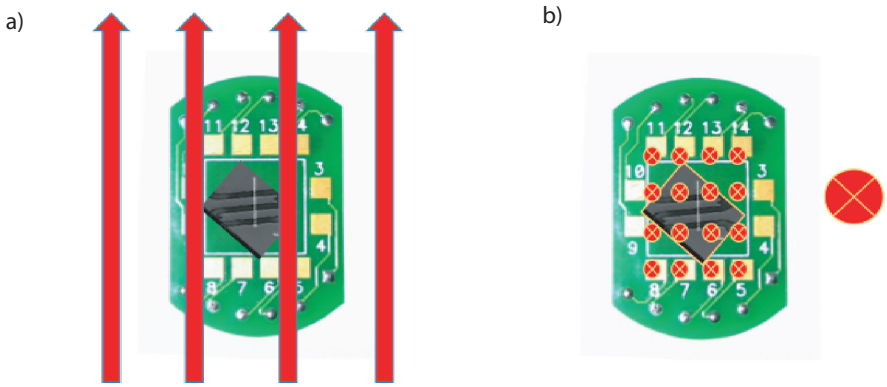

Figure 4.9. Measurement configuration (a) Inplane or parallel measurement configuration (b) out of plane or perpendicular measurement configuration

Magnetic characterization of single nanowire is implemented by anisotropic magnetoresistance (AMR) measurement[121].Electrical characterization of individual nanowires were carried out using the transport option in a Quantum Design Physical Property Measurement system. In ferromagnetic materials, electrical resistivity depends on a relative angle θ between the magnetization (M) direction and the current (I) flow direction according to $\rho = \rho_{\parallel} - (\rho_{\parallel} - \rho_{\perp})sin^2(\theta)$ where ρ is the total resistivity and $\rho_{\parallel}$ and $\rho_{\perp}$ are the resistivities for the magnetization parallel and perpendicular to the current

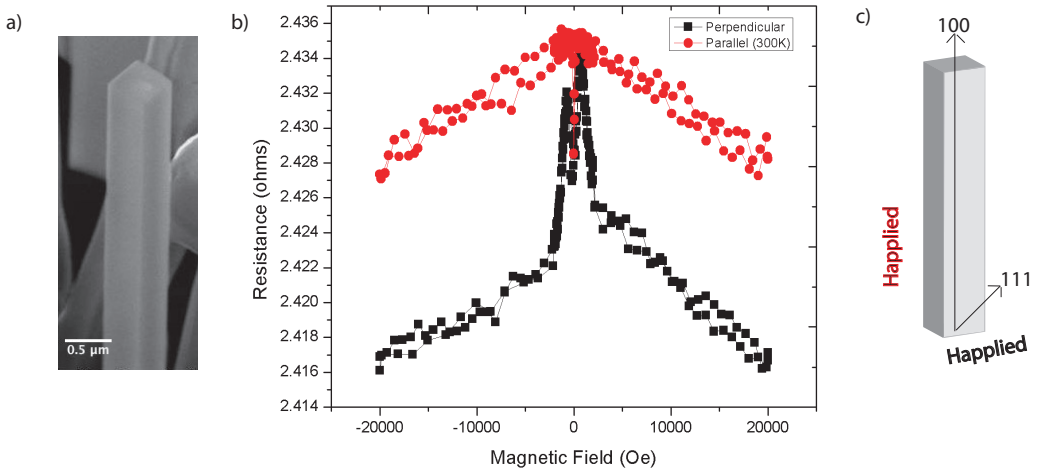

Figure 4.10. AMR of single crystal nanowire at 300K (a) SEM image of a single crystal nickel nanowire with cubic 100 facets (b) AMR curve of single crystal nickel nanowire at 300K. The swiching field is around 700 Oe. (c) Schematic of a single crystal nickel nanowire and how the field is applied during transport measurements relative to its crystallographic directions.

direction, respectively [122, 123]. Applied magnetic field was swept from 20 to -20 kOe and back at various temperatures below and above 9K (T_c for Nb contacts) while applying 0.01 mA of current for magnetoresistance measurements with the nanowire oriented both parallel and perpendicular to the direction of applied magnetic field as shown in Fig 4.10(c). Shown in Fig 4.10(b) is the typical AMR response for a single crystal-ferromagnetic wire at room temperature[124]. The AMR curves are nearly reversible (i.e., independent of field history) with sharp switching. The switching field of the nanowire is around 700 Oe. The nickel nanowires synthesized and measured by us are single crystals which grew vertically on the substrate along $\langle 100 \rangle$ (Fig 4.10(a)). Nickel is fcc and it's easy direction of magnetization is along $\langle 111 \rangle$. The origin of this behavior results from the competing shape anisotropy of the nanowire, which favors magnetization along the nanowire axis $\langle 100 \rangle$, and the magnetocrystalline anisotropy, which favors magnetization along the $\langle 111 \rangle$ crystallographic direction.

When we look at the case where the field is applied perpendicular to the wire as shown in Fig 4.9(b), at high fields the magnetization points in the same direction as the applied fields, hence the magnetization is perpendicular to the current flow. The resistance is lowest in this case. As the field decreases back to zero, the magnetization orients somewhere between $\langle 100 \rangle$ and $\langle 111 \rangle$. As the field is increased in the negative direction, the magnetization switches direction and then reorients to align with the applied field.

In the case when the field is applied parallel to the wire as shown in Fig 4.9 (a), the magnetization of nanowire at high fields should align with applied field which is along the length of the wire. The resistance should be the maximum at this point. However we notice that the resistance decreases slightly with high fields and that is due to the reduction in electron-magnon scattering induced by damping of spin waves[125]. As the field is reduced, the magnetization of the nanowire orients towards an angle between $\langle 100 \rangle$ and $\langle 111 \rangle$, i.e the same state when the field is zero even when the field applied was perpendicular. The resistance in this case is the lowest and should meet the AMR curve where the direction of field is orthogonal to the nanowire. This trend is typical of a single crystal wire. Had it been a polycrystalline wire, the magnetization would be along the length of the wire always and the resistance would not change when the field is applied parallel to the wire.

Nb is a s-wave superconductor with T_c of 9K [126]. We confirmed the T_c of the sputtered Nb strip by doing a 4 probe kelvin measurement to be 9K as shown in Fig 4.11 (a). Fig 4.11 (b) shows the evolution of the critical fields at various temperatures for Nb strip. The thickness of sputtered Nb strip was maintained at 80nm same as the thickness of the Nb contacts sputtered on nanowires. The critical field reduces as the temperature approaches T_c.

We present a systematic 2-wire and 4-wire measurement study on single crystal

nanowire synthesized via chemical vapor deposition using Nb leads which has Tc around 9K. The Ni NWs, which we measured, are ∼500 nm in diameter and ∼10 um long which is much larger than the Co wire measure by Wang et al.

4.6.1 2-wire measurements

The separation between the two Nb contact pads on top of the nanowire are constant in our measurement which $\sim 7\mu$m. The nanowires that we could pattern with photolithography are $\sim 10\mu$m and longer with average diameter of $\sim$ 500nm.

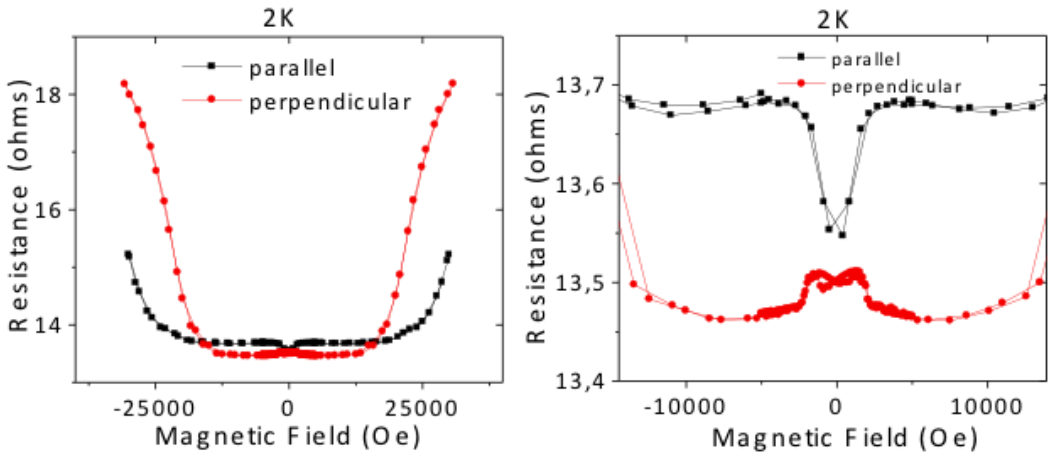

Figure 4.12. Two-wire AMR of Ni nanowire at 2K

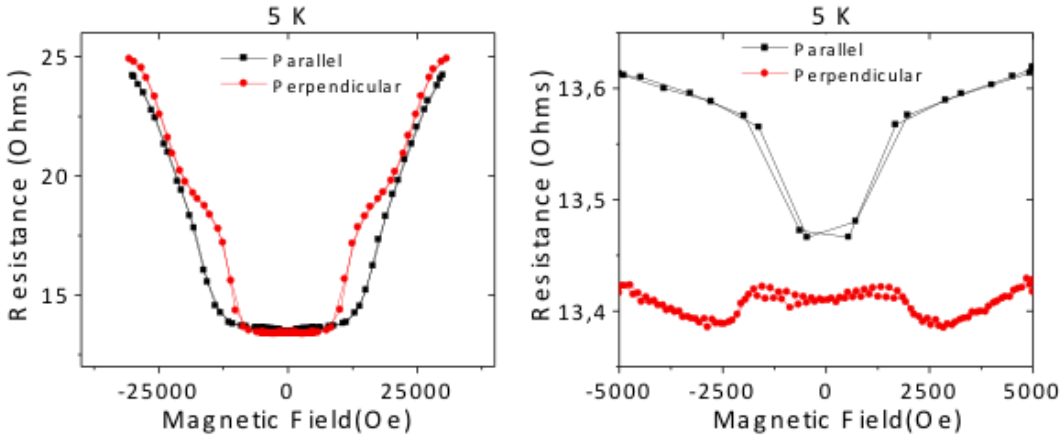

Figure 4.13. Two-wire AMR of Ni nanowire at 5K

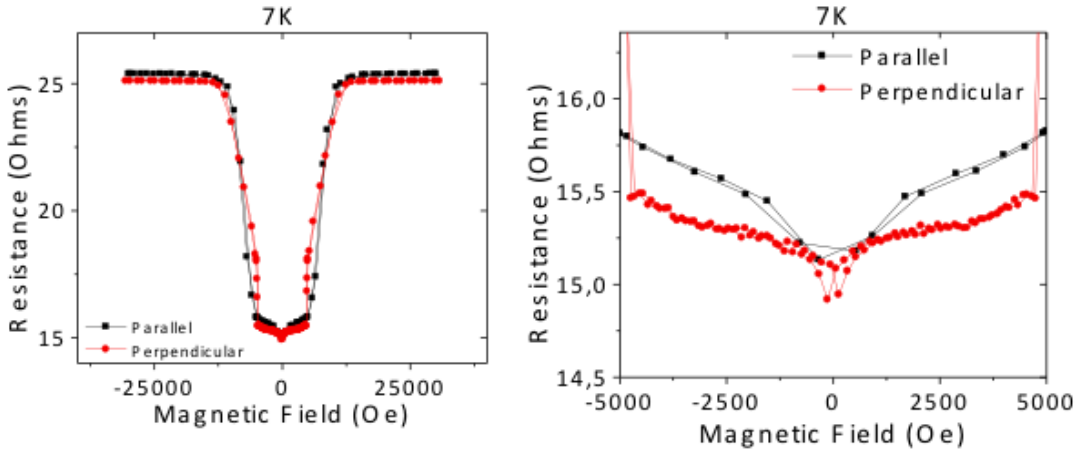

Figure 4.14. Two-wire AMR of Ni nanowire at 7K

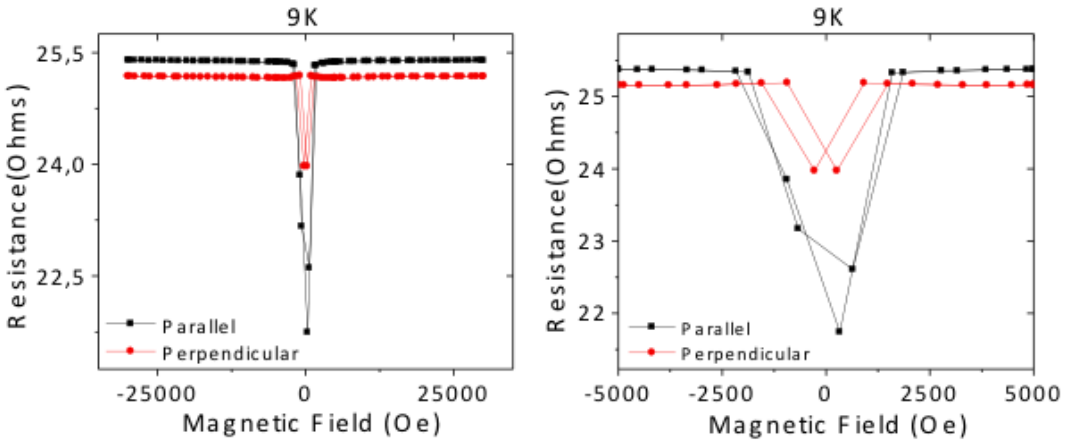

Figure 4.15. Two-wire AMR of Ni nanowire at 9K

We observe that at well below the superconducting transition temperature, the Ni NWs show ferromagnetic AMR signature, the anomaly being around the transition temperature (7K-9K) where we observe an inverse effect. The Ni NW shows expected AMR behavior at 2K, 5K and 11K. Around the transition temperature of the superconductor Nb (9K), the behavior is anomalous. The superconducting effect seems to be masking the ferromagnetic nature at the transition.

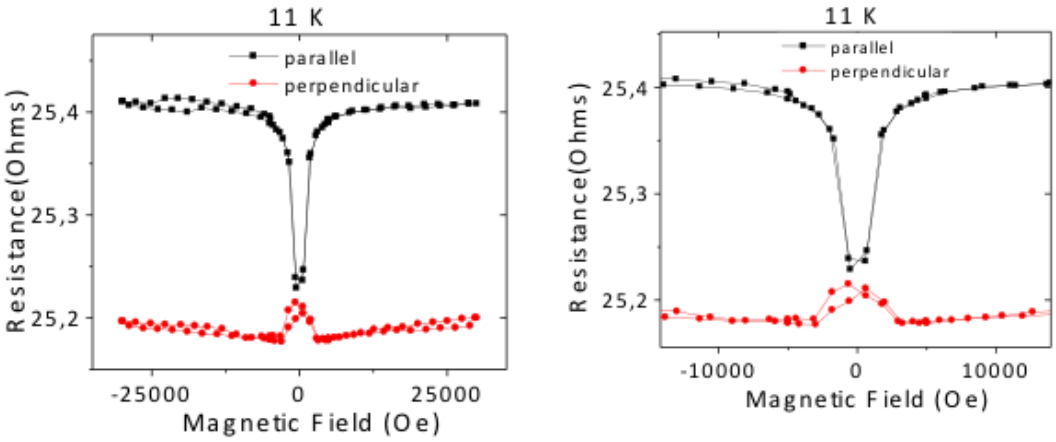

Figure 4.16. Two-wire AMR of Ni nanowire at 11K

We observe that with temperature above 9K, the field has no effect on the resis-

tance of the superconductor. Hence the change observed is only due the AMR effect in the NW. At temperatures well below 9K, we observe that the resistance of superconducting leads goes to zero, and with the application of high fields > 0.5 T leads to an increase in resistance. But at low fields, the contributing factor to the change in resistance is again due to the AMR effect. We also observe the increase in minimum resistance as we increase the temperature due to thermal effects in transition metal like Ni. Around transition temperature (7-9 K), there is a sharp increase in resistance with the application of fields. So as a field is applied, the resistance of the NW decreases due to AMR effect, whereas the the resistance of the superconducting lead increases thereby leading to an inverse magnetoresistance effect. The AMR curves in the parallel direction do not show a decrease in resistance with increase in fields. This further implies that the magnon scattering reduction only takes place at room temperature.

4.6.2 4-wire measurements

The separation between the two Nb contact pads on top of the nanowire are constant in our measurement which $\sim$1.6 μm. The change in resistance with temperature was measured at various fields as shown in Fig 4.17(b). We notice the resistance of the wire drop suddenly just below 9K. The resistance, however drops only until 1 ohm and does not become superconducting. With the application of field, the drop of the resistance occurs at lower temperatures as compared to 9K in pure Nb(4.17(a)).

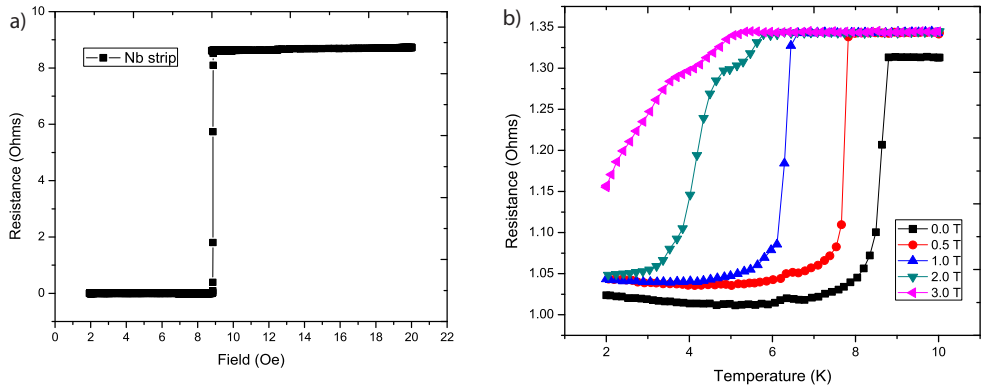

Figure 4.17. R vs T Four wire measurement of Ni nanowire

Below 9K we observe the superconducting transition of the Nb lead in 4-wire measurements. At low temperatures (T$<$ 7K) we observed the AMR behavior of the Ni at low fields and then suppression of the superconductivity at high fields. For intermediate temperatures the AMR signal is perturbed by the superconductivity. Very near superconducting transition temperature the magnetoresisitance is dominated by the response of the superconducting leads with a strong increase of resistance with applied fields. While we observed some features in the transport data that is similar to Wang et al. [120] we do not see evidence of long-range proximity effect in the Ni wires. The drop in the resistance can be accounted for by current flowing through the Nb contacts present on top of the Ni nanowire.

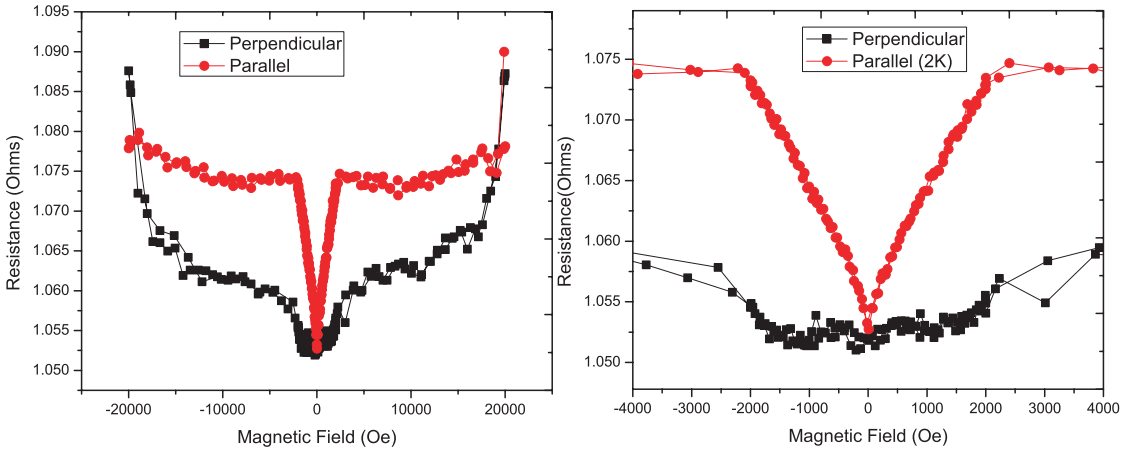

Figure 4.18. Four-wire AMR of Ni nanowire at 2K

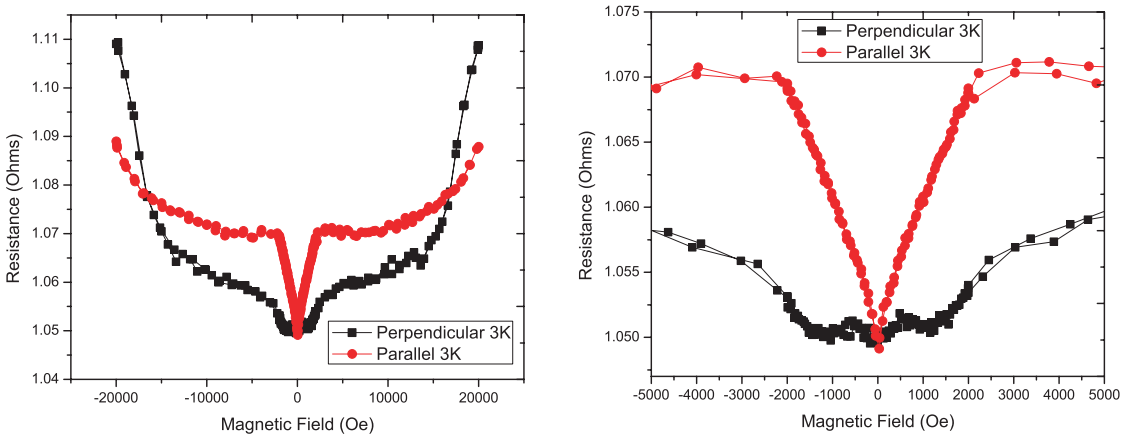

Figure 4.19. Four-wire AMR of Ni nanowire at 3K

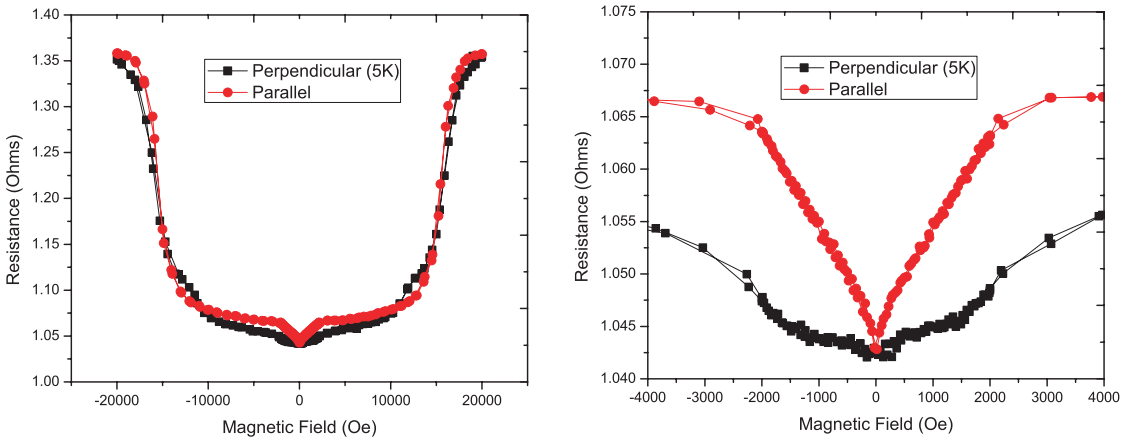

Figure 4.20. Four-wire AMR of Ni nanowire at 5K

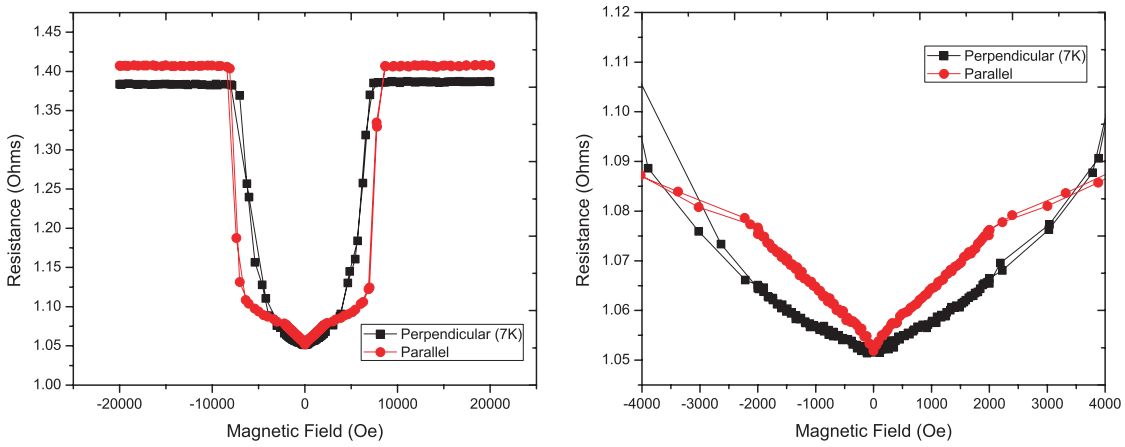

Figure 4.21. Four-wire AMR of Ni nanowire at 7K

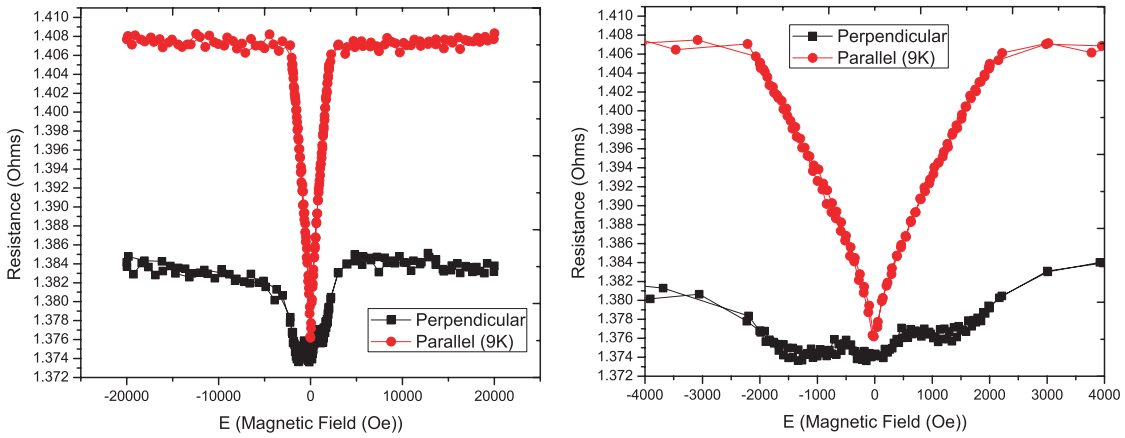

Figure 4.22. Four-wire AMR of Ni nanowire at 9K

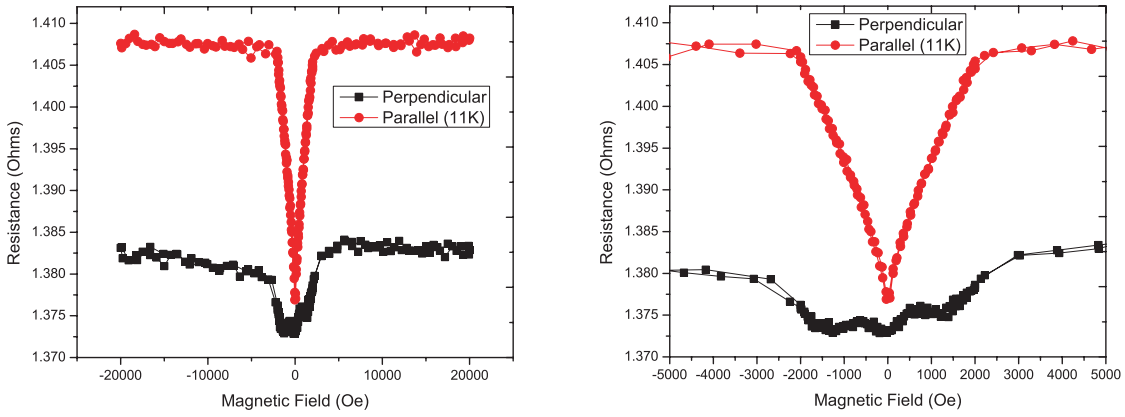

Figure 4.23. Four-wire AMR of Ni nanowire at 11K

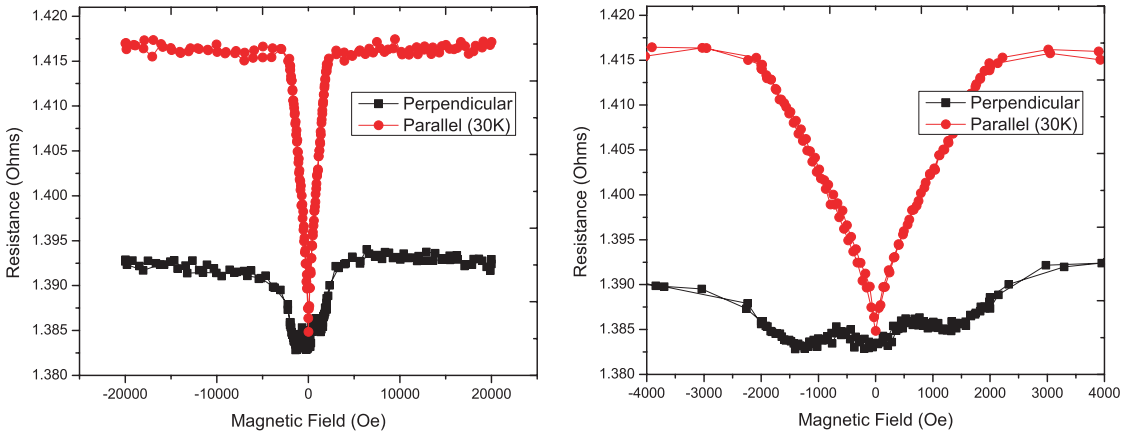

Figure 4.24. Four-wire AMR of Ni nanowire at 30K

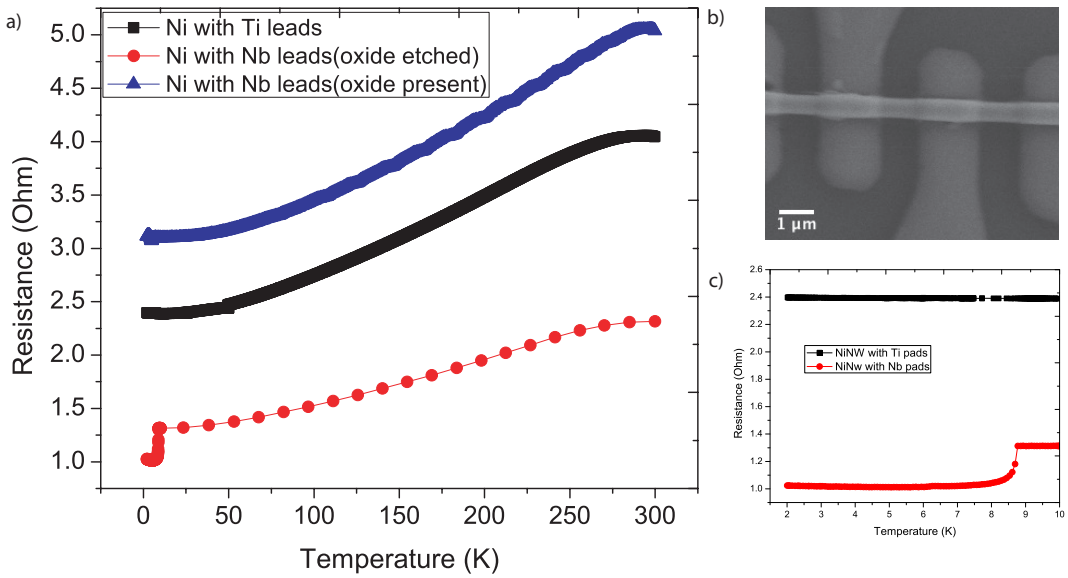

Figure 4.25. (a) R vs T Four-wire measurement with different contacts (b) SEM images of Ni nanowire with Nb contacts (c) Zoomed in R vs T Four-wire measurement with Nb and Ti contacts

If we compare the resistance (R) vs temperature (T) curves of the Ni nanowire with Nb contacts (where the oxide was etched before Nb was sputtered) to the one with Nb contacts (where the oxide was not etched) and to that of Titanium (Ti) contacts, the rate of change of resistance is similar until just below Tc of Nb (Fig 4.25(a)). The quality of interface between nanowire and Nb is very important. If we look closer in Fig 4.25(c),

we notice that resistance drops suddenly at 8.7K (which is slightly below Tc of Nb) and we observe the drop is not very sharp and rather has a tail. This indicates there is a strong interface effect and the drop in resistance is not merely due to the shunting effect of Nb contacts becoming superconducting. In fact, the shifting of Tc to 8.7K shows that the superconuctivity in Nb being suppressed and this might be due to the magnetic field of the nickel nanowire. Nb is type-II superconductor, which entails that a magnetic field can penetrate the superconductor to a certain extent and supress superconductivity.

What was surprising is that when we pass different amounts of current into the nanowire, we observe two transitions as shown in Fig 4.26(a). The transition around 9K is independent of the amount of current passed but the second transition is sensitive to it. The first transition is related to the contacst becoming superconducting but the second transition is related to the nanowire itself.

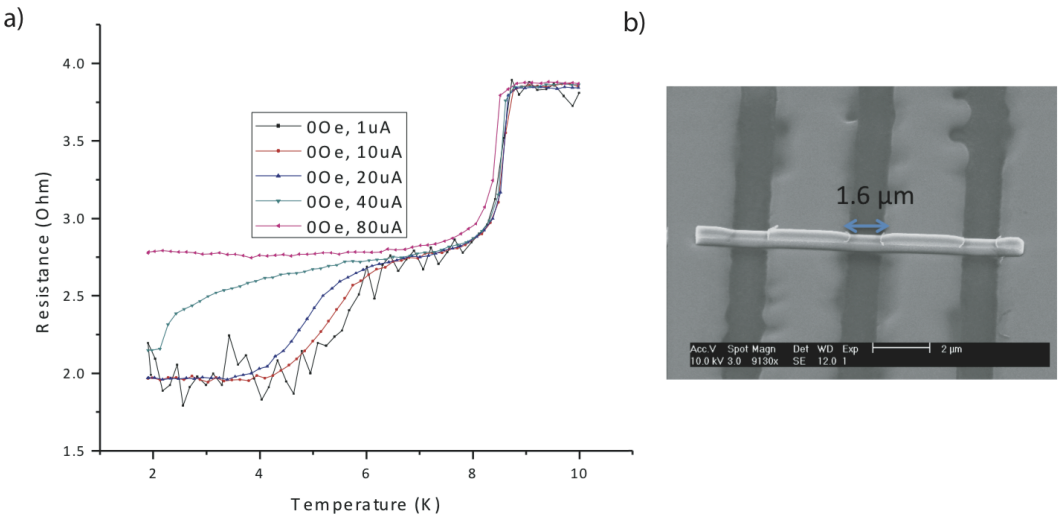

Figure 4.26. (a) R vs T Four-wire measurement with different current passed (b) SEM images of Ni nanowire with Nb contacts with separation of 1.6μm

We reduced the inner contact separation to 320 nm for similar measurements. As as shown in Fig 4.27 (b), we observe the nanowire becoming superconducting. We notice

that the two-wire measurement, the resistance only reaches a minimum resistance of $\sim$ 200 ohms which tells us that our contacts are indeed not shorted.

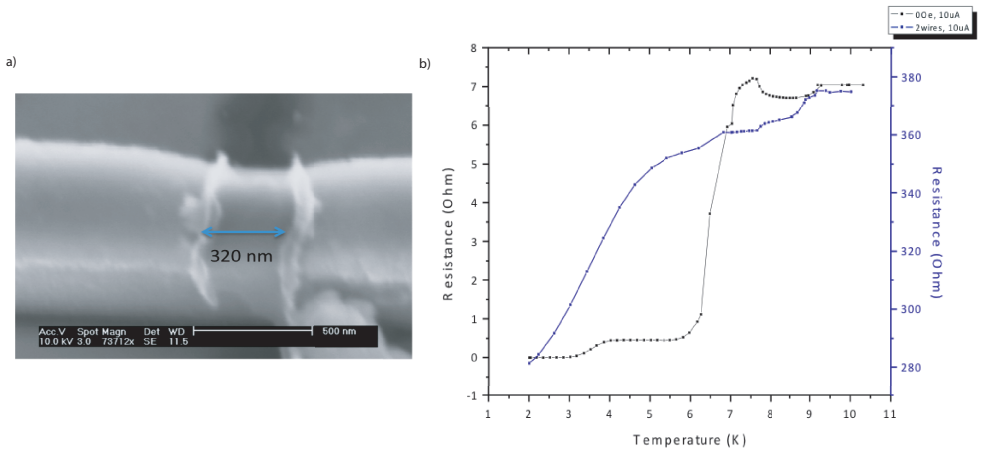

Figure 4.27. R vs T measurement with lead separation of 320 nm. (a) shows the SEM image of the separation between inner two contacts (b) R Vs T measurement which shows the nickel nanowire becomes superconducting

We observe the evolution of the AMR curves at different temperatures in Fig 4.28 and at 6K, we observe the AMR as expected, but around 3K and 2K it dissapears. What is puzzling is the the resistance is zero even at high fields such as 2T where we would expect the nanowire to be fully saturated and hence the inhomgeneity to not be present, which is required for the triplet cooper pairs to exist.

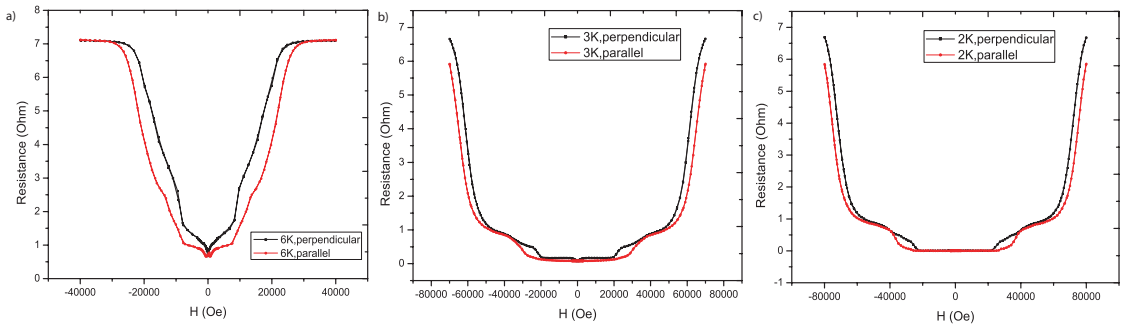

Figure 4.28. AMR measurements with lead separation of 320 nm (a) at 6K, where we still notice ferromagnetic AMR signature, (b), at 3K, the AMR signal weakens and (c) at 2K, where the AMR signal dissapears completely

And as we observe in Fig 4.29 (a) and (b), the Resistance vs Temperature curve is dependent on the amount of current and the external field applied. The superconductivity is supressed with currents and fields. So in this measurement, we observe long range proximity effects of the order of 160 nm in single crystal nickel nanowire. This is an exciting and a bold claim, which we would like to verify again by making the contacts more cleaner.

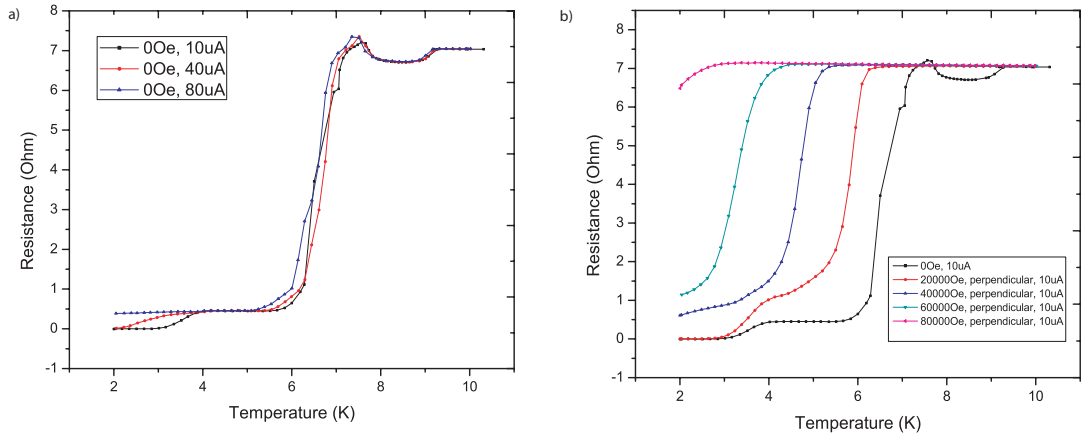

Figure 4.29. R vs T four-wire measurement with (a) different currents passed (b) at different perpendicular fields applied

Chapter 5

Two Dimension:Thin films

Thin films especially metallic thin films are ubiquitous in modern world. They exist in potato chips bags to the chips in smartphones. The earliest observation of thin films in literature can be traced back to a study in 1852 carried out by Grove[127], who noted that thin films are formed by the sputtering of cathode with high energy ions. Since then there has been a phenomenal rise in metallic thin films research due to their prolific applications in electronics, optics, aviation, space science, defence and several other industries. These investigations have led to the inventions of several devices and components such as piezo-electric devices, spintronic devices, solar cells, reflecting and anti-reflecting coatings and magnetic recording.

Metal thin film properties are sensitive not only to their structures but also to many other parameters, including the process by which they are made, deposition conditions, substrates onto which they are deposited and most crucially on their thickness. Optical, electrical and magnetic properties change with thickness and surface. Magnetic thin films have been developed where the spins of electrons are exploited for applications in spintronics ranging from sensors to storage.

5.1 Thin films in Spintronics

Electrons have two attributes, ”charge” and ”spin”. Conventional electronic devices operate on charge transfer due to electron motion. Spintronic devices depend on both, charge and spin transfer. ”Magnetism” arises from uncompensated spins in individual atoms. Magnetoresistance (MR) is a term that describes the change in resistance when an external field is applied to any material. It is due to the lorentz force experience by electrons in current flow. The inherent magnetization in a ferromagnetic material coupled with the electron flow leads to an enhanced effect known as anisotropic magnetoresistance (AMR)[128]. This effect was dependent on the angle between the electric current and magnetization. Typically, the resistance is smaller if the electric current flows in a direction perpendicular to the direction of magnetization than parallel. With the possibility of depositing thin films with accurate control, magnetic thin films such as permalloy with AMR effect of few percent, became very useful in technical applications such as sensors in the read-out head for magnetic recording.

With the innovation of giant magnetoresistance effect in ferromagnetic metal/non magnetic metal hybrid structures by Fert[129] and Grunberg[130] in 1988, a revolution began in magnetic storage industry with IBM developing spin valve structures made of magnetic and non magnetic thin films. Futher developments in this field led to the discovery of Tunnel magnetoresistance effect (TMR) by Miyazaki[131] and Moodera[132] providing opportunities for the development of memory elements in a new type of non-volatile memory known as magnetoresistive random-access memories (MRAM).

Magnetic tunnel junctions (MTJs) are thin-films structures where two ferromagnetic conducting layers are separated by a very thin barrier often a dielectric material. Due to TMR effect, MTJs experience a large difference in resistance when the layers are magnetized parallel to each other than the state when the layers are magnetized

antiparallel. These two states can be switched from one another by using an external magnetic field. These two attributes make MTJs the perfect building blocks for MRAM.

5.2 CoFeB/MgO

CoFeB/MgO multilayers are widely adopted materials for MTJs because of its giant TMR ratio with in-plane magnetization and low damping. Ohno et al. later on showed that this system can also be magnetized perpendicular to the substrate plane when incorporated into an MTJ[133]. Perpendicular magnetization leads to higher density due to reduction of size and also high-stability magnetization which is important for long term storage. This large out of plane magnetorcrystalline anisotropy and large energy barrier to switzhing allow stable magnetic states at room temperature in thin film elements less than 10 nm in diameter. These states are expected to be easily swicthed via spin transfer torque[134] which has led to intense efforts to realize Spin transfer torque MRAM (STT-MRAM).

PMA is achieved only after annealing i.e after the crystallization of CoFeB/MgO. The PMA in CoFeB/MgO is an interface effect. PMA exists only in very thin CoFeB layers, as the thickness of CoFeB increases the magnetization rotates in-plane[133]. Interface anisotropy is strong enough to overcome the tendency of CoFeB layers to be magnetized in-plane due to shape anisotropy.

Annealing often causes defects in the system and high temperature annealing is not preferred in device processing. To achieve PMA in CoFeB/MgO layers, we explore Ion irradiation as a substitute.

5.3 Ion Irradiation

Ion Irradiation is an alternative technique to tune the magnetic anisotropy of magnetic thin films and optimize annealing by reducing the required temperatures [135]. Ion

Irradiation can induce either local order or disorder depending on the enthalpy of mixing and the temperature used during the ion treatment, thereby modifying in a precise way the magneto crystalline and interface anisotropy[136–138]. The modifications are brought about by the energy loss of ions in the crystal structure. Early examples of using ion irradiation include in-plane rotation of magnetic anisotropy of CoPt multilayers[139, 140] with perpendicular magnetic anisotropy (PMA) using He+ ions, out of plane rotation in FePt films[141] due to the subsequent increase of PMA due to induction of chemical order and supression of exchange bias in FeNi/FeMn films. The local nature of the modifications due to ion irradiation is an advantage for applications such as planar magnetic nano-patterning[142–144] and the study and control of magnetic domain wall dynamics[145]. Magnetic feature sizes below 50 nm is facile without affecting the surface topography in contrast to lithographic techniques. Earlier studies have demonstrated the use of He+ ion irradiation on CoFeB/MgO thin films to control perpendicular anisotropy (PMA)[145, 146]. The focus is on CoFeB[133] thin films since it is a magnetic system generating immense interest due to its perpendicular anisotropy and low damping parameters which is appealing for spintronic applications such as MRAM[147, 148]. The degree of crystallization and sharp interfaces affect the performance of CoFeB/MgO films. These films comprise the free layer of a MTJ. In general these films need to be annealed at high temperatures $\sim 380^{\circ}$C[149] to bring about the crystallization which leads to PMA[133]. Ion Irradiation induces similar effect while keeping the annealing temperatures low. In this study, we optimize the temperature at which the irradiation is done as well as the irradiation dose (ID) to obtain high PMA. He+ irradiation has shown to increase domain wall velocity and at the same time, to reduce the annealing temperature used to induce PMA in non-irradiated films.

5.4 Experiments

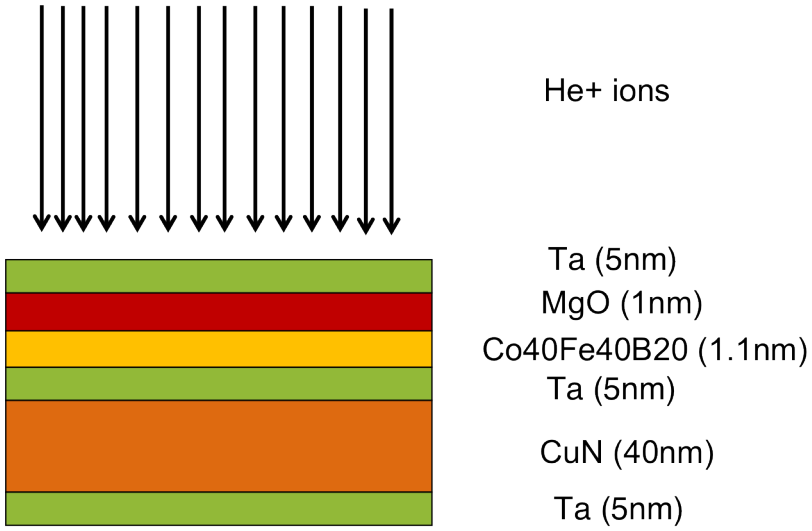

Figure 5.1. Schematic illustration of sample structure

The samples investigated are the free layer of a bigger MTJ stack: Ta(5nm)\ CuN (40nm)\ Ta(5nm)\ Co40Fe40B20 (1.1nm)\ MgO (1nm)\ Ta(5nm) which were prepared by magnetron sputtering by Singulus. The schematic diagram of the sample structure is illustrated in Fig 5.1. The as-grown films are amorphous and have inplane anisotropy. These films when annealed at 380°C exhibit PMA. These films are then irradiated with He+ ions with constant energy of 15keV using a current density of $10\mu A/cm^2$ with varying irradiation doses (ID) ranging from 8×10^{14} He+/m^2 to 25×10^{14} He+/ m^2. The irradiation occurs at temperatures of 150°C, 200°C and 250°C. The magnetization characterization were done with polar magneto-optical Kerr effect (PMOKE).

5.5 Results & Discussion

Characterization of the films were carried on using polar moke and the resulting loops were analyzed. The as-grown films require annealing at temperatures greater than 300°C to induce PMA. Fig 5.2 shows a gradual increase of PMA as the annealing

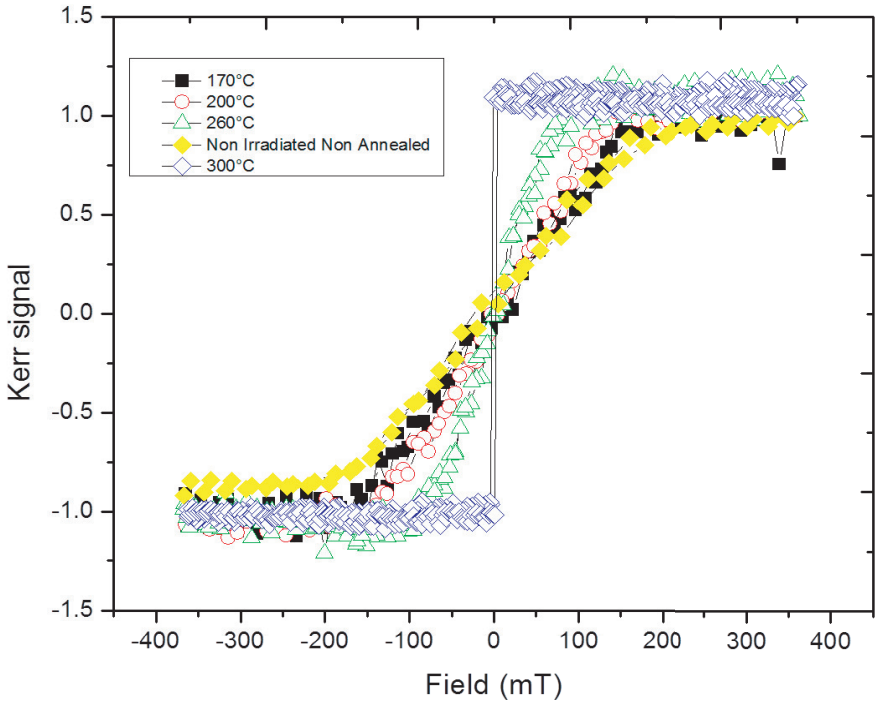

Figure 5.2. A gradual increase in PMA with increase in temperature achieving full PMA around 300°C

temperatures is increased. However, high annealing temperatures are not suitable for most device processing. Our overall goal is to reduce the annealing temperatures. Using Ion irradiation at lower temperature also induces PMA. As demonstrated in Fig 5.3, we observe a gradual increase in PMA as ID is increased. The PMA response also increases when irradiation is done at higher temperatures. When irradiation occurs at 150°C, there anisotropy rotates more out of plane with increase in ID, however never becomes fully perpendicular. At 200°C, with increase in ID, the anisotropy becomes more out of plane. It becomes fully perpendicular at the highest dose.

Full PMA is achieved with most ID at temperature of 250°C. Therefore, the optimum temperature for irradiation to take place is 250°C for full PMA in the CoFeB/MgO

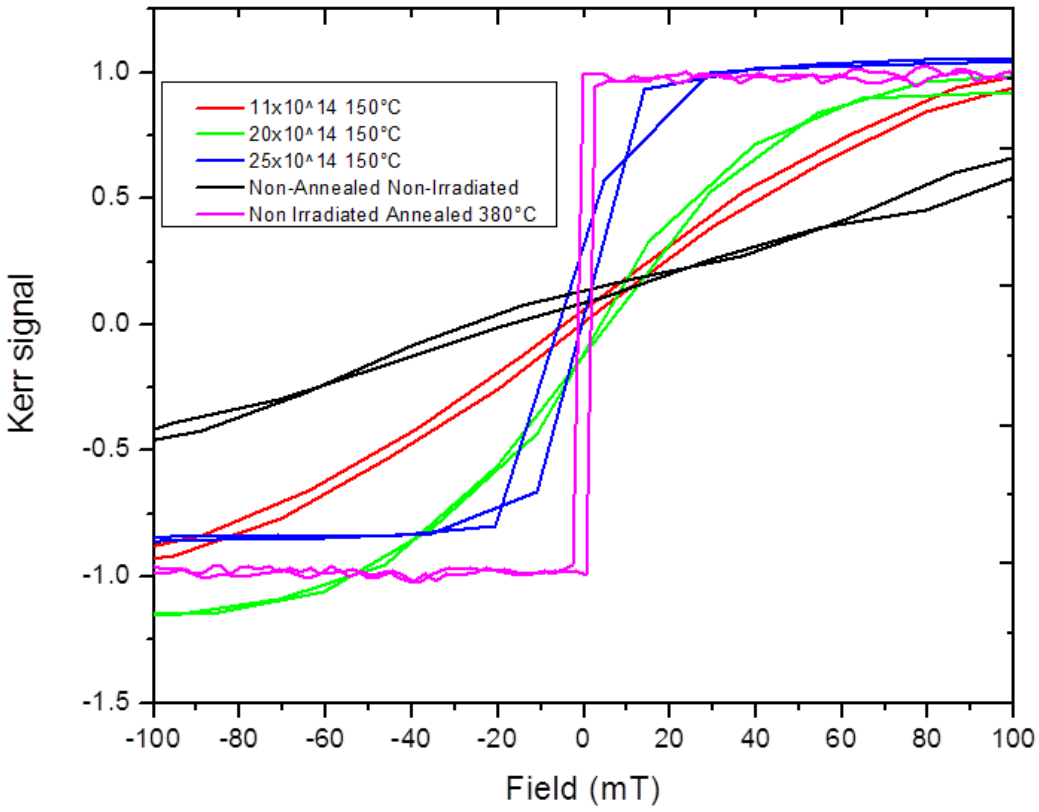

Figure 5.3. Magneto-optical hysteresis loops of films irradiated with varying ID at 150°C

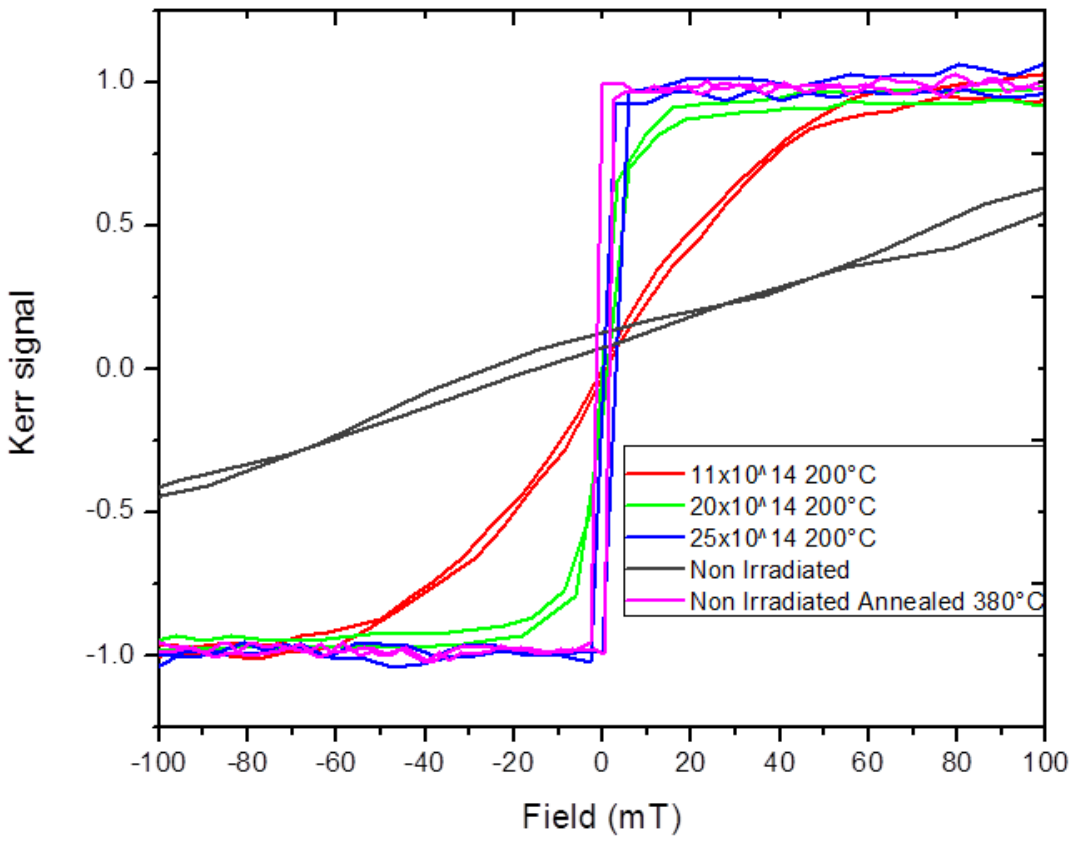

Figure 5.4. Magneto-optical hysteresis loops of films irradiated with varying ID at 200°C

free layer of MTJ. At this temperature, irradiation can facilitate crystallization process which induces PMA in the system. When we look closely at the magneto-optical hystersis loops in Fig 5.4 (a), we notice an increase in the squareness and thus PMA with ID. The quantitative evaluation of magnetic anisotropy has been carried out by measuring magneto-optical kerr loops as a function of an in-plane field (along hard axis) and subsequent fitting by minimisation of the anisotropy energy density given by the following equation.

$$E = K_e sin(\theta)^2 + K_e^2 sin(\theta)^4 - HM_s cos(\theta - \phi) \tag{5.1}$$

where H = magnetic field, θ =angle between H and M_s, ϕ = angle between H and the easy

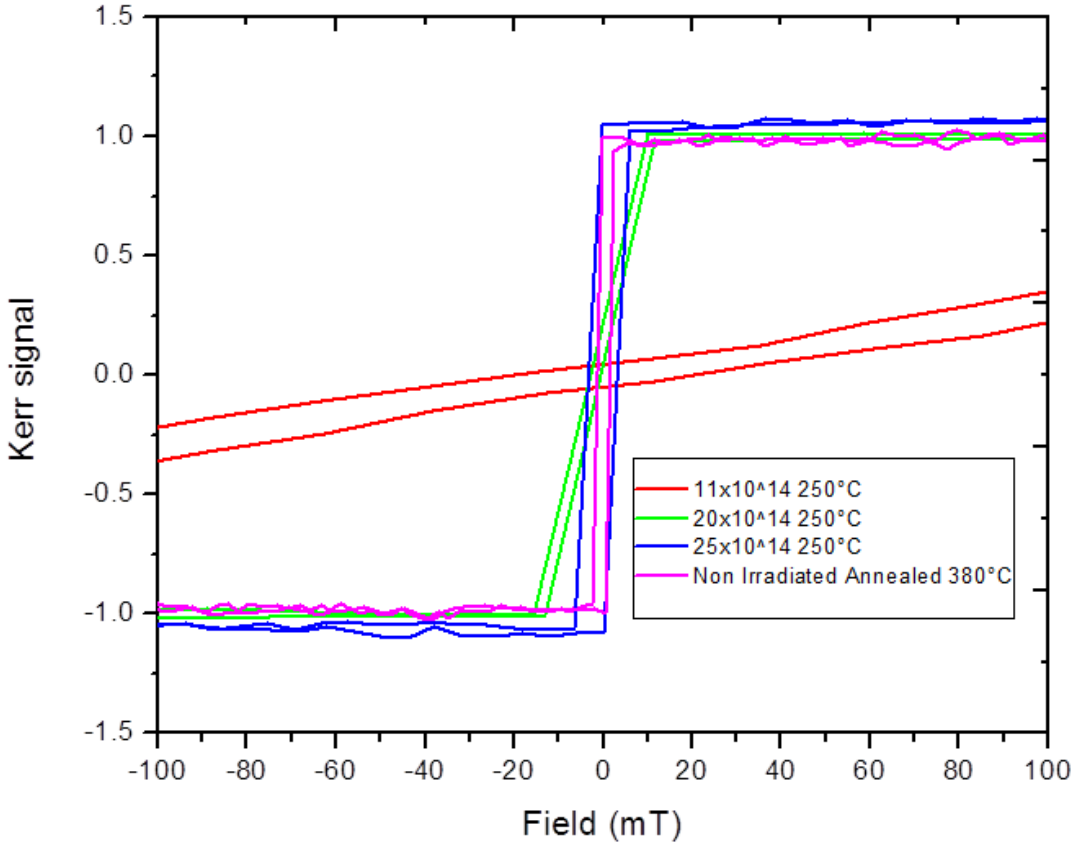

Figure 5.5. Magneto-optical hysteresis loops of films irradiated with varying ID at 250°C

axis. We observe a gradual increase in anisotropy coefficient with increase in fluence as shown in Fig 5.4 (b).

Utilizing differential Kerr microscopy we study the domain wall dynamics in thin films irradiated at 250°C. Fig 5.5 (a) demonstrates the marked increase in domain wall velocity with increase in dosage.

In this study we demonstrate the use of He+ ion irradiation on CoFeB/MgO free layer to control perpendicular anisotropy (PMA). We demonstrate a visible increase in PMA and domain wall velocity with increasing He+ irradiation dose and while keeping the annealing temperature below 380°C. We found that the optimum temperature at which the free laer should be iradiated is at 250°C for achieving full PMA. The reported He+

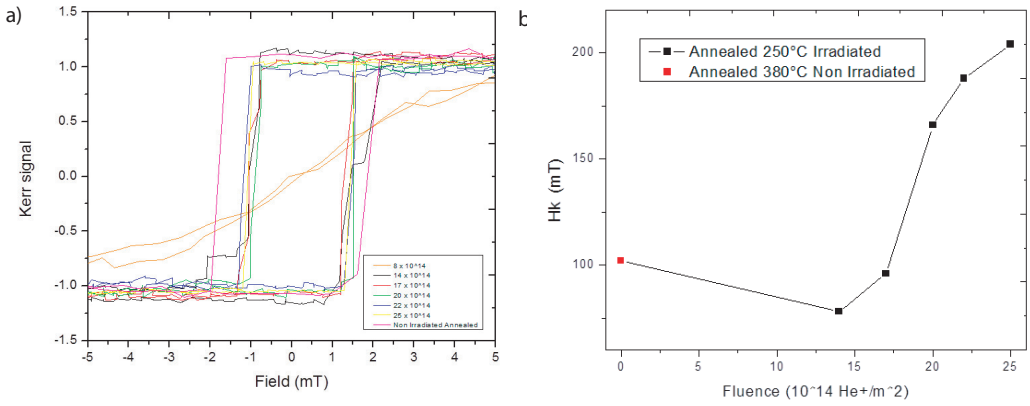

Figure 5.6. Anisotropy of films irradiated at 250°C (a) Magneto-optical hysteresis loops of films irradiated with varying fluence at 250°C (b) anisotropy of films with varying fluence

irradiation induced improvement of the magnetic properties combined with a reduction of the annealing temperature of 130°C shows the great potential of He+ irradiation as a powerful tool for the development of spintronics devices.

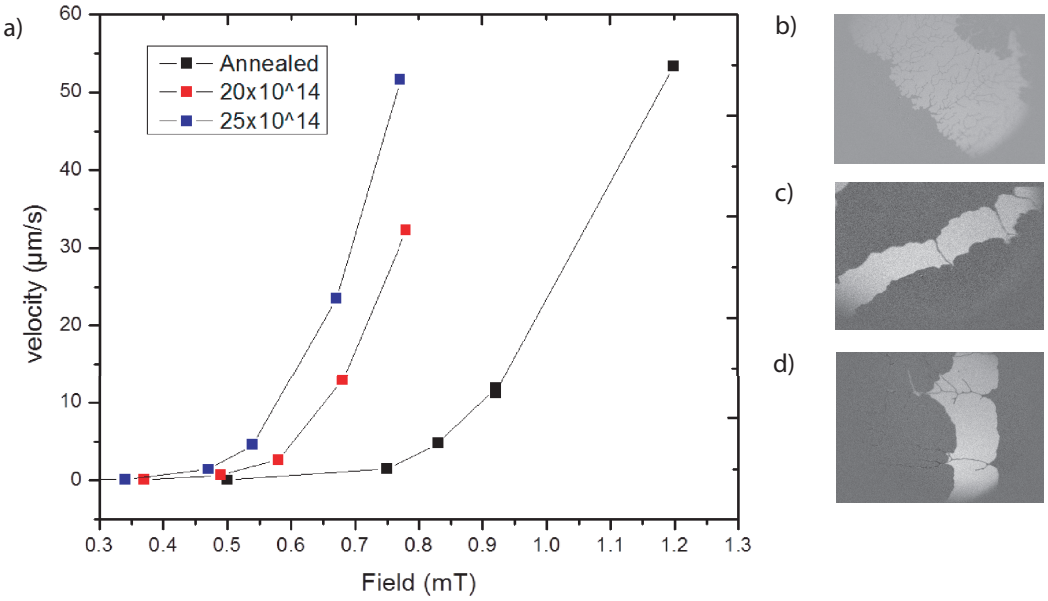

Figure 5.7. (a) Domain wall velocity evaluated using differential Kerr microscopy. Kerr microscop image of (a) as grown non annealed film (b) film irradiated with a dose of 20×10^{14} He+/ m^2(c) film irradiated with a dose of 25×10^{14} He+/ m^2

Chapter 6

Conclusion

The role of anisotropy manifests in nanomaterials. Anistropic nanocrystals and nanowires were synthesized by exploiting the anistropic energies of crystal facets of metallic crystal structures and shape energetics. These anisotropies in shape also lead to anisotropic properties such as strain or magnetic properties. This leads to interesting phenomena at nanoscale.

We synthesized a range of metallic nanomaterials from nanocrystals to nanowires to thin films. Anistropy in some form or the other, provide us with a parameter to play with the properties of such materials. We probed the strain in nanocrystals which is dependent on the anistropy in shape of the crystals. We probed the magnetic properties in magnetic nanowires and how they are dependent either on shape anisotropy or the magnetocrystalline anisotropy. We observed long range proximity effect of the order of 160 nm in our single crystal nickel nanowire. We observe how the magnetic properties of thin film can be tailored by altering the interface anisotropy between multilayers.

Bibliography

[1] Quan Li. *Anisotropic Nanomaterials*. Springer, 2015.

[2] Sohini Manna, Jong Woo Kim, Yukiko Takahashi, Oleg G Shpyrko, and Eric E Fullerton. Synthesis of single-crystalline anisotropic gold nano-crystals via chemical vapor deposition. *Journal of Applied Physics*, 119(17):174301, 2016.

[3] JW Kim, S Manna, SH Dietze, A Ulvestad, R Harder, E Fohtung, EE Fullerton, and OG Shpyrko. Curvature-induced and thermal strain in polyhedral gold nanocrystals. *Applied Physics Letters*, 105(17):173108, 2014.

[4] Gerd Binnig, Calvin F Quate, and Ch Gerber. Atomic force microscope. *Physical review letters*, 56(9):930, 1986.

[5] JJ Saenz, N Garcia, P Grütter, E Meyer, H Heinzelmann, R Wiesendanger, L Rosenthaler, HR Hidber, and H-J Güntherodt. Observation of magnetic forces by the atomic force microscope. *Journal of applied physics*, 62(10):4293–4295, 1987.

[6] Jianwei Miao, Richard L Sandberg, and Changyong Song. Coherent x-ray diffraction imaging. *Ieee Journal of Selected Topics in Quantum Electronics*, 18(1): 399–410, 2012.

[7] Ian Robinson and Ross Harder. Coherent x-ray diffraction imaging of strain at the nanoscale. *Nature materials*, 8(4):291–298, 2009.

[8] R Chang, S Li, MV Lubarda, B Livshitz, and V Lomakin. Fastmag: Fast micromagnetic simulator for complex magnetic structures. *Journal of Applied Physics*, 109(7):07D358, 2011.

[9] Deping Huang, Xiangtao Bai, and Liqiang Zheng. Ultrafast preparation of three-dimensional dendritic gold nanostructures in aqueous solution and their applications in catalysis and sers. *The Journal of Physical Chemistry C*, 115(30): 14641–14647, 2011.

[10] Didier Astruc, Feng Lu, and Jaime Ruiz Aranzaes. Nanoparticles as recyclable catalysts: The frontier between homogeneous and heterogeneous catalysis. *Angewandte Chemie International Edition*, 44(48):7852–7872, 2005. ISSN 1521-3773. doi: 10.1002/anie.200500766. URL http://dx.doi.org/10.1002/anie.200500766.

[11] Gabor A Somorjai, Feng Tao, and Jeong Young Park. The nanoscience revolution: merging of colloid science, catalysis and nanoelectronics. *Topics in Catalysis*, 47 (1-2):1–14, 2008.

[12] Marie-Christine Daniel and Didier Astruc. Gold nanoparticles: assembly, supramolecular chemistry, quantum-size-related properties, and applications toward biology, catalysis, and nanotechnology. *Chemical reviews*, 104(1):293–346, 2004.

[13] Dimitra G Georganopoulou, Lei Chang, Jwa-Min Nam, C Shad Thaxton, Elliott J Mufson, William L Klein, and Chad A Mirkin. Nanoparticle-based detection in cerebral spinal fluid of a soluble pathogenic biomarker for alzheimer's disease. *Proceedings of the National Academy of Sciences of the United States of America*, 102(7):2273–2276, 2005.

[14] C. Shad Thaxton, Dimitra G. Georganopoulou, and Chad A. Mirkin. Gold nanoparticle probes for the detection of nucleic acid targets. *Clinica Chimica Acta*, 363(1–2):120 – 126, 2006. ISSN 0009-8981. doi: http://dx.doi.org/10.1016/j.cccn.2005.05.042. URL http://www.sciencedirect.com/science/article/pii/S0009898105004304. From Real-Time {PCR} to Nanotechnology: Rapid and/or High-Throughput Diagnostic Methods for Nucleic Acids.

[15] Haley D Hill and Chad A Mirkin. The bio-barcode assay for the detection of protein and nucleic acid targets using dtt-induced ligand exchange. *NATURE PROTOCOLS-ELECTRONIC EDITION-*, 1(1):324, 2006.

[16] Dwight S Seferos, David A Giljohann, Haley D Hill, Andrew E Prigodich, and Chad A Mirkin. Nano-flares: probes for transfection and mrna detection in living cells. *Journal of the American Chemical Society*, 129(50):15477–15479, 2007.

[17] Haley D Hill, Rafael A Vega, and Chad A Mirkin. Nonenzymatic detection of bacterial genomic dna using the bio bar code assay. *Analytical chemistry*, 79(23): 9218–9223, 2007.

[18] Matthew J Banholzer, Nadine Harris, Jill E Millstone, George C Schatz, and Chad A Mirkin. Abnormally large plasmonic shifts in silica-protected gold triangular nanoprisms. *The Journal of Physical Chemistry C*, 114(16):7521–7526,

2010.

[19] Can Xue, Jill E Millstone, Shuyou Li, and Chad A Mirkin. Plasmon-driven synthesis of triangular core–shell nanoprisms from gold seeds. *Angewandte Chemie*, 119(44):8588–8591, 2007.

[20] Xiaohua Huang and Mostafa A El-Sayed. Gold nanoparticles: optical properties and implementations in cancer diagnosis and photothermal therapy. *Journal of Advanced Research*, 1(1):13–28, 2010.

[21] G Schmid and U Simon. Gold nanoparticles: assembly and electrical properties in 1–3 dimensions. *Chemical communications*, (6):697–710, 2005.

[22] Rongchao Jin, Y Charles Cao, Encai Hao, Gabriella S Métraux, George C Schatz, and Chad A Mirkin. Controlling anisotropic nanoparticle growth through plasmon excitation. *Nature*, 425(6957):487–490, 2003.

[23] S Shiv Shankar, Akhilesh Rai, Balaprasad Ankamwar, Amit Singh, Absar Ahmad, and Murali Sastry. Biological synthesis of triangular gold nanoprisms. *Nature materials*, 3(7):482–488, 2004.

[24] Jianhua Sun, Mingyun Guan, Tongming Shang, Cuiling Gao, Zheng Xu, and Jianmin Zhu. Selective synthesis of gold cuboid and decahedral nanoparticles regulated and controlled by cu2+ ions. *Crystal Growth and Design*, 8(3):906–910, 2008.

[25] Yi-Hsin Chien, Chih-Chia Huang, Shu-Wen Wang, and Chen-Sheng Yeh. Synthesis of nanoparticles: sunlight formation of gold nanodecahedra for ultra-sensitive lead-ion detection. *Green Chemistry*, 13(5):1162–1166, 2011.

[26] Jorge Pérez-Juste, Isabel Pastoriza-Santos, Luis M Liz-Marzán, and Paul Mulvaney. Gold nanorods: synthesis, characterization and applications. *Coordination Chemistry Reviews*, 249(17):1870–1901, 2005.

[27] Christopher J Johnson, Erik Dujardin, Sean A Davis, Catherine J Murphy, and Stephen Mann. Growth and form of gold nanorods prepared by seed-mediated, surfactant-directed synthesis. *Journal of Materials Chemistry*, 12(6):1765–1770, 2002.

[28] ZL Wang, MB Mohamed, S Link, and MA El-Sayed. Crystallographic facets and shapes of gold nanorods of different aspect ratios. *Surface Science*, 440(1): L809–L814, 1999.

[29] Xiguang Han, Mingshang Jin, Shuifen Xie, Qin Kuang, Zhiyuan Jiang, Yaqi Jiang, Zhaoxiong Xie, and Lansun Zheng. Synthesis of tin dioxide octahedral nanoparticles with exposed high-energy $\{221\}$ facets and enhanced gas-sensing properties. *Angewandte Chemie*, 121(48):9344–9347, 2009.

[30] Wenguang Yu, Tonglai Zhang, Jianguo Zhang, Xiaojing Qiao, Li Yang, and Yanhong Liu. The synthesis of octahedral nanoparticles of magnetite. *Materials Letters*, 60(24):2998–3001, 2006.

[31] DK Saha, K Koga, and H Takeo. Stable icosahedral nanoparticles in an as-grown au–fe alloy. *The European Physical Journal D-Atomic, Molecular, Optical and Plasma Physics*, 9(1):539–542, 1999.

[32] Qingbo Zhang, Jianping Xie, Jinhua Yang, and Jim Yang Lee. Monodisperse icosahedral ag, au, and pd nanoparticles: size control strategy and superlattice formation. *Acs Nano*, 3(1):139–148, 2008.

[33] Kihyun Kwon, Kang Yeol Lee, Young Wook Lee, Minjung Kim, Jinhwa Heo, Sang Jung Ahn, and Sang Woo Han. Controlled synthesis of icosahedral gold nanoparticles and their surface-enhanced raman scattering property. *The Journal of Physical Chemistry C*, 111(3):1161–1165, 2007.

[34] DK Kim, Y Zhang, W Voit, KV Rao, and Mamoun Muhammed. Synthesis and characterization of surfactant-coated superparamagnetic monodispersed iron oxide nanoparticles. *Journal of Magnetism and Magnetic Materials*, 225(1):30–36, 2001.

[35] Nikhil R Jana, Latha Gearheart, and Catherine J Murphy. Seed-mediated growth approach for shape-controlled synthesis of spheroidal and rod-like gold nanoparticles using a surfactant template. *Advanced Materials*, 13(18):1389, 2001.

[36] Hiroki Hiramatsu and Frank E Osterloh. A simple large-scale synthesis of nearly monodisperse gold and silver nanoparticles with adjustable sizes and with exchangeable surfactants. *Chemistry of Materials*, 16(13):2509–2511, 2004.

[37] Irshad Hussain, Susan Graham, Zhenxin Wang, Bien Tan, David C Sherrington, Steven P Rannard, Andrew I Cooper, and Mathias Brust. Size-controlled synthesis of near-monodisperse gold nanoparticles in the 1-4 nm range using polymeric stabilizers. *Journal of the American Chemical Society*, 127(47):16398–16399, 2005.

[38] Toshiharu Teranishi, Iwao Kiyokawa, and Mikio Miyake. Synthesis of monodis-

perse gold nanoparticles using linear polymers as protective agents. *Advanced Materials*, 10(8):596–599, 1998.

[39] Janne Raula, Jun Shan, Markus Nuopponen, Antti Niskanen, Hua Jiang, Esko I Kauppinen, and Heikki Tenhu. Synthesis of gold nanoparticles grafted with a thermoresponsive polymer by surface-induced reversible-addition-fragmentation chain-transfer polymerization. *Langmuir*, 19(8):3499–3504, 2003.

[40] Paresh Chandra Ray, Hongtao Yu, and Peter P Fu. Toxicity and environmental risks of nanomaterials: challenges and future needs. *Journal of Environmental Science and Health Part C*, 27(1):1–35, 2009.

[41] Ellen E Connor, Judith Mwamuka, Anand Gole, Catherine J Murphy, and Michael D Wyatt. Gold nanoparticles are taken up by human cells but do not cause acute cytotoxicity. *Small*, 1(3):325–327, 2005.

[42] Elodie Boisselier and Didier Astruc. Gold nanoparticles in nanomedicine: preparations, imaging, diagnostics, therapies and toxicity. *Chemical Society Reviews*, 38(6):1759–1782, 2009.

[43] Raja G Rayavarapu, Wilma Petersen, Liesbeth Hartsuiker, Patrick Chin, Hans Janssen, Fijs WB Van Leeuwen, Cees Otto, Srirang Manohar, and Ton G Van Leeuwen. In vitro toxicity studies of polymer-coated gold nanorods. *Nanotechnology*, 21(14):145101, 2010.

[44] Wan-Seob Cho, Minjung Cho, Jinyoung Jeong, Mina Choi, Hea-Young Cho, Beom Seok Han, Sheen Hee Kim, Hyoung Ook Kim, Yong Taik Lim, Bong Hyun Chung, et al. Acute toxicity and pharmacokinetics of 13 nm-sized peg-coated gold nanoparticles. *Toxicology and applied pharmacology*, 236(1):16–24, 2009.

[45] Catherine M Goodman, Catherine D McCusker, Tuna Yilmaz, and Vincent M Rotello. Toxicity of gold nanoparticles functionalized with cationic and anionic side chains. *Bioconjugate chemistry*, 15(4):897–900, 2004.

[46] Babak Nikoobakht and Mostafa A El-Sayed. Preparation and growth mechanism of gold nanorods (nrs) using seed-mediated growth method. *Chemistry of Materials*, 15(10):1957–1962, 2003.

[47] Tapan K Sau, Anjali Pal, NR Jana, ZL Wang, and Tarasankar Pal. Size controlled synthesis of gold nanoparticles using photochemically prepared seed particles. *Journal of Nanoparticle Research*, 3(4):257–261, 2001.

[48] Zhen Ma and Sheng Dai. Development of novel supported gold catalysts: A materials perspective. *Nano Research*, 4(1):3–32, 2011.

[49] Xiaoyan Liu, Chung-Yuan Mou, Szetsen Lee, Yanan Li, Jeremiah Secrest, and Ben W-L Jang. Room temperature o 2 plasma treatment of sio 2 supported au catalysts for selective hydrogenation of acetylene in the presence of large excess of ethylene. *Journal of Catalysis*, 285(1):152–159, 2012.

[50] Yangying Chen, Jieshan Qiu, Xinkui Wang, and Jinghai Xiu. Preparation and application of highly dispersed gold nanoparticles supported on silica for catalytic hydrogenation of aromatic nitro compounds. *Journal of Catalysis*, 242(1):227–230, 2006.

[51] Masatake Haruta, Tetsuhiko Kobayashi, Hiroshi Sano, and Nobumasa Yamada. Novel gold catalysts for the oxidation of carbon monoxide at a temperature far below 0. deg. c. *Chemistry Letters*, (2):405–408, 1987.

[52] Masatake Haruta, N Yamada, T Kobayashi, and S Iijima. Gold catalysts prepared by coprecipitation for low-temperature oxidation of hydrogen and of carbon monoxide. *Journal of catalysis*, 115(2):301–309, 1989.

[53] Masatake Haruta, Susumu Tsubota, Tetsuhiko Kobayashi, Hiroyuki Kageyama, Michel J Genet, and B Delmon. Low-temperature oxidation of co over gold supported on tio 2, α-fe 2 o 3, and co 3 o 4. *Journal of Catalysis*, 144(1):175–192, 1993.

[54] Keith T Chan, Jimmy J Kan, Christopher Doran, Lu Ouyang, David J Smith, and Eric E Fullerton. Controlled growth behavior of chemical vapor deposited ni nanostructures. *Philosophical Magazine*, 92(17):2173–2186, 2012.

[55] Keith T Chan, Jimmy J Kan, Christopher Doran, Lu Ouyang, David J Smith, and Eric E Fullerton. Oriented growth of single-crystal ni nanowires onto amorphous sio2. *Nano letters*, 10(12):5070–5075, 2010.

[56] Jixiang Fang, Xiaoni Ma, Hanhui Cai, Xiaoping Song, and Bingjun Ding. Nanoparticle-aggregated 3d monocrystalline gold dendritic nanostructures. *Nanotechnology*, 17(23):5841, 2006.

[57] Martin Zinke-Allmang, Leonard C Feldman, and Marcia H Grabow. Clustering on surfaces. *Surface Science Reports*, 16(8):377–463, 1992.

[58] JG Allpress and JV Sanders. The structure and orientation of crystals in deposits

of metals on mica. *Surface Science*, 7(1):1–25, 1967.

[59] BK Min, WT Wallace, AK Santra, and DW Goodman. Role of defects in the nucleation and growth of au nanoclusters on sio2 thin films. *The Journal of Physical Chemistry B*, 108(42):16339–16343, 2004.

[60] X Lai, TP St Clair, M Valden, and DW Goodman. Scanning tunneling microscopy studies of metal clusters supported on tio 2 (110): morphology and electronic structure. *Progress in Surface Science*, 59(1):25–52, 1998.

[61] Ahmad Umar, B Karunagaran, SH Kim, E-K Suh, and YB Hahn. Growth mechanism and optical properties of aligned hexagonal zno nanoprisms synthesized by noncatalytic thermal evaporation. *Inorganic chemistry*, 47(10):4088–4094, 2008.

[62] A Howie and LD Marks. Elastic strains and the energy balance for multiply twinned particles. *Philosophical Magazine A*, 49(1):95–109, 1984.

[63] Jill E Millstone, Sarah J Hurst, Gabriella S Métraux, Joshua I Cutler, and Chad A Mirkin. Colloidal gold and silver triangular nanoprisms. *Small*, 5(6):646–664, 2009.

[64] E Bauer and Jan H van der Merwe. Structure and growth of crystalline superlattices: From monolayer to superlattice. *Physical review b*, 33(6):3657, 1986.

[65] CEJ Mitchell, A Howard, M Carney, and RG Egdell. Direct observation of behaviour of au nanoclusters on tio 2 (110) at elevated temperatures. *Surface science*, 490(1):196–210, 2001.

[66] Fabien Silly and Martin R Castell. Bimodal growth of au on srtio 3 (001). *Physical review letters*, 96(8):086104, 2006.

[67] LD Marks. Surface structure and energetics of multiply twinned particles. *Philosophical Magazine A*, 49(1):81–93, 1984.

[68] IA Vartanyants and IK Robinson. Partial coherence effects on the imaging of small crystals using coherent x-ray diffraction. *Journal of Physics: Condensed Matter*, 13(47):10593, 2001.

[69] Moyu Watari, Rachel A McKendry, Manuel Vögtli, Gabriel Aeppli, Yeong-Ah Soh, Xiaowen Shi, Gang Xiong, Xiaojing Huang, Ross Harder, and Ian K Robinson. Differential stress induced by thiol adsorption on facetted nanocrystals. *Nature materials*, 10(11):862–866, 2011.

[70] Robert L White, Richard MH Newt, and R Fabian W Pease. Patterned media: a viable route to 50 gbit/in 2 and up for magnetic recording? *Magnetics, IEEE Transactions on*, 33(1):990–995, 1997.

[71] Claude Chappert, Albert Fert, and Frédéric Nguyen Van Dau. The emergence of spin electronics in data storage. *Nature materials*, 6(11):813–823, 2007.

[72] BD Terris and T Thomson. Nanofabricated and self-assembled magnetic structures as data storage media. *Journal of physics D: Applied physics*, 38(12):R199, 2005.

[73] Anitha Ethirajan, Ulf Wiedwald, H-G Boyen, Birgit Kern, Luyang Han, Andreas Klimmer, Frank Weigl, Gerd Kaestle, Paul Ziemann, Kai Fauth, et al. A micellar approach to magnetic ultrahigh-density data-storage media: Extending the limits of current colloidal methods. *Advanced Materials*, 19(3):406–410, 2007.

[74] RL Comstock. Review modern magnetic materials in data storage. *Journal of Materials Science: Materials in Electronics*, 13(9):509–523, 2002.

[75] Aric Kumaran Menon and BK Gupta. Nanotechnology: a data storage perspective. *Nanostructured Materials*, 11(8):965–986, 1999.

[76] KJ Kirk. Nanomagnets for sensors and data storage. *Contemporary Physics*, 41 (2):61–78, 2000.

[77] Matthew Joseph Carey, Eric Edward Fullerton, Bruce Alvin Gurney, Hal Jervis Rosen, and Manfred Ernst Schabes. Magnetic recording media with antiferromagnetically coupled ferromagnetic films as the recording layer, August 28 2001. US Patent 6,280,813.

[78] Stellan Bohlens, Benjamin Krüger, André Drews, Markus Bolte, Guido Meier, and Daniela Pfannkuche. Current controlled random-access memory based on magnetic vortex handedness. *Applied Physics Letters*, 93(14):142508, 2008.

[79] Michal Urbánek, Vojtěch Uhlíř, Charles-Henri Lambert, Jimmy J Kan, Nasim Eibagi, Marek Vaňatka, Lukáš Flajšman, Radek Kalousek, Mi-Young Im, Peter Fischer, et al. Dynamics and efficiency of magnetic vortex circulation reversal. *Physical Review B*, 91(9):094415, 2015.

[80] Keisuke Yamada, Shinya Kasai, Yoshinobu Nakatani, Kensuke Kobayashi, Hiroshi Kohno, André Thiaville, and Teruo Ono. Electrical switching of the vortex core in a magnetic disk. *Nature materials*, 6(4):270–273, 2007.

[81] RP Cowburn. Property variation with shape in magnetic nanoelements. *Journal of Physics D: Applied Physics*, 33(1):R1, 2000.

[82] Russell P Cowburn and Mark E Welland. Phase transitions in planar magnetic nanostructures. *Applied physics letters*, 72(16):2041–2043, 1998.

[83] RP Cowburn, DK Koltsov, AO Adeyeye, ME Welland, and DM Tricker. Single-domain circular nanomagnets. *Physical Review Letters*, 83(5):1042, 1999.

[84] Thomas P Beebe Jr, D Wayne Goodman, Bruce D Kay, and John T Yates Jr. Kinetics of the activated dissociative adsorption of methane on the low index planes of nickel single crystal surfaces. *The Journal of chemical physics*, 87(4): 2305–2315, 1987.

[85] Koichiro Asazawa, Tomokazu Sakamoto, Susumu Yamaguchi, Koji Yamada, Hirotoshi Fujikawa, Hirohisa Tanaka, and Keisuke Oguro. Study of anode catalysts and fuel concentration on direct hydrazine alkaline anion-exchange membrane fuel cells. *Journal of The Electrochemical Society*, 156(4):B509–B512, 2009.

[86] SMA Shibli, KS Beenakumari, and ND Suma. Nano nickel oxide/nickel incorporated nickel composite coating for sensing and estimation of acetylcholine. *Biosensors and bioelectronics*, 22(5):633–638, 2006.

[87] Keith T Chan, Christopher Doran, Erik G Shipton, and Eric E Fullerton. Core-shell structured nanowire spin valves. *Magnetics, IEEE Transactions on*, 46(6): 2209–2211, 2010.

[88] Antonino Salvatore Arico, Peter Bruce, Bruno Scrosati, Jean-Marie Tarascon, and Walter Van Schalkwijk. Nanostructured materials for advanced energy conversion and storage devices. *Nature materials*, 4(5):366–377, 2005.

[89] Weiyang Li, Chunsheng Li, Chunyuan Zhou, Hua Ma, and Jun Chen. Metallic magnesium nano/mesoscale structures: their shape-controlled preparation and mg/air battery applications. *Angewandte Chemie International Edition*, 45(36): 6009–6012, 2006.

[90] GJ Williams, MA Pfeifer, IA Vartanyants, and IK Robinson. Three-dimensional imaging of microstructure in au nanocrystals. *Physical review letters*, 90(17): 175501, 2003.

[91] Mark A Pfeifer, Garth J Williams, Ivan A Vartanyants, Ross Harder, and Ian K Robinson. Three-dimensional mapping of a deformation field inside a nanocrystal.

Nature, 442(7098):63–66, 2006.

[92] A Ulvestad, HM Cho, R Harder, JW Kim, SH Dietze, E Fohtung, YS Meng, and OG Shpyrko. Nanoscale strain mapping in battery nanostructures. *Applied Physics Letters*, 104(7):073108, 2014.

[93] Satio Takagi. A dynamical theory of diffraction for a distorted crystal. *Journal of the Physical Society of Japan*, 26(5):1239–1253, 1969.

[94] Geoffrey SD Beach, Corneliu Nistor, Carl Knutson, Maxim Tsoi, and James L Erskine. Dynamics of field-driven domain-wall propagation in ferromagnetic nanowires. *Nature materials*, 4(10):741–744, 2005.

[95] Sumio Iijima et al. Helical microtubules of graphitic carbon. *nature*, 354(6348): 56–58, 1991.

[96] V Uhlíř, Stefania Pizzini, Nicolas Rougemaille, J Novotnỳ, Vincent Cros, Erika Jiménez, Giancarlo Faini, Lutz Heyne, Fausto Sirotti, Carsten Tieg, et al. Current-induced motion and pinning of domain walls in spin-valve nanowires studied by xmcd-peem. *Physical Review B*, 81(22):224418, 2010.

[97] A Fabian, Ch Terrier, S Serrano Guisan, X Hoffer, M Dubey, L Gravier, J-Ph Ansermet, and J-E Wegrowe. Current-induced two-level fluctuations in pseudo-spin-valve (c o/c u/c o) nanostructures. *Physical review letters*, 91(25):257209, 2003.

[98] Luc Piraux, Krystel Renard, Raphael Guillemet, Stefan Mátéfi-Tempfli, Mária Mátéfi-Tempfli, Vlad Andrei Antohe, Stéphane Fusil, Karim Bouzehouane, and Vincent Cros. Template-grown nife/cu/nife nanowires for spin transfer devices. *Nano letters*, 7(9):2563–2567, 2007.

[99] Stuart SP Parkin, Masamitsu Hayashi, and Luc Thomas. Magnetic domain-wall racetrack memory. *Science*, 320(5873):190–194, 2008.

[100] RS Wagner and WC Ellis. Vapor-liquid-solid mechanism of single crystal growth. *Applied Physics Letters*, 4(5):89–90, 1964.

[101] Keiichi Haraguchi, Toshio Katsuyama, Kenji Hiruma, and Kensuke Ogawa. Gaas p-n junction formed in quantum wire crystals. *Applied Physics Letters*, 60(6): 745–747, 1992.

[102] EI Givargizov. Fundamental aspects of vls growth. *Journal of Crystal Growth*, 31:

20–30, 1975.

[103] James L Carter. Vls (vapor-liquid-solid): Newly discovered growth mechanism on the lunar surface? *Science*, 181(4102):841–842, 1973.

[104] Chun Liu, Zheng Hu, Qiang Wu, Xizhang Wang, Yi Chen, Hai Sang, Jianmin Zhu, Shaozhi Deng, and Ningsheng Xu. Vapor-solid growth and characterization of aluminum nitride nanocones. *Journal of the American Chemical Society*, 127(4): 1318–1322, 2005.

[105] Jun Zhang, Lide Zhang, Xinsheng Peng, and Xiangfeng Wang. Vapor–solid growth route to single-crystalline indium nitride nanowires. *Journal of Materials Chemistry*, 12(4):802–804, 2002.

[106] Yung-Jung Hsu and Shih-Yuan Lu. Vapor-solid growth of sn nanowires: growth mechanism and superconductivity. *The Journal of Physical Chemistry B*, 109(10): 4398–4403, 2005.

[107] RE Cech. The role of halide-cycle reactions in the growth of nickel whiskers. *Acta Metallurgica*, 9(5):459–463, 1961.

[108] Paul HE Meijer. Kamerlingh onnes and the discovery of superconductivity. *American Journal of Physics*, 62(12):1105–1108, 1994.

[109] Fritz London and Heinz London. The electromagnetic equations of the supraconductor. In *Proceedings of the Royal Society of London A: Mathematical, Physical and Engineering Sciences*, volume 149, pages 71–88. The Royal Society, 1935.

[110] John Bardeen, Leon N Cooper, and John Robert Schrieffer. Theory of superconductivity. *Physical Review*, 108(5):1175, 1957.

[111] Jian Wang, Chuntai Shi, Mingliang Tian, Qi Zhang, Nitesh Kumar, JK Jain, TE Mallouk, and MHW Chan. Proximity-induced superconductivity in nanowires: minigap state and differential magnetoresistance oscillations. *Physical review letters*, 102(24):247003, 2009.

[112] Yu N Chiang, OG Shevchenko, and RN Kolenov. Manifestation of coherent and spin-dependent effects in the conductance of ferromagnets adjoining a superconductor. *Low Temperature Physics*, 33(4):314–320, 2007.

[113] Jose Aumentado and Venkat Chandrasekhar. Mesoscopic ferromagnet-superconductor junctions and the proximity effect. *Physical Review B*, 64(5):

054505, 2001.

[114] FS Bergeret, AF Volkov, and KB Efetov. Odd triplet superconductivity and related phenomena in superconductor-ferromagnet structures. *Reviews of modern physics*, 77(4):1321, 2005.

[115] I Sosnin, H Cho, VT Petrashov, and AF Volkov. Superconducting phase coherent electron transport in proximity conical ferromagnets. *Physical review letters*, 96 (15):157002, 2006.

[116] V Peña, Zouhair Sefrioui, D Arias, C Leon, J Santamaria, M Varela, SJ Pennycook, and JL Martinez. Coupling of superconductors through a half-metallic ferromagnet: Evidence for a long-range proximity effect. *Physical review B*, 69(22):224502, 2004.

[117] VT Petrashov, IA Sosnin, I Cox, A Parsons, and C Troadec. Giant mutual proximity effects in ferromagnetic/superconducting nanostructures. *Physical review letters*, 83(16):3281, 1999.

[118] M Giroud, H Courtois, K Hasselbach, D Mailly, and B Pannetier. Superconducting proximity effect in a mesoscopic ferromagnetic wire. *Physical Review B*, 58(18): R11872, 1998.

[119] RS Keizer, STB Goennenwein, TM Klapwijk, G Miao, Gang Xiao, and A Gupta. A spin triplet supercurrent through the half-metallic ferromagnet cro2. *Nature*, 439(7078):825–827, 2006.

[120] Jian Wang, Meenakshi Singh, Mingliang Tian, Nitesh Kumar, Bangzhi Liu, Chuntai Shi, JK Jain, Nitin Samarth, TE Mallouk, and MHW Chan. Interplay between superconductivity and ferromagnetism in crystalline nanowires. *Nature Physics*, 6(5):389–394, 2010.

[121] JE Wegrowe, D Kelly, A Franck, SE Gilbert, and J-Ph Ansermet. Magnetoresistance of ferromagnetic nanowires. *Physical review letters*, 82(18):3681, 1999.

[122] Satoshi Kokado and Masakiyo Tsunoda. Anisotropic magnetoresistance effect: General expression of amr ratio and intuitive explanation for sign of amr ratio. In *Advanced Materials Research*, volume 750, pages 978–982. Trans Tech Publ, 2013.

[123] IA Campbell, A Fert, and O Jaoul. The spontaneous resistivity anisotropy in ni-based alloys. *Journal of Physics C: Solid State Physics*, 3(1S):S95, 1970.

[124] A Fert and Luc Piraux. Magnetic nanowires. *Journal of Magnetism and Magnetic Materials*, 200(1):338–358, 1999.

[125] B Raquet, M Viret, E Sondergard, O Cespedes, and R Mamy. Electron-magnon scattering and magnetic resistivity in 3 d ferromagnets. *Physical Review B*, 66(2): 024433, 2002.

[126] AI Gubin, KS Il'in, SA Vitusevich, M Siegel, and N Klein. Dependence of magnetic penetration depth on the thickness of superconducting nb thin films. *Physical Review B*, 72(6):064503, 2005.

[127] William Robert Grove. On the electro-chemical polarity of gases. *Philosophical Transactions of the Royal Society of London*, 142:87–101, 1852.

[128] T McGuire and RL Potter. Anisotropic magnetoresistance in ferromagnetic 3d alloys. *IEEE Transactions on Magnetics*, 11(4):1018–1038, 1975.

[129] Mario Norberto Baibich, Jean Marc Broto, Albert Fert, F Nguyen Van Dau, Frédéric Petroff, P Etienne, G Creuzet, A Friederich, and J Chazelas. Giant magnetoresistance of (001) fe/(001) cr magnetic superlattices. *Physical review letters*, 61(21):2472, 1988.

[130] Grünberg Binasch, Peter Grünberg, F Saurenbach, and W Zinn. Enhanced magnetoresistance in layered magnetic structures with antiferromagnetic interlayer exchange. *Physical review B*, 39(7):4828, 1989.

[131] Terunobu Miyazaki and N Tezuka. Giant magnetic tunneling effect in fe/al 2 o 3/fe junction. *Journal of Magnetism and Magnetic Materials*, 139(3):L231–L234, 1995.

[132] Jagadeesh Subbaiah Moodera, Lisa R Kinder, Terrilyn M Wong, and R Meservey. Large magnetoresistance at room temperature in ferromagnetic thin film tunnel junctions. *Physical review letters*, 74(16):3273, 1995.

[133] S Ikeda, K Miura, H Yamamoto, K Mizunuma, HD Gan, M Endo, Sl Kanai, J Hayakawa, F Matsukura, and H Ohno. A perpendicular-anisotropy cofeb–mgo magnetic tunnel junction. *Nature materials*, 9(9):721–724, 2010.

[134] John C Slonczewski. Current-driven excitation of magnetic multilayers. *Journal of Magnetism and Magnetic Materials*, 159(1):L1–L7, 1996.

[135] Jürgen Fassbender, Daphiné Ravelosona, and Y Samson. Tailoring magnetism by

light-ion irradiation. *Journal of Physics D: Applied Physics*, 37(16):R179, 2004.

[136] D Ravelosona, C Chappert, V Mathet, and H Bernas. Chemical order induced by ion irradiation in fept (001) films. *Applied Physics Letters*, 76:236, 2000.

[137] Chih-Huang Lai, Cheng-Han Yang, and CC Chiang. Ion-irradiation-induced direct ordering of l10 fept phase. *Applied physics letters*, 83:4550, 2003.

[138] M Abes, O Ersen, D Muller, M Acosta, C Ulhaq-Bouillet, A Dinia, and V Pierron-Bohnes. Effect of ion irradiation on the structural and magnetic properties of sputtered copt alloy. *Materials Science and Engineering: C*, 23(1):229–233, 2003.

[139] A Maziewski, P Mazalski, Z Kurant, MO Liedke, J McCord, J Fassbender, J Ferré, A Mougin, A Wawro, LT Baczewski, et al. Tailoring of magnetism in pt/co/pt ultrathin films by ion irradiation. *Physical Review B*, 85(5):054427, 2012.

[140] T Devolder. Light ion irradiation of co/pt systems: structural origin of the decrease in magnetic anisotropy. *Physical Review B*, 62(9):5794, 2000.

[141] Takashi Hasegawa, W Pei, T Wang, Y Fu, T Washiya, H Saito, and S Ishio. Mfm analysis of the magnetization process in l1 0–a1 fept patterned film fabricated by ion irradiation. *Acta Materialia*, 56(7):1564–1569, 2008.

[142] C Chappert, H Bernas, J Ferré, V Kottler, J-P Jamet, Y Chen, E Cambril, T Devolder, F Rousseaux, V Mathet, et al. Planar patterned magnetic media obtained by ion irradiation. *Science*, 280(5371):1919–1922, 1998.

[143] M Abes, J Venuat, D Muller, A Carvalho, G Schmerber, E Beaurepaire, A Dinia, and V Pierron-Bohnes. Magnetic patterning using ion irradiation for highly ordered copt alloys with perpendicular anisotropy. *Journal of applied physics*, 96 (12), 2004.

[144] Eric Edward Fullerton and Dieter Klaus Weller. Magnetic recording media with magnetic bit regions patterned by ion irradiation, May 7 2002. US Patent 6,383,597.

[145] L Herrera Diez, F García-Sánchez, J-P Adam, T Devolder, S Eimer, MS El Hadri, A Lamperti, R Mantovan, B Ocker, and D Ravelosona. Controlling magnetic domain wall motion in the creep regime in he+-irradiated cofeb/mgo films with perpendicular anisotropy. *Applied Physics Letters*, 107(3):032401, 2015.

[146] T Devolder, I Barisic, S Eimer, K Garcia, J-P Adam, B Ockert, and D Rav-

elosona. Irradiation-induced tailoring of the magnetism of cofeb/mgo ultrathin films. *Journal of Applied Physics*, 113(20):203912, 2013.

[147] Woojin Kim, JH Jeong, Y Kim, WC Lim, JH Kim, JH Park, HJ Shin, YS Park, KS Kim, SH Park, et al. Extended scalability of perpendicular stt-mram towards sub-20nm mtj node. In *Electron Devices Meeting (IEDM), 2011 IEEE International*, pages 24–1. IEEE, 2011.

[148] AV Khvalkovskiy, D Apalkov, S Watts, R Chepulskii, RS Beach, A Ong, X Tang, A Driskill-Smith, WH Butler, PB Visscher, et al. Basic principles of stt-mram cell operation in memory arrays. *Journal of Physics D: Applied Physics*, 46(7): 074001, 2013.

[149] WG Wang, C Ni, A Rumaiz, Y Wang, X Fan, T Moriyama, R Cao, QY Wen, HW Zhang, and John Q Xiao. Real-time evolution of tunneling magnetoresistance during annealing in cofeb/mgo/cofeb magnetic tunnel junctions. *Applied Physics Letters*, 92(15):152501, 2008.